THE FINITE-DIFFERENCE TIME-DOMAIN METHOD AND ITS APPLICATION TO THE ANALYSIS OF MICROSTRIP ANTENNAS

By

ZHIQIANG BI, B.Sc.(Eng.), and M.Eng.
(Dalian Maritime University)

A Thesis
Submitted to the School of Graduate Studies
in Partial Fulfilment of the Requirements
for the Degree
Doctor of Philosophy

McMaster University
April 1994

DOCTOR OF PHILOSOPHY (1994)
(Electrical and Computer Engineering)

MCMASTER UNIVERSITY
Hamilton, Ontario, Canada

TITLE: **The finite-difference time-domain method and its application to the analysis of microstrip antennas**

AUTHOR: Zhiqiang Bi
B.Sc.(Eng.), and M.Eng.
(Dalian Maritime University)

SUPERVISOR: Dr. John Litva
Professor, Electrical Engineering

NUMBER OF PAGES: xv, 156

ISBN 0-315-93397-6

Canada

THE FINITE-DIFFERENCE TIME DOMAIN METHOD AND ITS APPLICATION TO THE ANALYSIS OF MICROSTRIP ANTENNAS

Abstract

In this thesis, issues related to the FD-TD method and its application are discussed. In particular, absorbing boundary conditions, use of signal processing techniques with the FD-TD method, and the application of the FD-TD technique to analyzing microstrip antennas are studied.

A new theory called *dispersive boundary condition* (DBC) theory is formulated and developed. The concept of dispersive boundary condition is introduced first. Based on this concept, three dispersive absorbing boundary conditions are proposed from differing points of view. These DBC's are applied to microstrip and waveguide component analyses. Using these dispersive boundary conditions, great savings in computer memory and significant improvements in the accuracy of the FD-TD method can be achieved for dispersive structure analyses.

The use of digital signal processing (DSP) techniques for improving the performance of the FD-TD method is introduced. We demonstrate that the capabilities and the efficiency of the FD-TD method can be improved in several aspects due to the introduction of DSP. In the dispersive absorbing boundary condition studies, digital filter theory is applied to analyze and design DBC. Several DBC's have been unified by using digital filter theory, and it is expected that this will stimulate further development in absorbing boundary conditions.

Also, modern spectrum estimation and digital filtering techniques are used to improve the efficiency of FD-TD method in solving eigenvalue problems. It is demonstrated by means of numerical and experimental results that the efficiency of the FD-TD method for dielectric resonator analysis improves by about one order of magnitude. This new result makes it possible for the FD-TD method to be used as a practical tool for analyzing dielectric resonators.

The FD-TD method is used to accurately characterize complex planar printed antennas with various feed structures, including microstrip line feed, proximity coupled feed, aperture coupled feed, and coaxial probe feed structures. The validity of a coaxial probe

feed model is demonstrated by a comparison of simulated and experimental results. For high dielectric constant substrate antennas, the dispersive boundary condition is employed to absorb strongly dispersive waves. In addition, several other new treatments have been tested for microstrip antenna analysis. All the numerical results obtained using the FD-TD method are compared with experimental results, and the comparison shows excellent agreement over a wide frequency band.

Acknowledgments

This dissertation ends an important chapter of my life, one whose conclusion would have been impossible without help from many others. The list is long, but in particular, I would like to mention a few.

I am deeply grateful to my thesis and academic advisor, Professor John Litva, for his research supervision, encouragement, expertise in electromagnetics and signal processing techniques, and support of a world class research facility. Without any of these, my research would not have been possible. I am also very grateful to him for the memorable times I have had. Working together with Dr. Litva is always a kind of enjoyment.

I am deeply indebted to Dr. Keli Wu for his many stimulating comments throughout this research, his friendship, and his guidance in the earlier stages when I changed the research field from signal processing into electromagnetics. I am also deeply indebted to Mr. Chen Wu for his many discussions and friendship. A large part of the present research was a result of our cooperative effort and much of the work on modelling of coaxial-fed microstrip patch antenna is Chen and Keli's contribution.

I am very thankful to two of my best friends, Richard Yang and Dr. Xuemin Shen for their continuous friendship and encouragement. Richard, my officemate, has given me the tremendous help in many aspects in the last three years. Xuemin, my former college classmate, who has published twenty five journal papers and has written two books, has given me valuable advice on both work and life by telling his failing and success experience. Thank you both and good luck in your future endeavors.

I owe special thanks to members of Professor Litva's research group who made it possible for me to complete this dissertation. Russ Fralich, who was the group meeting organizer, created a good environment where I had a chance to present my updated research and get suggestions from the other members. My thanks to Yuan Zhang for his discussions on fundamental electromagnetics, Ying Shen for his discussions on dielectric resonator, Titus Lo for his discussions on signal processing techniques, Andrew Liang, Minya Zhang,

Ban Quach, Nagula Sangary, Charies Laperle. Garth Jenkins, Liliana Lavi and Albert Chan for their friendship.

I also owe special thanks to the other members of Communications Research Laboratory, including Qu Jin and Jingyun Li for their years of friendship, Zhijian Hu for his many comments on the subjects related to electrical engineering, Andrew Ukrainec for his help with computers, Barry Zhou for his helping in preparing my comprehensive examination, and Xiaohui Wu for the discussions on electromagnetics. Further thanks to Qiang Wu, Weiguo Chen and A. Drosopoulos for their discussions on digital signal processing techniques, Liang Li and Bob Li for their discussions on neural networks, Nasir Ghani for his proofreading parts of the thesis, and computer managers, Terry Greenlay and Dean McArthur.

I acknowledge Canadian Government, the Ontario Provincial Government and the McMaster University for their financial support through the Canadian International Development Agency Scholarship (CIDA), Ontario Graduate Scholarship (OGS), and Teaching & Research Scholarship, respectively. The support provided by the Telecommunications Research Institute of Ontario is also deeply acknowledged.

I would like to express my deep thanks to all of my family members for their love, understanding, support and believing in me in the past.

Last, but most important, I thank my wife, Weiming, for her unfailing love, companionship and for her support and sacrifice during this often difficult effort.

Contents

List of Tables

List of Figures

Chapter 1

INTRODUCTION

In the last few years, the *Finite-Difference Time-Domain* (FD-TD) method for solving Maxwell's equations has received a great of attention in the field of *Computational Electromagnetics* (CEM). This is primarily due to several desirable attributes. First, the FD-TD method can be applied to problems exhibiting a complex structure which may be very difficult to solve using other analytical or numerical methods. Second, the FD-TD is a time domain method by which transient phenomena can be studied. Third, the Fourier transform of the transient result of FD-TD yields frequency domain results over a large spectrum. This is very elegant, since only one computation is required. Traditional frequency domain methods require many computations (one frequency point at a time). Fourth, it can be applied to inhomogeneous, lossy, anisotropic, time varying and dispersive media. Most other approaches are not that flexible. The main disadvantages of the method are its requirements for, (a) large computer memory, and (b) long computational times when analyzing both three-dimensional and large scale two-dimensional problems. Overcoming these limitations depends on two aspects: the development of fast computers and improvement of the method itself. The purpose of this thesis is to contribute to the development of the method and to employ the improved method to study some microstrip antennas which might be very difficult to analyze using alternate techniques.

1.1 Literature Survey

Since Kane Yee [1] introduced the finite-difference time-domain method for solving Maxwell's equations in 1966, the method has been widely used for solving many electromagnetic problems. In recent years, most of the research have been directed at achieving more accurate discretization schemes [2]-[12], better absorbing boundary conditions [17]-[33], more efficient implementations on supercomputers [44], and applications to various electromagnetic problems. Examples of these problems are scattering problems [45]-[48], microstrip circuits and antennas [49]-[57], waveguides [65]-[70], and problems related to medical applications. The discretization scheme is crucial to modeling the physical geometry of the structures, treating dielectric/magnetic materials, implementation, and accuracy. Absorbing boundary conditions are crucial to reducing the size of the computational domain, the number of discretization nodes, and hence, computer memory and the computation time requirements.

1.1.1 Finite Difference Schemes

The rectangular grid is perhaps the most widely used form of discretization in computational electromagnetics. In the rectangular grid, arbitrary geometries are approximated by using staircases. In Yee's algorithm [1], the electric and magnetic fields are spatially interlaced. Within a rectangular cell, electric fields are placed along the edges, and magnetic fields are placed at the face centers. Furthermore, these electric and magnetic fields are also temporally interlaced. The spatial and temporal derivatives of the field components are approximated in a central difference manner which provides accuracy to the second order. For the rectangular grid, keeping track of geometry is trivial and only requires integer arithmetic. Consequently, the implementation of FD-TD proceeds in a straightforward manner with a minimum requirement for the storage of data. Yee [1] applied FD-TD to initial boundary value problems in isotropic media. Taflove [46] employed the method

to obtain frequency domain solutions to scattering problems. By exciting with incident sinusoidal electric fields and waiting for the steady state, frequency domain solutions were extracted from the time domain results; the stability criteria of the second order Yee's scheme was also derived in Taflove's investigations. Holland [47, 48] employed the FD-TD to analyze electromagnetic pulse problems. These techniques have since been thoroughly investigated and a considerable amount of effort has been expended in the computer code development.

Although the rectangular grid provides the simplest discretization scheme, the accuracy of the staircasing approximation is questionable when the space step is larger than $\lambda/20$. To improve upon the staircasing approximation, a number of FD-TD conformal surface models have been proposed. These fall into three principal groups.

The models in the first group use globally-stretched grids. These employ available numerical mesh generation schemes to construct non-Cartesian grids which are continuously and globally stretched to conform with structure surfaces. Examples of this approach include the FD-TD algorithm in curvilinear coordinates [4, 5, 6], tangential flux conservation schemes [7], and the recently developed triangular grid FD-TD algorithm [2].

The models in the second group use locally-stretched grid models. These preserve the basic Cartesian grid arrangement of field components at all space cells except those adjacent to the structure's surface. Space cells adjacent to the surface are deformed to conform with the surface locus. Only field components in these cells are provided with a modified time-stepping algorithm. Examples of this approach include the contour FD-TD scheme [3, 45], which is derived by numerically approximating Ampere's and Faraday's integral equations, the mixed-polygonal modified finite volume method [9, 13], and the finite element derived time domain methods [9, 10].

The models in the third group include variable mesh algorithms [49, 2] and the

multigrid algorithm [13]. Both of these algorithms use fine grids around discontinuities with the grids evolving into coarse meshes near the wall of the computational domain. The main difference between the two algorithms is that the variable mesh uses only one time step, determined by the finest grid in the entire volume, while the multigrid algorithm uses several time increments corresponding to different spatial increments.

Research is ongoing for each of these types of conformal surface models and for developing new finite difference schemes. Key issues include: ease of mesh generation; suppression of numerical artifacts such as instability, dispersion, pseudo-refraction, and subtraction noise limitation of computational dynamic range; coding complexity; and computer execution time [74].

In Chapter 2, an alternative finite difference scheme for solving the Maxwell's equation in the time domain will be presented.

1.1.2 Absorbing Boundary Conditions

In a finite-difference scheme, the grid that contains the points for finite differencing has to be of finite extent due to the limits on computer memory and resources. In most cases the finite-difference grid lies in a box. But in many applications, the media are of infinite extent. To simulate an infinite geometry, *absorbing boundary conditions* (ABC) are needed at the surface of the box. The use of absorbing boundary conditions reduces computer memory requirements since the size of the box can be made smaller.

There are several approaches to deriving absorbing boundary conditions. One popular approach involves factoring the wave operator into a product of incoming and outcoming wave operators with respect to the computational domain. The operator or the wave equation that governs the outgoing wave field is then used to design the absorbing boundary

condition. Because this approach is based on an approximation to the one-way wave equation, the derived absorbing boundary conditions are called one-way absorbing boundary conditions.

This strategy was used by Lindman in 1975 [23], Clayton and Engquits in 1977 [19], Engquist and Majda in 1977 [20] and in 1979 [21], Mur in 1981 [22], and Lee in 1990 [2]. Several one-way absorbing boundary conditions under different coordinate systems have been presented. These ABCs have been further developed and their performances have been thoroughly tested by Halpern and Trefethen [24, 25], Blaschak [26], Moore [27] and Fang [17].

The other two ABCs which are becoming more and more popular are Key and Higdon ABC [30]-[32], and Liao's ABC [33]. These two ABCs together with the Bayliss-Turkell ABC [28] which was developed under the spherical coordinates can be referred to as *one-dimensional ABCs*. The reason for using this name will be explained later in Chapter 3. This new classification will provide some physical insights into these ABCs.

Recently, the FD-TD has been used to calculate complex microstrip circuits and antennas [49]-[54],[56, 57], waveguide components [65]-[68], and guided-wave optical structures [69, 70]. All of these calculations have shown the FD-TD to be a very powerful tool for the above analyses. However, this method has one serious limitation when it is applied to the analysis of these structures. It is found that the accuracy of the FD-TD method may vary as a function of frequency, that is, it may not have the required accuracy over a wide frequency range. The reason for this is tied to the fact that when a pulse travels on a particular structure, the velocities of the fields are different for different frequencies due to the dispersive nature of the structure. When applying the ordinary angle absorbing boundary conditions to the boundary of the calculation domain, it is found that it falls short of the mark because it is an optimal absorber of waves at only one frequency or for one

velocity. For the analysis of these structures, a new kind of absorbing boundary conditions needs to be proposed, one which can absorb waves over a wide frequency band. We call this kind of boundary conditions as a *Dispersive Boundary Condition* (DBC). In Chapter 3, several DBCs will be presented and studied, and dispersive boundary condition theory will be systematically formulated and developed.

1.1.3 The Applications of the FD-TD Method

The wide applications of the FD-TD method were thoroughly reviewed by Taflove in [46] and Jurgens in [3]. We will review several of the latest developments on the applications of the FD-TD technique.

In the last few years, a number of investigators have used the FD-TD method to calculate the frequency-dependent characteristics of microstrip discontinuities [51, 52], microstrip circuits [49, 50], simple microstrip antennas [49, 50, 54], and complex microstrip antennas [72, 73]. All of these calculations have shown the FD-TD method to be a very powerful tool for these analyses because of its several highly desired atributes. However, in the case of the coaxial-line feed microstrip antenna problem the analysis is based on assumptions that deviate from reality. For example, the discontinuity between the coaxial line and patch region is replaced by an equivalent lump resistance, and, as well, the characteristic impedance of the coaxial line is not included in the model [54]. Obviously, it is very difficult to obtain an accurate equivalent resistance to incorporate all of the effects of the discontinuity near the connector, especially if the modeling is being carried out over a wide frequency range. On the other hand, although a number of researchers have given attention to modeling line-fed printed antennas using the FD-TD method, as of yet, none has addressed the problem of strong dispersion when the dielectric constant is high. For

microstrip circuit analysis, absorbing the strongly dispersive wave on high dielectric microstrip line also has not been studied so far. These two issues will be addressed in the thesis.

Recently, work has been reported on FD-TD modeling of semiconductor devices. Sano and Shibata [55] combine the conventional FD-TD form of Maxwell's equations with current continuity equations based on drift diffusion for both electrons and holes to obtain a self-consistent solution for charge and fields in picosecond photoconductive switches. The modeling of the generation and recombination of electrons and holes appears as current density in Maxwell's curl equations. Results are qualitatively compared with experimental data. Another approach also has been reported on the FD-TD modeling of active circuits [56]. In this approach, based on the relationships between the E and H fields and the voltages and currents, the conventional FD-TD method is generalized so as to allow inclusion of lumped elements within the grid. By specifying the appropriate I-V characteristics of the sources and elements, both passive and active, as well as linear and nonlinear circuit elements, can be treated. The validity of these two methods needs to be further verified in the future.

The FD-TD method has been used to calculate the properties of waveguide components [65]-[68],[71] in the last few years. It has been shown that the FD-TD method can be easily adapted to complex geometries. Howerer, most of the papers are limited to using monochromatic waves as the excitation for waveguide component analysis due to the lack of a good dispersive absorbing boundary condition. This strikes a blow at one of the most important advantages of time domain methods. That is, by using a pulse as excitation, only one computation is required to get the frequency domain results over a large frequency spectrum. The presented dispersive boundary conditions will be used to attack this problem.

It has been demonstrated that dielectric resonators can be analyzed very accurately using FD-TD [91, 92]. The resonant frequencies for different modes can be obtained with one computation. However, this method has one significant drawback, which is that it requires a very long computation time before the resonant frequencies can be extracted from the FD-TD results. This limitation can be overcome by incorporating digital filtering and modern spectrum estimation techniques into the FD-TD method.

Recently, the FD-TD method has been generalized to treat frequency dispersive materials. For general dispersive materials, two approaches have been developed. In the first approach, convolution integrals are employed [36, 37]. Since these convolutions are applied to every discretization point at every time step, this approach is very time consuming and requires large memory. The second approach [2, 38] does not require time domain convolution. The time domain models of the dispersive materials are written in the form of ordinary time differential equations. This second algorithm is much more efficient than the first in terms of computation time and memory requirement. It can be shown that these two models can be unified if one applies systems analysis concept.

1.2 Description of the Thesis

In this thesis, issues related to the FD-TD method and its applications are discussed. In particular, a finite difference time domain algorithm, absorbing boundary conditions, use of signal processing techniques with the FD-TD method, and applications of the FD-TD technique for analyzing microstrip antennas are studied.

In Chapter 2, an alternative finite difference scheme for solving the Maxwell's equation in the time domain is presented. The new scheme provides greater flexibility for studying the finite-element time-domain (FE-TD) method, multigrid method, variable mesh method, and the method of finite difference approximations to boundary conditions.

In Chapter 3, the concept of dispersive boundary condition is introduced. Based on this concept, three dispersive boundary conditions are proposed and studied from different points of view. Based on these studies, a theory of dispersive absorbing boundary conditions is systematically formulated and developed. These dispersive boundary conditions allow us to achieve great savings in computer memory requirements when analyzing microstrip and waveguide components.

In Chapter 4, digital filtering and spectrum estimation techniques are used with the FD-TD method to improve its efficiency for solving eigenvalue problems. The considerable improvement in the efficiency for the method is demonstrated by means of both numerical and measured results. In addition, several improvements to the present FD-TD method for eigenvalue analysis are presented. These include the analysis of open dielectric resonators, the extraction of resonant frequencies and the calculation of the field distribution from the FD-TD results. The result for the open dielectric resonator analysis is validated using the measured data.

In Chapter 5, the FD-TD method is used to accurately characterize complex planar printed antennas with various feed structures, which include, microstrip line feed, proximity coupled feed, aperture coupled feed and coaxial probe feed structures. A coaxial probe model is developed by using a three-dimensional FD-TD technique. This model is shown to be an efficient and accurate tool for modeling coaxial-line fed structures. On the other hand, although a number of researchers have given attention to modelling line-fed printed antennas using the FD-TD method, as of yet, none has addressed the problem of strong dispersion when the dielectric constant is high. The situation will be addressed in this chapter by means of the dispersive absorbing boundary condition presented in Chapter 3.

Chapter 6 summarizes the study on the FD-TD method and its applications to microstrip component and waveguide component analyses.

Chapter 2

A NEW FD-TD SCHEME FOR SOLVING MAXWELL'S EQUATIONS

2.1 Introduction

To date, Yee's FD-TD method has received a great deal of attention because it has a number of desirable attributes. Recently, several other time domain methods have been presented. These have been developed to overcome the rectangular lattice limitations of the method. Listed among of these are the finite element derived time domain methods [8, 9], the point-matched time domain finite element method [10, 11], and the FD-TD method which uses triangular grids [2]. All of these methods make use of the conforming ability of the finite element method to approximate physical boundaries more accurately.

The objective of this chapter is to investigate other forms of finite difference schemes, and to improve the stability condition of Yee's FD-TD method. In what follows, we first present a new FD-TD scheme. Then, we show that this scheme is of second order accuracy, and that it has a larger stability condition than Yee's scheme. Finally, we discuss the

relationship between the scheme presented here and the *finite element derived time domain methods* (FE-TD).

2.2 Description of the New Scheme

Maxwell's equations in a source free isotropic medium are

$$\frac{\partial \vec{H}}{\partial t} = -\frac{1}{\mu} \nabla \times \vec{E} \tag{2.1}$$

$$\frac{\partial \vec{E}}{\partial t} = \frac{1}{\epsilon} \nabla \times \vec{H}. \tag{2.2}$$

For ease of understanding, we introduce the algorithm by describing the two dimensional case, and assume TM mode propagation. Under these conditions, Maxwell's equations become

$$\frac{\partial H_x}{\partial t} = -\frac{1}{\mu}\frac{\partial E_z}{\partial y} \tag{2.3}$$

$$\frac{\partial H_y}{\partial t} = \frac{1}{\mu}\frac{\partial E_z}{\partial x} \tag{2.4}$$

$$\frac{\partial E_z}{\partial t} = \frac{1}{\epsilon}\left(\frac{\partial H_y}{\partial x} - \frac{\partial H_x}{\partial y}\right). \tag{2.5}$$

Yee's method uses the central finite-difference approximation of both the space and the time derivatives to discretize the Maxwell's equations. The scheme presented here, which is analogous to the Rotated Richtmyer Scheme [14]-[16], discretizes Maxwell's equations into the following finite difference equations:

$$\begin{aligned} H_x^{n+\frac{1}{2}}(i,j) = {} & H_x^{n-\frac{1}{2}}(i,j) - \frac{\Delta t}{\mu \Delta y} \cdot \left\{ \frac{1}{2}[E_z^n(i,j) + E_z^n(i,j-1)] \right. \\ & \left. -\frac{1}{2}[E_z^n(i-1,j) + E_z^n(i-1,j-1)] \right\} \end{aligned} \tag{2.6}$$

$$\begin{aligned} H_y^{n+\frac{1}{2}}(i,j) = {} & H_y^{n-\frac{1}{2}}(i,j) + \frac{\Delta t}{\mu \Delta x} \cdot \left\{ \frac{1}{2}[E_z^n(i,j) + E_z^n(i-1,j)] \right. \\ & \left. -\frac{1}{2}[E_z^n(i,j-1) + E_z^n(i-1,j-1)] \right\} \end{aligned} \tag{2.7}$$

$$
\begin{aligned}
E_z^{n+1}(i,j) &= E_z^n(i,j) + \frac{\Delta t}{\epsilon \Delta x} \cdot \left\{ \frac{1}{2}[H_y^{n+\frac{1}{2}}(i+1,j+1) + H_y^{n+\frac{1}{2}}(i,j+1)] \right. \\
&\quad \left. - \frac{1}{2}[H_y^{n+\frac{1}{2}}(i+1,j) + H_y^{n+\frac{1}{2}}(i,j)] \right\} \\
&\quad - \frac{\Delta t}{\epsilon \Delta y} \cdot \left\{ \frac{1}{2}[H_x^{n+\frac{1}{2}}(i+1,j+1) + H_x^{n+\frac{1}{2}}(i+1,j)] \right. \\
&\quad \left. - \frac{1}{2}[H_x^{n+\frac{1}{2}}(i,j+1) + H_x^{n+\frac{1}{2}}(i,j)] \right\}. \qquad (2.8)
\end{aligned}
$$

The lattice used for implementing the proposed scheme is shown in region A of Fig. 2.1. It differs from the conventional lattice used for Yee's method, which is shown in region B of Fig. 2.1. The new lattice is referred to as rotated lattice since this lattice rotates $\pi/4$ relative to Yee's. The proposed algorithm can be interpreted as an average finite difference scheme. From (2.6)-(2.8), it can be seen that this scheme consists of two steps. The first step consists of finding average values for the components of the fields on fictitious nodes such as those at p, p' and q, q'. During the second step one uses the values obtained in the first step to derive the centered difference approximation to Maxwell's equations.

It can be shown that the proposed scheme is very compatible with the conventional Yee's method. In region A of Fig. 2.1, the new scheme is used, and in region B, Yee's method is used. At the interface between the two regions, we use both algorithms to calculate the values which correspond to the different schemes. In this way we can easily transfer from one region to the other. The transition is guaranteed to have the same accuracy as either of the two methods, i.e., the second order accuracy.

2.3 Stability and Convergence of the Scheme

In this section, we discuss the conditions under which the approximate solutions derived from the numerical scheme converge to the exact value. In any finite difference scheme, a system of differential equations is replaced by a discretized one. The discretized system has

of course an exact theoretical solution. Let $\bar{u}$ represent the exact solution of the discretized system and $\bar{U}$ the exact solution of the differential system. Then, if $\bar{x}$ and t are the independent variables, the discretized system is said to be convergent to the differential one when the difference between $\bar{u}$ and $\bar{U}$, at a fixed point $(\bar{x}, t)$, tends to zero uniformly, as the computational net is refined in such a way that $\Delta x, \Delta t \to 0$ and $m_i, n \to \infty$, $(i = 1, 2, 3)$, with $m_i \Delta t (= x_i)$ and $n\Delta t (= t)$ remaining fixed. In general, it is difficult to investigate the problem of convergence. Fortunately, the convergence of discrete approximations to linear hyperbolic differential equations can be studied by using the Lax equivalence theorem in terms of stability and consistency. The theorem reads: If a finite difference approximation is consistent with a properly posed linear initial-value problem, then stability is the necessary and sufficient condition for convergence. Therefore, once the consistency of the scheme is demonstrated, we only need to examine the condition under which the scheme is stable, in order to ensure convergence.

It can be shown that the new scheme is consistent. To start with, consider the hyperbolic system of Maxwell's curl equations (2.1) and (2.2) for $t \geq 0$ with initial conditions:

$$\vec{E}(\vec{r}, 0) = \vec{G}_1(\vec{r}) \quad \text{and} \quad \vec{H}(\vec{r}, 0) = \vec{G}_2(\vec{r}). \tag{2.9}$$

On a domain without boundaries, the above system consists of a properly posed initial-value problem called the Cauchy problem. Consistency provides assurance that, as the finite difference mesh is refined (i.e., as space and time steps tend to zero), the truncation errors go to zero. Alternatively, one can say that the finite difference model approximates the desired PDE and not some other PDE. For simplicity, a normalized form of one of Maxwell's curl equations is examined. The model equation is

$$\frac{\partial U}{\partial t} = \frac{\partial V_y}{\partial x} - \frac{\partial V_x}{\partial y}. \tag{2.10}$$

As the Yee's method, the following central difference approximation is used for the

time derivative

$$\left\{\frac{\partial U}{\partial t}\right\}_n \approx \frac{U^{n+\frac{1}{2}} - U^{n-\frac{1}{2}}}{\Delta t}. \tag{2.11}$$

Using Taylor's expansion

$$U^{n+\frac{1}{2}} = U^n + \frac{\Delta t}{2}\left\{\frac{\partial U}{\partial t}\right\}_n + \frac{1}{2!}\left(\frac{\Delta t}{2}\right)^2\left\{\frac{\partial^2 U}{\partial t^2}\right\}_n + ... \tag{2.12}$$

$$U^{n-\frac{1}{2}} = U^n - \frac{\Delta t}{2}\left\{\frac{\partial U}{\partial t}\right\}_n + \frac{1}{2!}\left(\frac{\Delta t}{2}\right)^2\left\{\frac{\partial^2 U}{\partial t^2}\right\}_n - .... \tag{2.13}$$

and by substitution, we have

$$\frac{U^{n+\frac{1}{2}} - U^{n-\frac{1}{2}}}{\Delta t} = \left\{\frac{\partial U}{\partial t}\right\}_n + \frac{1}{24}(\Delta t)^2\left\{\frac{\partial^3 U}{\partial t^3}\right\}_n + ... \tag{2.14}$$

In the case of the space derivatives, the new algorithm provides the following approximations (refer to Fig. 2.2):

$$\left\{\frac{\partial V_y}{\partial x}\right\}_{(A)} \approx \frac{1}{\Delta x}\{\frac{1}{2}[V_y(3) + V_y(2)] - \frac{1}{2}[V_y(4) + V_y(1)]\} \tag{2.15}$$

$$\left\{\frac{\partial V_x}{\partial y}\right\}_{(A)} \approx \frac{1}{\Delta y}\{\frac{1}{2}[V_x(4) + V_x(3)] - \frac{1}{2}[V_x(2) + V_x(1)]\} \tag{2.16}$$

Again, by Taylor's expansion

$$\begin{aligned} V_y(1) &= V_y(A) - \frac{\Delta x}{2}\left\{\frac{\partial V_y}{\partial x}\right\}_{(A)} - \frac{\Delta y}{2}\left\{\frac{\partial V_y}{\partial y}\right\}_{(A)} \\ &+ \frac{1}{2!}\left(\frac{\Delta x}{2}\right)^2\left\{\frac{\partial^2 V_y}{\partial x^2}\right\}_{(A)} + \frac{1}{2!}\left(\frac{\Delta y}{2}\right)^2\left\{\frac{\partial^2 V_y}{\partial y^2}\right\}_{(A)} \\ &+ \frac{1}{2!}\left(\frac{\Delta x}{2}\right)\left(\frac{\Delta y}{2}\right)\left\{\frac{\partial^2 V_y}{\partial x \partial y}\right\}_{(A)} + ... \end{aligned} \tag{2.17}$$

$$\begin{aligned} V_y(2) &= V_y(A) + \frac{\Delta x}{2}\left\{\frac{\partial V_y}{\partial x}\right\}_{(A)} - \frac{\Delta y}{2}\left\{\frac{\partial V_y}{\partial y}\right\}_{(A)} \\ &+ \frac{1}{2!}\left(\frac{\Delta x}{2}\right)^2\left\{\frac{\partial^2 V_y}{\partial x^2}\right\}_{(A)} + \frac{1}{2!}\left(\frac{\Delta y}{2}\right)^2\left\{\frac{\partial^2 V_y}{\partial y^2}\right\}_{(A)} \\ &- \frac{1}{2!}\left(\frac{\Delta x}{2}\right)\left(\frac{\Delta y}{2}\right)\left\{\frac{\partial^2 V_y}{\partial x \partial y}\right\}_{(A)} + ... \end{aligned} \tag{2.18}$$

and similarly for $V_y(3), V_y(4), V_x(1), V_x(2), V_x(3), V_x(4)$. Then from equations (2.17) and (2.18) and similar ones for the rest of node values, with the supposition that $\Delta x = \Delta y = 2h$,

and after carrying out the necessary subtractions, we have

$$\frac{1}{\Delta x}\{\frac{1}{2}[V_y(3)+V_y(2)]-\frac{1}{2}[V_y(4)+V_y(1)]\} = \left\{\frac{\partial V_y}{\partial x}\right\}_{(A)}+O(h^2) \quad (2.19)$$

$$\frac{1}{\Delta y}\{\frac{1}{2}[V_y(3)+V_y(2)]-\frac{1}{2}[V_y(4)+V_y(1)]\} = \left\{\frac{\partial V_y}{\partial x}\right\}_{(A)}+O(h^2). \quad (2.20)$$

Finally, from equations (2.14),(2.19) and (2.20), we can have

$$\begin{aligned}\frac{U_A^{n+\frac{1}{2}}-U_A^{n-\frac{1}{2}}}{\Delta t} &- \frac{1}{\Delta x}\{\frac{1}{2}[V_y(3)+V_y(2)]-\frac{1}{2}[V_y(4)+V_y(1)]\}\\ &+ \frac{1}{\Delta y}\{\frac{1}{2}[V_x(4)+V_x(3)]-\frac{1}{2}[V_x(2)+V_x(1)]\}\\ &= \left(\frac{\partial U}{\partial t}-\frac{\partial V_y}{\partial x}+\frac{\partial V_x}{\partial y}\right)_{(A,n\Delta t)}\\ &+ O(\Delta t^2)+O(h^2)+....\end{aligned} \quad (2.21)$$

From the above equation (2.21), we can see that when we use the new scheme to approximate the differential equation, the principal part of the local truncation error due to the displacement is $O(\Delta t^2)+O(h^2)$. This error approaches zero with the second order of the mesh lengths Δt and h. Hence, the new scheme is consistent with the differential equation, and the new algorithm is of the second order accuracy.

Under the assumption of no additional numerical boundary conditions, there are several ways of analyzing the stability of a finite difference scheme. Using a method similar to that used by Wilson [14], it can be proven that the rotated scheme is stable if

$$\frac{c(\Delta t)}{\Delta x} \leq 1 \quad (2.22)$$

where c is the velocity of propagation, and $\Delta x = \Delta y$. This stability criterion is independent of the number of dimensions if the computational grid is uniform. This invariance with the dimensions of the problems is considered to be an advantage of our scheme when compared to Yee's scheme. Yee's stability condition depends on the number of dimensions n as

$$\frac{c\Delta t}{\Delta x} \leq \frac{1}{\sqrt{n}}. \quad (2.23)$$

Actually the condition (2.22) reaches the upper limit of Courant. Friedrichs and Lewy condition. On this basis, and also by examining the number of arithmetic operations in the four schemes [14, 16], Wilson concludes that the rotated scheme is the best algorithm.

We have carried out a numerical experiment to test the stability condition given by (2.22), as well as to check the validity of the new algorithm. An H-plane rectangular waveguide is chosen as the example [71] for our computation, where the excitation that is used on the excitation plane consists of a monochromatic dominant TE_{10} mode wave of unit amplitude. Both Yee's scheme and the new scheme have been applied to this problem. The stability factor, $\rho = c(\Delta t)/\Delta x$, is assumed to be 0.70 and 0.990, respectively, for the former and latter algorithms. A comparison of the results obtained using these two techniques is given in Fig. 2.3. The quantity that is being compared is the E_z field at a reference point. It is readily seen that by iteration 800 the new technique provides results covering a greater amount of time than the Yee's scheme. It is in this sense that the new method is considered to be more efficient than Yee's method. Another computation was carried out to test the stability conditions for Yee's scheme and the new scheme, respectively. The results show that once the stability factor exceeds 0.707186, Yee's method begins to diverge. But, in the case of the new scheme, the algorithm does not start to diverge until the value of stability factor exceeds 1. In Fig. 2.4 is given the compatibility testing result of the new scheme and Yee's method. In this test, the waveguide, as was the case in Fig. 2.1, consists of two regions, A and B. In region A, we use the new scheme, and in Region B, we use the Yee's scheme. The field is sampled in Region B. From this figure, we can see that the two schemes are very compatible.

2.4 The Relationship between the FE-TD and the FD-TD

It is shown in the appendix that the finite-element derived time-domain method [10, 11], defined over a rectangular subspace and formulated using isoparametric functions, is equivalent to the new finite-difference time domain method. This equivalence leads to simple interpretation for the FE-TD method and allows for straight-forward error analysis.

2.5 Summary

A new scheme of finite-difference time-domain computations for Maxwell's equations is presented. The accuracy of this new scheme is of second order accuracy in both time and space domains. The most important advantage of the scheme, compared with the conventional Yee's method, is in the value of its stability condition. The stability condition for the new FD-TD exceeds that for Yee's method by a factor 1.4 and 1.73 for two-dimensional case and three-dimensional cases, respectively. As well, there are two other important advantages of this method.

First, the new method is compatible with both the Yee's FD-TD method and the recently developed finite-element time-domain (FE-TD) method. With the help of the new scheme, the conventional FD-TD and the newer FE-TD methods can be unified. One benefit that can be realized from unifying the FD-TD and FE-TD methods is that the conforming boundary element method presented by Cangellaris [10, 11] can be simplified in the following manner. Cangellaris suggested that a few irregularly shaped quadrilateral elements are used to conform the geometry of interest while the square grids are used away from the boundary, hence, making use of the attractive feature of the finite-difference method where the index numbers of each node contain the nodal coordinates. Based on the above discussion, we suggest that, near the structure, the quadrilateral elements still be used to conform the

physical boundary, but away from the structure, the conventional Yee's method be used.

Second, the new FD-TD scheme provides greater flexibility for formulating and studying the multigrid method, variable mesh method and the method of finite difference approximations of the boundary conditions.

This chapter should not be concluded without mentioning that, although the stability condition for the new FD-TD scheme is considerably improved over that of Yee's method, the total computation efficiency of the two methods is almost the same on most current computers. This is due to the fact that, for the two dimensional TM wave case, the total operation number of the Yee's method at each time step is 15, while that of the new method is 22 (it is 46% more than Yee's method). But, with the development of parallel computation, the new method has the potential to increase the efficiency of FD-TD methods. On a multiprocessor computer (which can have tens of thousands of simple processors), the computation time mainly depends on the time it takes for the data communication between the processors. Usually this time is several tens times longer than the computation time it takes on the processors. Thus, for a fixed total computation time, because the new method needs a fewer number of time steps (this means less data communication is needed), it can improve the total efficiency of the FD-TD methods.

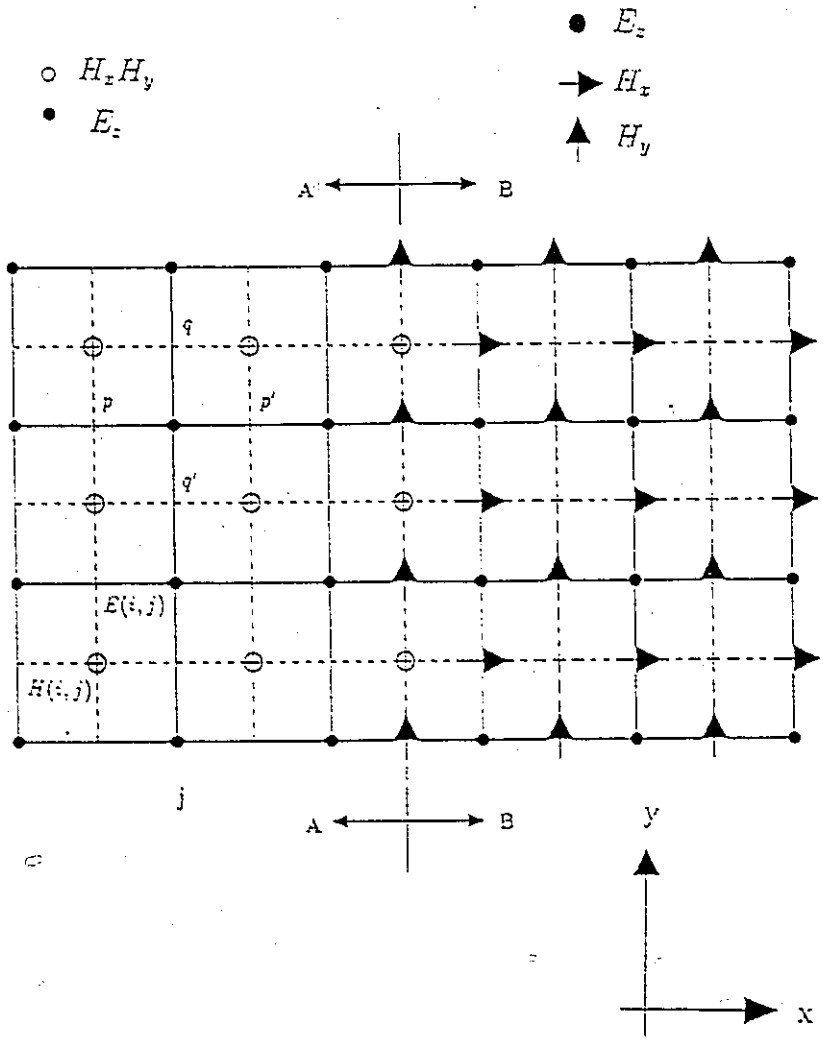

Figure 2.1: FD-TD two-dimensional lattice showing TM field placement

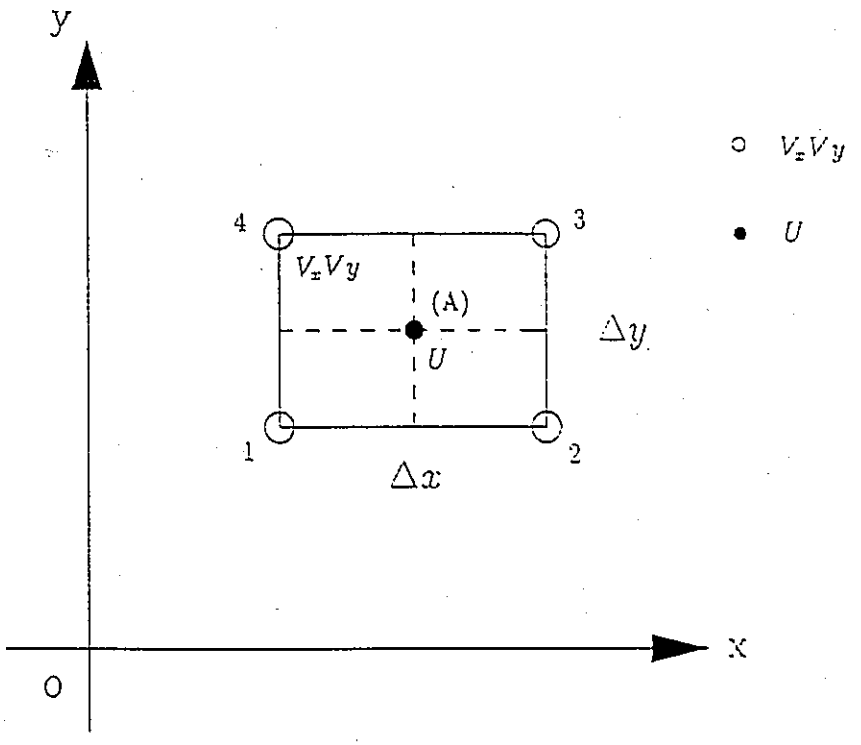

Figure 2.2: Basic lattice of the new FD-TD scheme

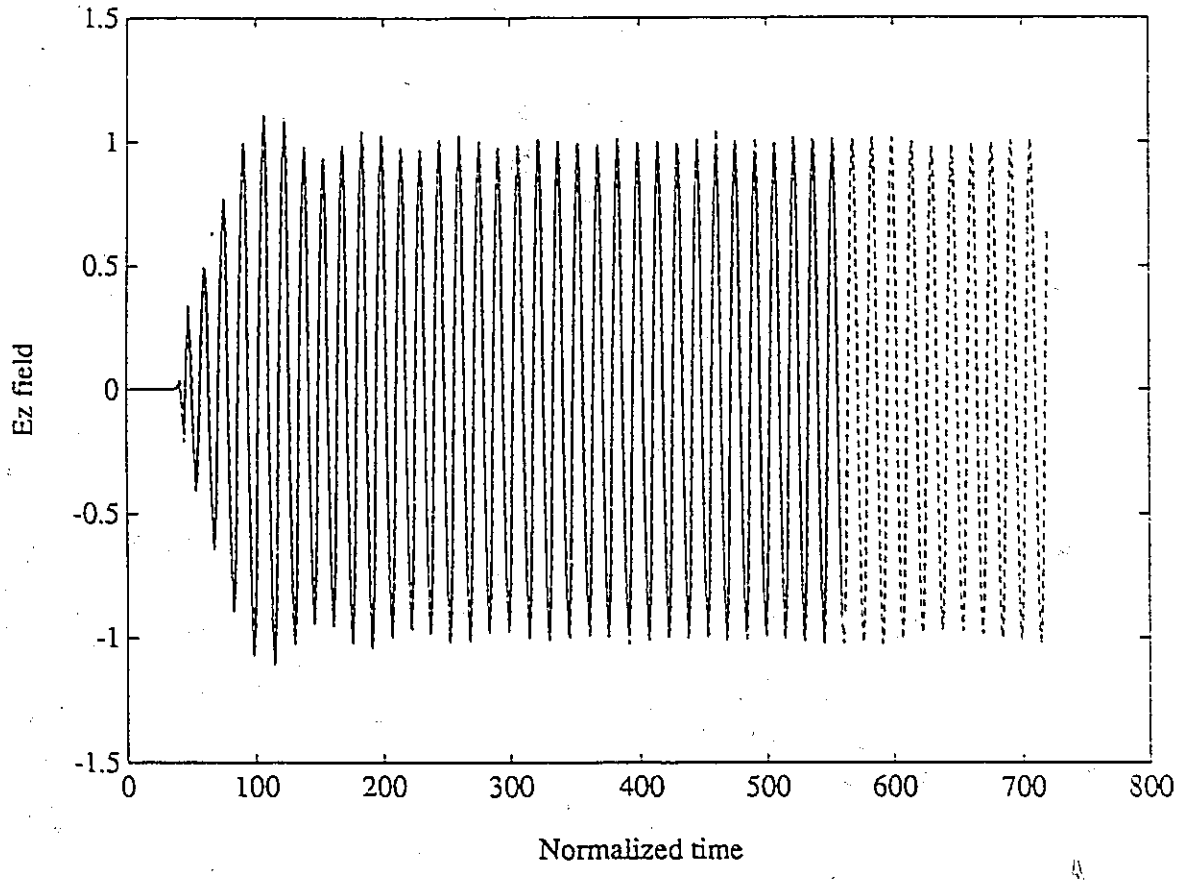

Figure 2.3: Efficiency comparison of Yee's method and the new scheme, iteration number n=800

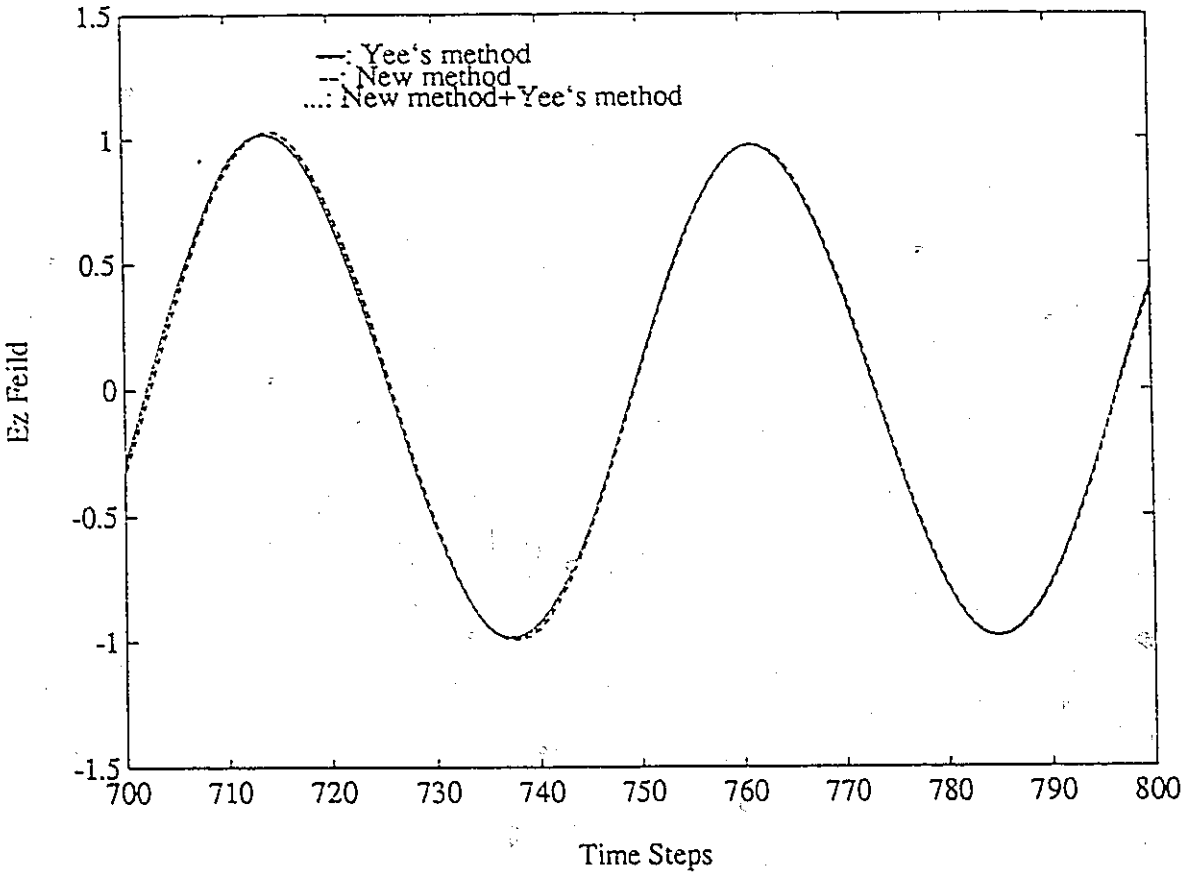

Figure 2.4: Compatibility of the new scheme and Yee's method

2.6 Appendix: Finite Element Derived Time Domain Methods

In this appendix, first, the finite element derived time domain (FE-TD) methods are reviewed. Then, their relationship with the new FD-TD method is derived. The FE-TD methods can be thought of as a hybrid approach. Its basic principle is that, in the Maxwell's equations given by (2.1) and (2.2), a finite-element basis function expansion is used to represent the spatial variations of the solution while time derivatives are approximated using central differences.

We assume that the space domain in the two dimensions has been discretized into quadrilaterals as depicted in 2.5. The electric-field nodes are represented by dots and the magnetic-field nodes by small circles. Those two sets of nodes are mutually interspaced to form two complementary meshes such that an element of the former always encloses a nodal point of the latter. We assume that $\vec{E}$ and $\vec{H}$ can be written in the general functional forms

$$\vec{E}(\bar{r},t) \approx \sum_{l=1}^{4} \phi_l(\bar{r})\vec{E}_l(t) \tag{2.24}$$

$$\vec{H}(\bar{r},t) \approx \sum_{l=1}^{4} \psi_l(\bar{r})\vec{H}_l(t), \tag{2.25}$$

where the $\vec{E}_i$'s and $\vec{H}_j$'s are the nodal values of the electric and magnetic fields, respectively, and the ϕ_i's and ψ_i's are known basis functions which allow us to describe any desirable variation of the fields within the elements. Using an appropriate definition for these functions the field within an element can be made dependent only on its values at the nodes of the element. Substituting the above functional forms into the right sides of Maxwell's equations (2.1) and (2.2) and enforcing the point matching or the collocation on both sides of the equations give

$$\frac{d\vec{H}_j}{dt} = -\frac{1}{\mu}\sum_{l=1}^{4}(\nabla\phi_l(\bar{r}))_{\bar{r}=\bar{r}_j} \times \vec{E}_l(t), \quad j = 1,2,...,N \tag{2.26}$$

$$\frac{d\vec{E}_i}{dt} = \frac{1}{\epsilon}\sum_{l=1}^{4}(\nabla\psi_l(\vec{r}))_{\vec{r}=\vec{r}_i} \times \vec{E}_l(t), \quad i = 1, 2, ..., M \tag{2.27}$$

where, N is the number of magnetic nodes, and M is the number of electric nodes. Using Yee's method as an analogy, we use central difference to approximate the time derivatives in the above two equations and we can obtain the following explicit recurrence formulas

$$\vec{H}_j^{n+\frac{1}{2}} = \vec{H}_j^{n-\frac{1}{2}} - \frac{\Delta t}{\mu}\sum_{l=1}^{4}(\nabla\phi_l(\vec{r}))_{\vec{r}=\vec{r}_j} \times \vec{E}_l^n, \quad j = 1, 2, ..., N \tag{2.28}$$

$$\vec{E}_i^{n+1} = \vec{E}_i^n + \frac{1}{\epsilon}\sum_{l=1}^{4}(\nabla\psi_l(\vec{r}))_{\vec{r}=\vec{r}_i} \times \vec{E}_l^{n+\frac{1}{2}}, \quad i = 1, 2, ..., M. \tag{2.29}$$

Formula (2.28) and (2.29) are the basic equations for the FE-TD method. The element is not limited to the shape of Fig. 2.5. It can be other forms of quadrilaterals or triangles [9]-[11]. But, in the following discussion of the finite element we only consider the quadrilaterals in Fig. 2.5.

The arbitrary quadrilateral is very attractive not only because of its conforming ability but mainly due to a very special interpolation scheme associated with it, which is called the isoparametric quadrilateral. Its construction involves two successive steps: (i) bilinear interpolation in natural coordinates ξ and η on the unit square; (ii) mapping of the unit square into a general quadrilateral in x and y coordinates. The bilinear interpolation function on the square element in the natural coordinates ξ and η (Fig. 2.6a)is given by

$$\phi(\xi, \eta) = \sum_{i=1}^{4} N_i(\xi, \eta)\phi_i \tag{2.30}$$

where

$$N_i(\xi, \eta) = \frac{1}{4}(1 + \xi\xi_i)(1 + \eta\eta_i), \quad i = 1, ..., 4 \tag{2.31}$$

and ϕ_i's are the nodal values.

The mapping from the natural coordinates to the x and y coordinates (Fig. 2.6b) is given by:

$$\begin{cases} x = \sum_{i=1}^{4} N_i(\xi, \eta)x_i \\ y = \sum_{i=1}^{4} N_i(\xi, \eta)y_i \end{cases} \tag{2.32}$$

where $N_i(\xi,\eta)$, i=1,...4, are also given by (2.31). The importance of this nonlinear mapping is well illustrated in Fig. 2.6c. First notice that ξ and η form a curvilinear coordinate system in the $(x-y)$ plane where the quadrilateral lies. The origin of the natural coordinate system is mapped onto the center of gravity of the quadrilateral. Finally, since the variation of x and y is a linear function of ξ and η along the sides, the resulting interpolation function will also have a linear variation on the same paths. Hence, the isoparametric quadrilateral is a C^0 element as a linear function is uniquely determined by two points which are common to two adjacent elements. The disadvantage of the isoparametric quadrilateral is that because of the non-linearity of the mapping functions N_i's, equation (2.32) cannot be inverted to express interpolation function (2.30) directly in terms of x and y. Therefore for a given point (x,y), one has to solve the above non-linear equations in order to obtain the corresponding natural coordinates ξ and η. This can be achieved by using the Newton-Raphson method [11].

The differentiation of element interpolation function can be calculated in the following way. Differentiating $N_i(\xi,\eta)$ with respect to ξ and η, we get

$$\begin{bmatrix} \frac{\partial N_i}{\partial \xi} \\ \frac{\partial N_i}{\partial \eta} \end{bmatrix} = \begin{bmatrix} \frac{\partial x}{\partial \xi} & \frac{\partial y}{\partial \xi} \\ \frac{\partial x}{\partial \eta} & \frac{\partial y}{\partial \eta} \end{bmatrix} \begin{bmatrix} \frac{\partial N_i}{\partial x} \\ \frac{\partial N_i}{\partial y} \end{bmatrix} = [J] \begin{bmatrix} \frac{\partial N_i}{\partial x} \\ \frac{\partial N_i}{\partial y} \end{bmatrix}. \tag{2.33}$$

where J is the Jacobian of the transformation. Solving for $\frac{\partial N_i}{\partial x}$ and $\frac{\partial N_i}{\partial y}$, we get

$$\begin{bmatrix} \frac{\partial N_i}{\partial x} \\ \frac{\partial N_i}{\partial y} \end{bmatrix} = [J]^{-1} \begin{bmatrix} \frac{\partial N_i}{\partial \xi} \\ \frac{\partial N_i}{\partial \eta} \end{bmatrix}. \tag{2.34}$$

In the above equation, the natural coordinates for a given point (x,y) are computed using Newton Raphson iteration. Once $\frac{\partial N_i}{\partial x}$ and $\frac{\partial N_i}{\partial y}$ are known, the derivatives $\frac{\partial \phi}{\partial x}$ and $\frac{\partial \phi}{\partial y}$ can be calculated from equation (2.30)

$$\frac{\partial \phi}{\partial x} = \sum_{i=1}^{4} \frac{\partial N_i}{\partial x} \phi_i \tag{2.35}$$

$$\frac{\partial \phi}{\partial y} = \sum_{i=1}^{4} \frac{\partial N_i}{\partial y} \phi_i. \tag{2.36}$$

Now we check what happens for the above finite element derived time domain method when the elements are rectangulars. For a rectanguiar element (Fig. 2.7), the mapping functions simplify to

$$\begin{cases} x = (\xi + 1)\frac{\Delta x}{2} + x_1 \\ y = (\eta + 1)\frac{\Delta y}{2} + y_1. \end{cases} \tag{2.37}$$

Since the transformation is linear in this case. The above equation can be inverted

$$\begin{cases} \xi = \frac{2}{\Delta x}(x - x_1) - 1 \\ \eta = \frac{2}{\Delta y}(y - y_1) - 1. \end{cases} \tag{2.38}$$

Substitution of (2.38) into (2.30) yields

$$\begin{aligned} \phi(x,y) = \phi_1 + \frac{\phi_2 - \phi_1}{\Delta x}(x - x_1) \quad &+ \quad \frac{\phi_4 - \phi_1}{\Delta y}(y - y_1) \\ &+ \quad \frac{\phi_1 - \phi_2 + \phi_3 - \phi_4}{\Delta x \Delta y}(x - x_1)(y - y_1). \end{aligned} \tag{2.39}$$

Then it is straightforward to obtain the partial derivatives

$$\begin{cases} \frac{\partial \phi}{\Delta x} = \frac{\phi_2 - \phi_1}{\Delta x} + \frac{\phi_1 - \phi_2 + \phi_3 - \phi_4}{\Delta x \Delta y}(y - y_1) \\ \frac{\partial \phi}{\Delta y} = \frac{\phi_4 - \phi_1}{\Delta y} + \frac{\phi_1 - \phi_2 + \phi_3 - \phi_4}{\Delta x \Delta y}(x - x_1). \end{cases} \tag{2.40}$$

When (x, y) is on the center of the square, the above equation can be arranged into

$$\begin{aligned} \frac{\partial \phi}{\partial x} &= \frac{\phi_2 - \phi_1}{\Delta x} + \frac{\phi_1 - \phi_2 + \phi_3 - \phi_4}{2\Delta x} \\ &= \frac{1}{\Delta x}\{\frac{1}{2}[\phi_3 + \phi_2] - \frac{1}{2}[\phi_4 + \phi_1]\} \end{aligned} \tag{2.41}$$

$$\begin{aligned} \frac{\partial \phi}{\partial y} &= \frac{\phi_4 - \phi_1}{\Delta y} + \frac{\phi_1 - \phi_2 + \phi_3 - \phi_4}{2\Delta y} \\ &= \frac{1}{\Delta y}\{\frac{1}{2}[\phi_4 + \phi_3] - \frac{1}{2}[\phi_2 + \phi_1]\}. \end{aligned} \tag{2.42}$$

Equations (2.41) and (2.42) are exactly the same as finite difference scheme quations (2.15) and (2.16). Based on the above derivation, we can conclude that the finite element derived time domain method, when defined over a rectangular subspace and formulated using isoparametric functions, is equivalent to the new finite difference time domain method.

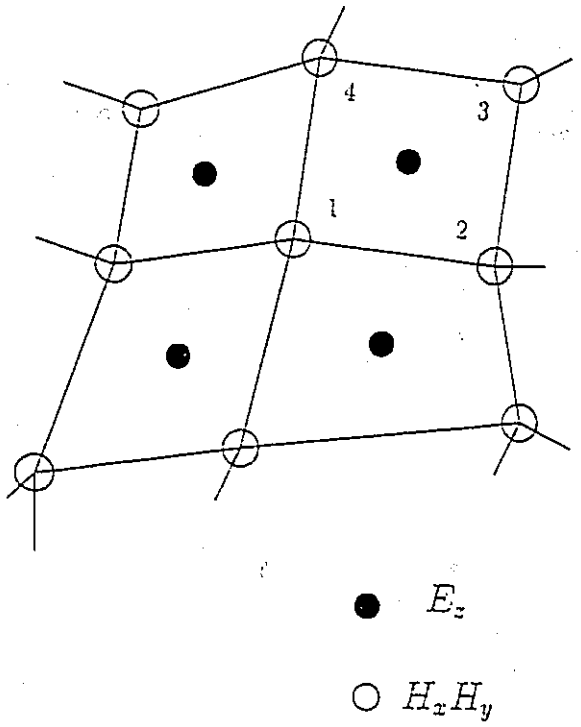

Figure 2.5: A space domain discretization of finite element time domain method

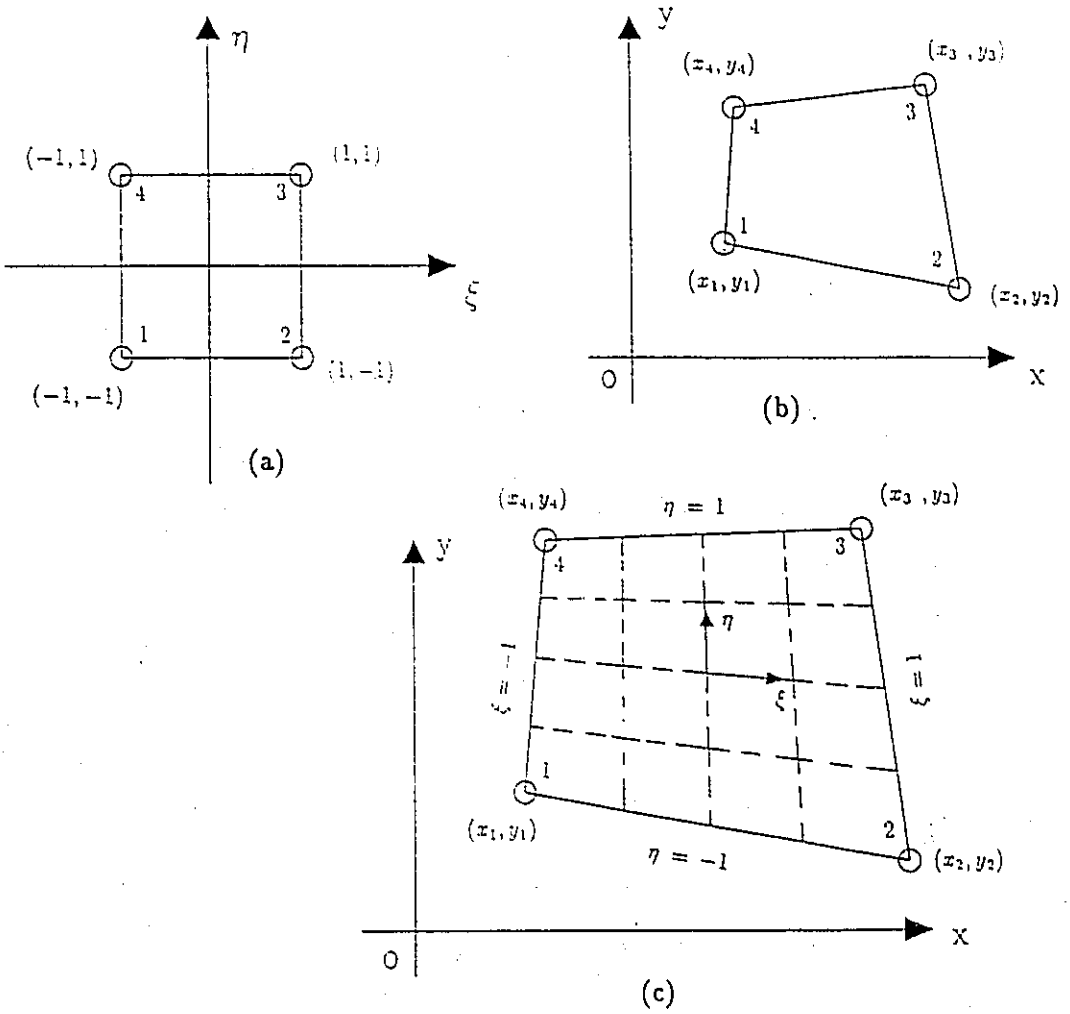

Figure 2.6: (a) and (b): Mapping from unit square on $(\xi - \eta)$ plane to a quadrilateral on the $(x - y)$ plane. (c). curvi-linear coordinate system $(\xi - \eta)$ in $(x - y)$ plane.

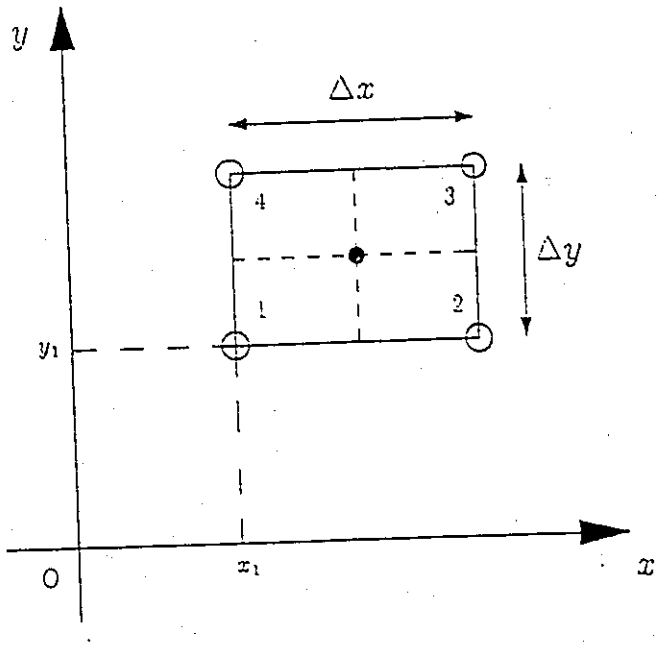

Figure 2.7: Rectangular finite element

Chapter 3

DISPERSIVE BOUNDARY CONDITIONS (DBC)

3.1 A DBC for Microstrip Component Analysis

3.1.1 Background

Recently, FD-TD methods have been used to calculate the frequency-dependent characteristic of microstrip discontinuities [51]-[53], microstrip components and simple microstrip antennas [49, 50, 54] and complex microstrip antennas [72, 73, 78, 79]. All of these calculations have shown the FD-TD method to be a very powerful tool for microstrip component and antenna analysis because it has the following two desirable attributes. First, it can be applied to problems exhibiting a complex structure which may be very difficult to solve using other analytical or numerical methods. Second, only one computation is required to get the frequency domain results over a large frequency spectrum. However, this method has one significant drawback, which is that it requires a very large computer memory, even for the analysis of very simple microstrip lines and coplanar waveguides [51]-[53]. One of the first approaches to be tried for reducing the memory requirement is to use a good absorbing boundary condition so that a smaller computational domain can be used. The authors of

earlier papers have used the one dimensional absorbing boundary condition or Mur's first order absorbing boundary condition (ABC), which is not accurate enough for microstrip analysis, especially for high dielectric constant microstrip components. The reason for this is tied to the fact that, when a Gaussian pulse travels on the microstrip line, the velocities of fields are different for different frequencies due to the dispersion properties of microstrip or coplanar lines. When applying Mur's first-order ABC it is found that it falls short of the mark because it is an effective absorber of waves at only one phase velocity or one frequency.

The objective of this section is to present a dispersive boundary condition (DBC) for microstrip component analysis, which can absorb waves over a wide frequency band. The derivation of this DBC is based on wave decomposition and on an approach that is analogous to that of Bayliss and Turkel [28]. The performance of this DBC is much better than that of the presently used Mur's first order boundary condition [49, 50, 52, 53], and its implementation is much easier compared with that of "super boundary condition" treatment of [52] and [53]. The significant improvement in performance of the present DBC compared with others will be demonstrated by carrying out a numerical analysis of a microstrip line.

3.1.2 Outline of Bayliss and Turcle's ABC

Based on Wilcox's expansion of the scattered fields [43], Bayliss and Turkel [28, 29] derived asymptotic absorbing boundary conditions in both the frequency and time domains. These absorbing boundary conditions are applicable to circular boundaries. They have been shown to be more absorbing than the boundary conditions derived by Engquist and Majda [20, 21].

In this absorbing boundary condition, it is assumed that the wave has the form [43]

$$E(\mathrm{r},t)=\sum_{i=1}^{\infty}\frac{E_i(ct-r,\theta,\phi)}{r^i} \tag{3.1}$$

in the vicinity of the box boundary. It should be noted that the above representation is intuitively obvious since the far field from a source can be expanded in terms of spherical

harmonics.

On defining an operator

$$L_i = \left(\frac{\partial}{\partial r} + \frac{1}{c}\frac{\partial}{\partial t} + \frac{i}{r}\right), \tag{3.2}$$

we can show that

$$L_i \frac{E_i(ct - r, \theta, \phi)}{r^i} = 0. \tag{3.3}$$

Hence, if we apply L_1 to (3.1), it will annihilate the first term in (3.1) and convert the other terms to higher order terms, namely,

$$L_1 E(\mathbf{r}, t) = \sum_{2}^{\infty} \frac{(1-i)E_i(ct - r, \theta, \phi)}{r^{i+1}}. \tag{3.4}$$

Consequently, $L_1 E(\mathbf{r}, t) \sim O(r^{-3})$. Similarly, it can be shown that $L_3 L_1 E(\mathbf{r}, t) \sim O(r^{-5})$ and so on. Then, on defining

$$B_m = L_{2m-1} B_{m-1}, \tag{3.5}$$

$$B_1 = L_1, \tag{3.6}$$

we have

$$B_m = \prod_{l=m}^{1} \left(\frac{\partial}{\partial r} + \frac{1}{c}\frac{\partial}{\partial t} + \frac{2l-1}{r}\right). \tag{3.7}$$

Furthermore, it is easy to show that

$$B_m E(\mathbf{r}, t) \sim O(1/r^{2m+1}). \tag{3.8}$$

In fact, B_m annihilates the first m terms in the expansion (3.1). This property is derived by carrying out formal manipulations with (3.1) and does not use any other properties of the wave equation. Hence, the relationship given by

$$B_m E(\mathbf{r}, t) = 0 \tag{3.9}$$

can be used as an absorbing boundary condition. It is good up to $O(1/r^{2m+1})$. In particular, if we assume that $m = 2$ explicitly, the boundary condition is

$$\left(\frac{\partial}{\partial r} + \frac{1}{c}\frac{\partial}{\partial t} + \frac{3}{r}\right)\left(\frac{\partial}{\partial r} + \frac{1}{c}\frac{\partial}{\partial t} + \frac{1}{r}\right) E(\mathbf{r}, t) = 0. \tag{3.10}$$

The boundary condition (3.9) become increasingly more difficult to implement when m becomes large. Among these absorbing conditions, the second-order condition is the most popular and has been applied to many problems. This boundary condition can be called a *one dimensional* ABC because its derivation is based the wave decomposition along only the r direction, and because it involves only space derivatives of r. Now we are going to use the above deriving strategy to present a dispersive boundary condition.

3.1.3 Dispersive Boundary Condition (DBC)

In most FD-TD analysis of microstrip components, such as microstrip lines, basic microstrip discontinuities and microstrip antennas, the major direction of the power flow is in the waveguided direction (for a microstrip line, in the metal strip direction). The sideways leakage and radiation are small due to the guiding nature of the metal strip and the high-dielectric constant of the substrate. This is quite similar to the one dimensional propagation case. Based on the above observation, papers [50, 52, 53] use the following one dimensional boundary condition or Mur's first order boundary condition:

$$\left(\frac{\partial}{\partial z} + \frac{1}{v_i}\frac{\partial}{\partial t}\right) E = 0, \tag{3.11}$$

where E represents the tangential electric field components relative to the boundary wall and v_i represents the velocity of propagation of the fields. Since the above boundary condition can only be optimized for a wave whose frequency corresponds to the velocity, v_i, the magnitude of the energy reflected by the boundary can be quite large due to reflections at other frequencies. Here, we use the strategy used in deriving Bayliss's ABC to present a dispersive boundary condition which can absorb fields over a wide frequency band.

A dispersive wave can be decomposed into many different frequency components, i.e.

$$E(t,z) = \sum_{i=1}^{\infty} E_i(z - v_i t), \tag{3.12}$$

where each frequency component corresponds to a plane wave with velocity v_i, which is determined by the dispersion relation

$$v_i = v(f_i), \tag{3.13}$$

where f is the frequency and $v(f)$ is any form of function which depends on the analyzed structures.

On defining an operator

$$B_i = \left(\frac{\partial}{\partial z} + \frac{1}{v_i}\frac{\partial}{\partial t}\right), \tag{3.14}$$

we can show that

$$B_i E_i(z - v_i t) = 0. \tag{3.15}$$

Hence, if we apply B_1 to (3.12), it will *annihilate* the first frequency component in (3.12) and *attenuate* the other frequency components, namely,

$$B_1 E(t,z) = \sum_{i=2}^{\infty}(1 - \frac{v_i}{v_1})E_i'(z - v_i t), \tag{3.16}$$

where $(1 - v_i/v_1)$ is called as attenuation factor. Similarly, it can be shown that B_2B_1 will annihilate the first two terms in (3.11) and further attenuate the other terms, namely,

$$B_2B_1 E(t,z) = \sum_{i=3}^{\infty}(1 - \frac{v_i}{v_1})(1 - \frac{v_i}{v_2})E_i''(z - v_i t), \tag{3.17}$$

where $(1 - v_i/v_1)(1 - v_i/v_2)$ is the attenuation factor. This property is derived by applying formal manipulations to (3.12) and does not use any other properties of the wave equation. Hence, a boundary condition

$$\left(\frac{\partial}{\partial z} + \frac{1}{v_1}\frac{\partial}{\partial t}\right)\left(\frac{\partial}{\partial z} + \frac{1}{v_2}\frac{\partial}{\partial t}\right)E = 0 \tag{3.18}$$

can be used as an absorbing boundary condition, which can absorb plane waves traveling to the right with velocities v_1 and v_2. By concatenating several absorbing boundary conditions (3.14), the number of the absorption velocities can be increased. If v_1 and v_2 are determined by the dispersion relation $v = v(f)$, boundary condition (3.18) becomes a multi-frequency absorbing boundary condition or a dispersive boundary condition (DBC).

3.1.4 The Relationship between the Proposed DBC and Key and Higdon's ABC

Keys and Higdon's angle absorbing boundary condition [30]-[32] can also be described in terms of the dispersive boundary condition (3.18). In their work, they choose the velocity v in (3.18) according to the relation $v_i = c/\cos\theta_i$, where c is the propagation velocity of wave, and θ_i is the incident angle of the wave with respect to the z-axis. The reason they can make this choice for the phase velocity is due to the following: A plane wave with velocity c and angle θ can be expressed as

$$E(t,z) = E(ct - z\cos\theta) = E(\frac{c}{\cos\theta}t - z) \tag{3.19}$$

along the z-axis. Moreover, an arbitrary wave can be decomposed into a summation of plane waves with different angles, i.e.:

$$E(t,z) = \sum_i E_i(ct - z\cos\theta_i) = \sum_i E_i(\frac{c}{\cos\theta_i}t - z). \tag{3.20}$$

This new description gives a one-dimensional interpretation to Key and Higdon's ABC. That is, the waves from different angles are first mapped into the waves traveling along the z-axis with corresponding velocities, then the waves with different velocities in one dimension are absorbed. So, based on this discussion, Key and Higdon's ABC can also be thought as a *one dimensional* ABC.

3.1.5 Numerical Results

The implementation of the dispersive boundary (3.18) can be realized by employing operators. Let us define the shift operators I, Z and K_z by the following:

$$\mathrm{I}E_i^n = E_i^n \tag{3.21}$$

$$\mathrm{Z}E_i^n = E_i^{n+1} \tag{3.22}$$

$$\mathrm{K}_z E_i^n = E_{i+1}^n \tag{3.23}$$

where i is the space position index and n is the time index. The difference equation for (3.11) is given by:

$$E_M^n - E_{M-1}^{n-1} - \gamma_i(E_M^{n-1} - E_{M-1}^n) = 0 \tag{3.24}$$

where

$$\gamma_i = \frac{1-\rho_i}{1+\rho_i} \tag{3.25}$$

$$\rho_i = \frac{v(f_i)\Delta t}{\Delta z}, \tag{3.26}$$

E_M represents the tangential electric field component on the boundary and E_{M-1} represents the tangential electric field component a distance of one node inside the boundary. The boundary condition (3.24) can be expressed by the operators:

$$[\mathrm{I} - \mathrm{Z}^{-1}\mathrm{K}_z^{-1} - \gamma_i(\mathrm{Z}^{-1} - \mathrm{K}_z^{-1})]E_M^n = 0 \tag{3.27}$$

or

$$\mathrm{B}_i E_M^n = 0 \tag{3.28}$$

where,

$$\mathrm{B}_i = \mathrm{I} - \mathrm{Z}^{-1}\mathrm{K}_z^{-1} - \gamma_i(\mathrm{Z}^{-1} - \mathrm{K}_z^{-1}) \tag{3.29}$$

is defined as the difference boundary operator. The difference boundary operator $\mathbf{B}$ for the dispersive boundary condition given by (3.18) can be obtained in the following way:

$$
\begin{aligned}
\mathrm{B} &= \mathrm{B_1 B_2} \\
&= [\mathrm{I} - \mathrm{Z}^{-1}\mathrm{K}_z^{-1} - \gamma_1(\mathrm{Z}^{-1} - \mathrm{K}_z^{-1})][\mathrm{I} - \mathrm{Z}^{-1}\mathrm{K}_z^{-1} - \gamma_2(\mathrm{Z}^{-1} - \mathrm{K}_z^{-1})] \\
&= \mathrm{I} - 2\mathrm{Z}^{-1}\mathrm{K}_z^{-1} + \mathrm{Z}^{-2}\mathrm{K}_z^{-2} + \gamma_1\gamma_2(\mathrm{Z}^{-2} - 2\mathrm{Z}^{-1}\mathrm{K}_z^{-1} + \mathrm{K}_z^{-2}) \\
&\quad -(\gamma_1 + \gamma_2)(\mathrm{Z}^{-1} - \mathrm{K}_z^{-1} - \mathrm{Z}^{-2}\mathrm{K}_z^{-1} + \mathrm{Z}^{-1}\mathrm{K}_z^{-2}). \qquad (3.30)
\end{aligned}
$$

From the above boundary operator, we can obtain the final second-order dispersive boundary condition:

$$
\begin{aligned}
E_M^n &= 2E_{M-1}^{n-1} - E_{M-2}^{n-2} \\
&+ (\gamma_1 + \gamma_2)(E_M^{n-1} - E_{M-1}^n - E_{M-1}^{n-2} + E_{M-2}^{n-1}) \\
&- \gamma_1\gamma_2(E_M^{n-2} - 2E_{M-1}^{n-1} + E_{M-2}^n). \qquad (3.31)
\end{aligned}
$$

Using the above dispersive boundary condition, we carry out an analysis on a microstrip line. Fig. (3.1) gives the effective dielectric constant calculated using the FD-TD method. The analysis is carried out by applying both the dispersive boundary condition and Mur's first-order boundary condition at the ends of the microstrip line, while at the remaining walls we only use Mur's first-order boundary condition. The curve identified by crosses was obtained by using a computation domain which is as large as that used in [51] so that the time domain data can be truncated before reflections from the boundary occur. This is an exact result in the sense that it is free of any boundary effects. The curve identified by circles was obtained by using the DBC and using only one third of the former computation domain. In the DBC, the velocities v_1 and v_2 were determined by using values 7.12 and 8.50, respectively, for the effective dielectric constants. The above two lines overlap exactly in this figure. The dashed line results from using Mur's first order ABC and the smaller computation domain. In Mur's first-order ABC, the velocity is determined by using an effective dielectric constant of 7.12. It follows from this that the DBC leads to

greatly reduced computation memory requirements. In Fig. (3.2) is shown a propagating E_x-pulse in the time domain, as well as a residual signal due to reflections at the boundary of the computation domain for both DBC and Mur's boundary condition. In the DBC, $\epsilon_{reff1} = 7.12$ and $\epsilon_{reff2} = 8.50$ are used to determine the two velocities. In Mur's first-order ABC, $\epsilon_{reff} = 7.12,\ 8.12$ are used to determine the velocity, respectively. From this result we see that in the time domain the reflections from the computation domain boundary are greatly reduced using DBC: in fact, DBC reflections are an order of magnitude less than those from the first-order boundary conditions. The numerical reflection coefficients for both DBC and the first-order boundary conditions are given in Fig. (3.3). This figure shows that DBC absorbs the wave over a large frequency band, i.e. the reflection coefficient is less than -45 dB from 0 to 20 GHz, where $\epsilon_{reff1} = 7.12$ and $\epsilon_{reff2} = 8.50$ are used for the DBC. For the first-order condition, the reflection coefficients are less than -45 dB only over the ranges from 0 to 3 GHz when $\epsilon_{reff} = 7.12$, or from 5 to 8 GHz when $\epsilon_{reff} = 8.12$.

3.1.6 Conclusion

The dispersive boundary condition allows the dispersive properties of waves to be incorporated into the design of an absorbing boundary condition. This feature can be very useful when the dispersion for a major outgoing wave is known. Both the validity and the efficiency of the DBC have been demonstrated by carrying out analyses on a microstrip line. With DBC, the memory requirement for FD-TD analyses of microstrip circuits and antennas can be greatly reduced.

The main difference between DBC and ABC is that DBC is designed to optimize the boundary condition according to the dispersive characteristics of the waves, while ABC is designed to optimize the boundary condition according to the propagation direction of the waves. The introduction of the concepts which are the basis of DBC is specially important

for the study of absorption for strongly dispersive waves, such as occurs in conductor waveguides and dielectric waveguides. Further applications of the proposed DBC to waveguide component analysis will be investigated in the next section. Based on the ideas presented in this paper, some ABCs can be modified into DBCs.

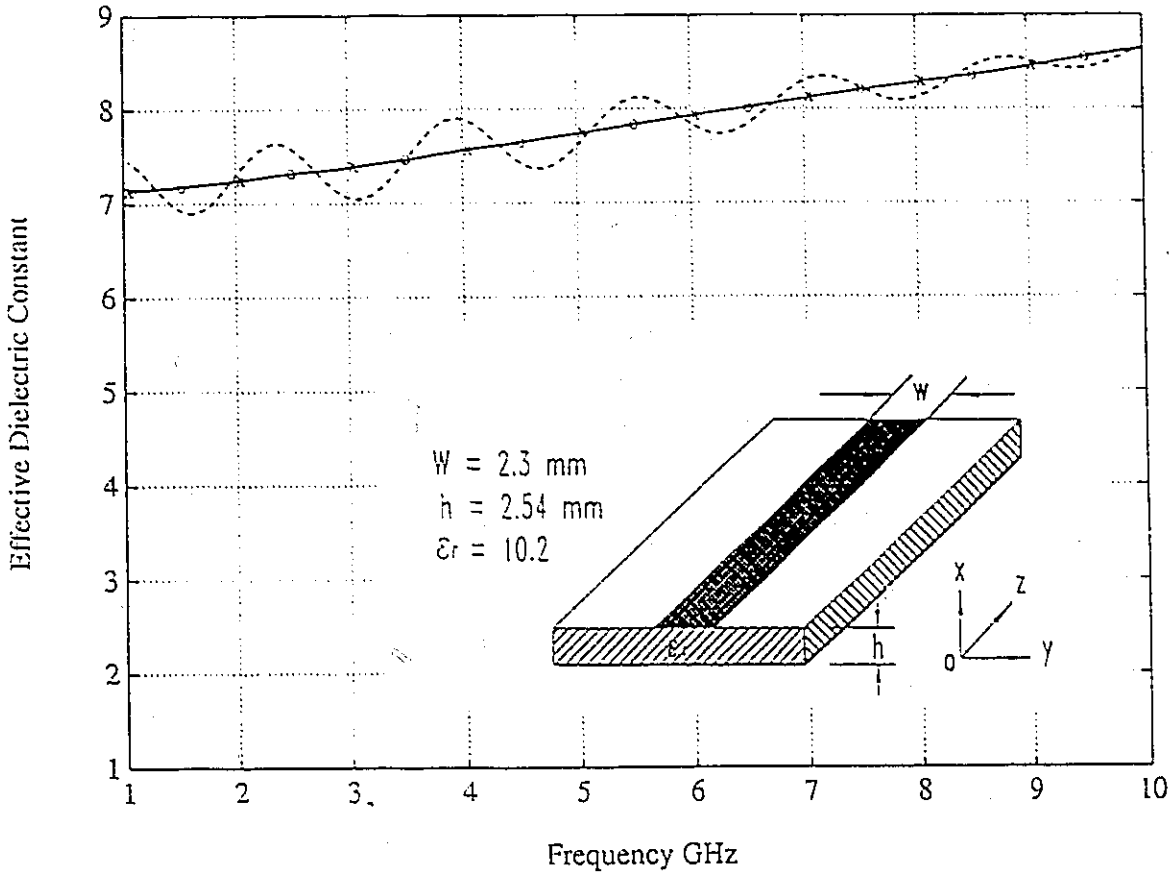

Figure 3.1: Effective dielectric constant of a microstrip line. The cross dotted line: Using very large computation domain. The circular dotted line: Using DBC and smaller computation domain. The dashed line: Using Mur's first order ABC and smaller computation domain.

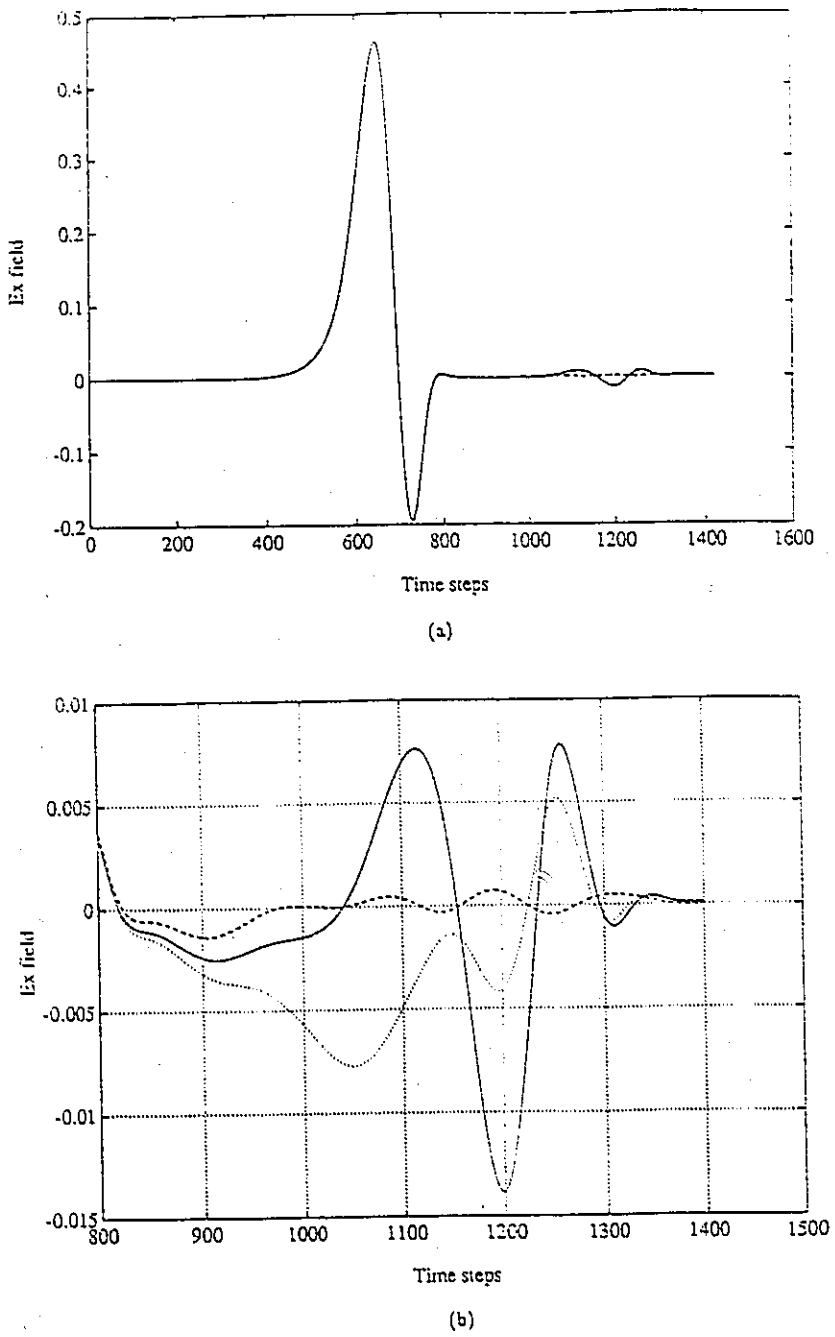

Figure 3.2: Field reflection in time domain due to boundary conditions. (a). Incident waves and reflected waves from the boundary conditions. Solid line: first order Mur's ABC, $\epsilon_{reff} = 7.12$; Dashed line: DBC, $\epsilon_{reff1} = 7.12$ and $\epsilon_{reff2} = 8.50$. (b). Reflected waves from the boundary conditions. Solid line: first order ABC, $\epsilon_{reff} = 7.12$; Dotted line: first order ABC, $\epsilon_{reff} = 8.12$; Dashed line: DBC, $\epsilon_{reff1} = 7.12$ and $\epsilon_{reff2} = 8.50$.

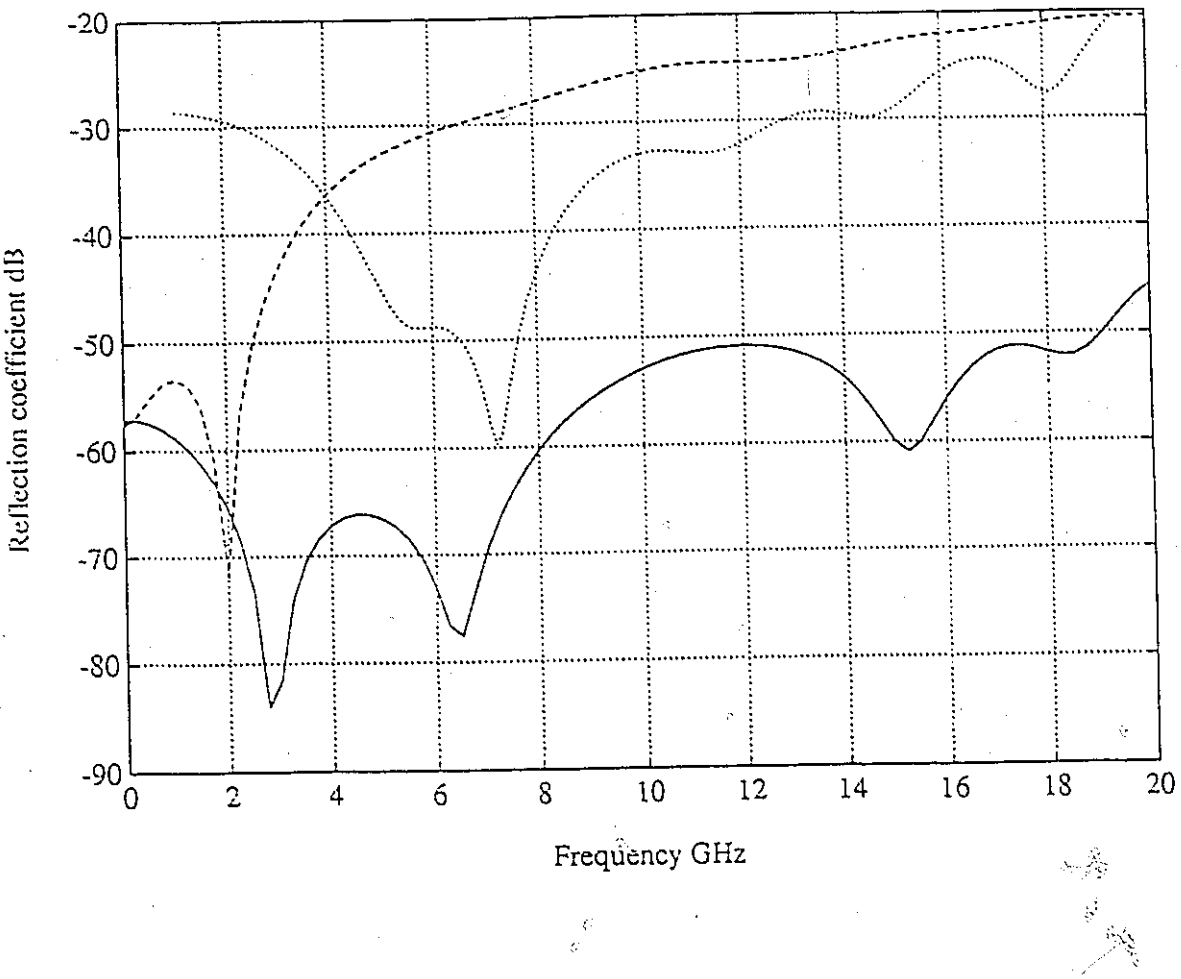

Figure 3.3: Numerical experiment reflection coefficients for a microstrip line. Dashed line: first order ABC, $\epsilon_{reff} = 7.12$; Dotted line: first order ABC, $\epsilon_{reff} = 8.12$; Solid line: DBC, $\epsilon_{reff1} = 7.12$ and $\epsilon_{reff2} = 8.50$.

3.2 Waveguide Component Analysis Using DBC

3.2.1 Background

Recently, the FD-TD method has been used to calculate the properties or characteristics of waveguide components [65]-[68], [71]. All of these calculations have shown the FD-TD method to be a very powerful tool for waveguide component analysis because it can easily be adapted to complex geometries which may be very difficult to solve using other analytical or numerical methods. However, most of the papers are limited to using monochromatic waves as the excitation in waveguide analysis. This means that the analysis has to be repeated for each frequency of interest. So, this strikes a blow at one of the most important advantages of time domain methods (FD-TD and TLM methods), which is that, by using a pulse as excitation, only one computation is required to get the frequency domain results over a large frequency spectrum. The reason that earlier workers chose a monochromatic wave, rather than a pulse of some selected shape as the excitation, is because of the lack of a good dispersive absorbing boundary condition which could be used with the FD-TD method. That is, one that could absorb waves propagating on the FD-TD grid over a wide frequency band. Oliver and McNamara [66] have responded to this limitation and have presented a dispersive boundary condition. It is found that the performance of the DBC they used does not meet the requirements demanded that must be met for carrying out highly accurate analyses. Recently, Alinikula and Kunz [68] used a pulse as the excitation in their analysis and tried to improve the efficiency of the FD-TD technique for waveguide component analysis. It will be shown that their results suffer from large inaccuracies because the boundary condition they used only absorbed waves in a very narrow part of

the dominant mode bandwidth (although they state the reflections due to the absorbing boundary condition (ABC) are less than -35 dB to -50 dB over 80% of the dominant mode frequency range, it will be shown that this performance can be obtained for that ABC at only less than 20% of the dominant mode frequency bandwidth.).

The objective of this section is to apply the dispersive absorbing boundary condition (DBC) developed in the last section for microstrip component analysis, a case where dispersion is weak, to a strongly dispersive case which occurs in conductor waveguides. This DBC will allow a pulse to be used as the excitation, thereby greatly improving the efficiency of the FD-TD method. The significant improvements brought about by the use of the DBC for waveguide component analysis will be demonstrated with both theoretical and numerical results.

3.2.2 Reflection Coefficient for Dispersive Boundary Conditions

It would not have been possible for the ordinary angle absorbing boundary condition (ABC) theory to have been developed so well if the reflection coefficient, R_{ABC}, had not been used to evaluate the performance of an ABC. Like ABC, the reflection coefficient for DBC, R_{DBC}, has to be formulated before we can carry out a study of DBC.

It is known [17, 27] that the performance of a given ABC can be assessed by deriving a reflection coefficient R, which quantifies the nonphysical reflection of a plane wave, as a function of incident angle θ, when it interacts with the grid boundary. Clearly, a good ABC gives a small value of R over a wide range of θ. Like ABC, the DBC can also be evaluated by the corresponding reflection coefficient R. But, for DBC, the reflection coefficient is a function of the frequency, rather than the incident angle. A good DBC should give a small value of R over a wide range of frequencies. The reflection coefficient R is defined as the ratio of the reflected wave field to an incident plane wave. Consider a wave traveling to the

right. The wave has the form

$$E_{in} = e^{j(\omega t - kz)}. \tag{3.32}$$

When this wave strikes an artificial boundary, it produces the total wave field

$$E_{tot} = e^{j(\omega t - kz)} + Re^{j(\omega t + kz)}, \tag{3.33}$$

where R is the reflection coefficient. This wave field satisfies the boundary condition so that R can be determined by substituting E_{tot} into the boundary condition equation. By substituting expression (3.33) into (3.11) and (3.18), the reflection coefficient expressions as a function of frequency are obtained for ABC (3.11) and DBC (3.18). They are, respectively,

$$R_{ABC} = \frac{-kv_i + \omega}{kv_i + \omega} \tag{3.34}$$

and

$$\begin{aligned} R_{DBC} &= \left(\frac{-kv_1 + \omega}{kv_1 + \omega}\right)\left(\frac{-kv_2 + \omega}{kv_2 + \omega}\right) \\ &= \prod_{i=1}^{2}\left(\frac{-kv_i + \omega}{kv_i + \omega}\right) \end{aligned} \tag{3.35}$$

where the propagation constant, k, is governed by the dispersion relation for the wave

$$k = k(\omega). \tag{3.36}$$

From expressions (3.34) and (3.35), it can be seen that the reflection coefficient for DBC is directly coupled with the dispersion relation. To continue the discussion of the evaluation for the DBC, based on the reflection coefficient, let us consider the dispersion relation of the dominant waveguide mode, TE_{10}, for our reflection coefficient calculation. The amplitudes of reflection coefficients for ABC (3.11), DBC (3.18) and the DBC used in [66] are shown in Fig. 3.4, where k_0 is the free space propagation constant, and w is width of the waveguide. The dashed lines are for ABC (3.11), the dotted line for the DBC [66] and the solid line for DBC (3.18). From this result, it can be seen that the

ABC (3.11) or Mur's first order ABC is a good absorber over only a very narrow range of frequencies. However, DBC (3.18) is effective over almost the total frequency band of the TE_{10} mode. The reflection due to this DBC is less than -40 dB for almost the whole TE_{10} mode frequency band. The performance of DBC [66] is not as good as that of DBC (3.18).

3.2.3 Numerical Results

To test the validity of the DBC (3.18) for waveguide component analysis, we carry out an analysis for a homogeneous waveguide. We use an electric wall to launch the wave down the waveguide. The incident transverse electric field on the excitation plane is forced to be a TE_{10} mode field distribution so that the wave that is launched approximates the TE_{10} mode. The incident time-domain field is a sinusoid with a centre frequency ω_0 which is modulated by a Gaussian pulse. The width of the Gausssian pulse is selected so that its spectrum fills and overlaps the frequency band in which only the dominant mode can propagate. In the calculation, the wide side of the waveguide is divided into 20 space steps, and the 5% Gaussian pulse width is chosen to be about 140 space steps. At the end of the waveguide, DBC (3.18) and ABC (3.11) are applied, respectively. In Fig. 3.5 are shown the time domain results. Fig. 3.5a shows a sinusoidal signal, modulated by a Gaussian envelope, propagating in a very long waveguide. Fig. 3.5b shows the reflected wave for ABC (3.11), and Fig. 3.5c shows the reflected wave corresponding to DBC (3.18). From this, we see that in the time domain the reflections from the computation domain boundary are greatly reduced using DBC (3.18). The numerical reflection coefficients for both DBC (3.18) and ABC (3.11) are given in Fig. 3.6. This figure further shows that DBC (3.18) is effective over 80% of the frequency band corresponding to the dominant mode for waveguides, i.e. the reflection coefficient is less than -40 dB over this range of frequencies. For ABC (3.11), the reflection coefficient is less than -40 dB over only 10% of the frequency band occupied by the dominant waveguide mode.

3.2.4 Conclusion

The dispersive absorbing boundary condition (DBC) presented in the last section for microstrip component analysis, where the dispersion is weak and where very good results have been obtained, is applied to the strongly dispersive case which occurs in conductor waveguides. The excellent absorbing quality of the DBC for strongly dispersive waves has been demonstrated by both theoretical and numerical results. The reflection coefficient is formulated for the dispersive boundary condition. With the help of this theoretical reflection coefficient, other dispersive boundary conditions can be more easily investigated and developed. One immediate benefit that can be realized from using the formulated reflection coefficient is that the DBC presented in [66] has been analyzed theoretically and has been further developed in the next section.

The workers using Transmission Line Method (TLM) have been trying to find an absorbing boundary condition to absorb the strongly dispersive waves occurring in conductor waveguides for several years [39]-[41]. In the boundary condition they proposed, convolution integrals are employed. Since these convolutions are applied to every nodal on the boundary, for every time step, this boundary condition is very time consuming and requires a large memory. Also, it should be noted that Simons [42] has demonstrated that the absorbing boundary conditions developed for FD-TD method can be applied to the TLM based on an established relation between the FD-TD and TLM methods. Using a method similar to that in [42], the dispersive boundary condition discussed in this section can also be applied to the TLM, and its implementation is much more efficient than that of the method discussed in [39]-[41] in terms of computation time and memory requirement. We have carried out a test that shows this DBC can be easily applied to the FD-TLM method [56].

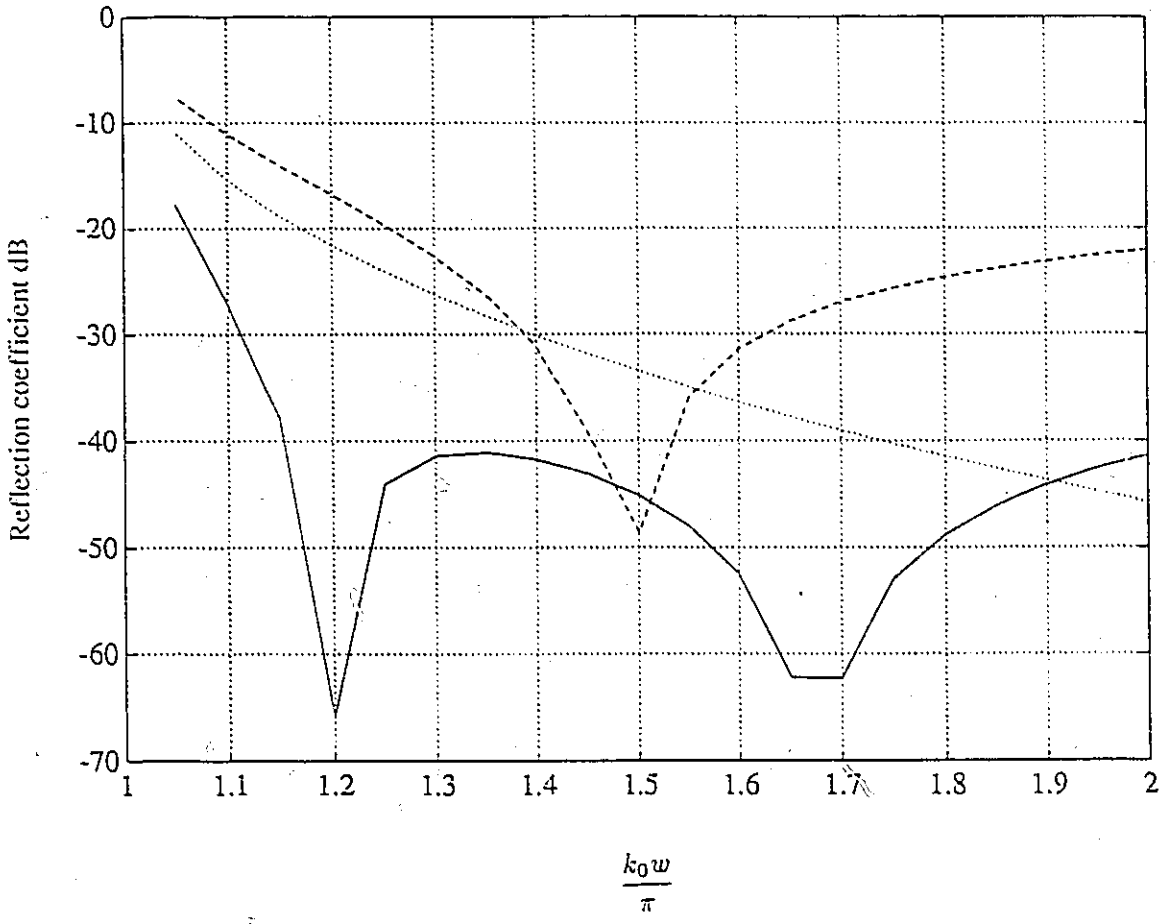

Figure 3.4: Theoretical reflection coefficients of DBC's and ABC. Dashed line: Mur's first order ABC; Dotted line: DBC [66. Oliver]; Solid line: DBC (3.18).

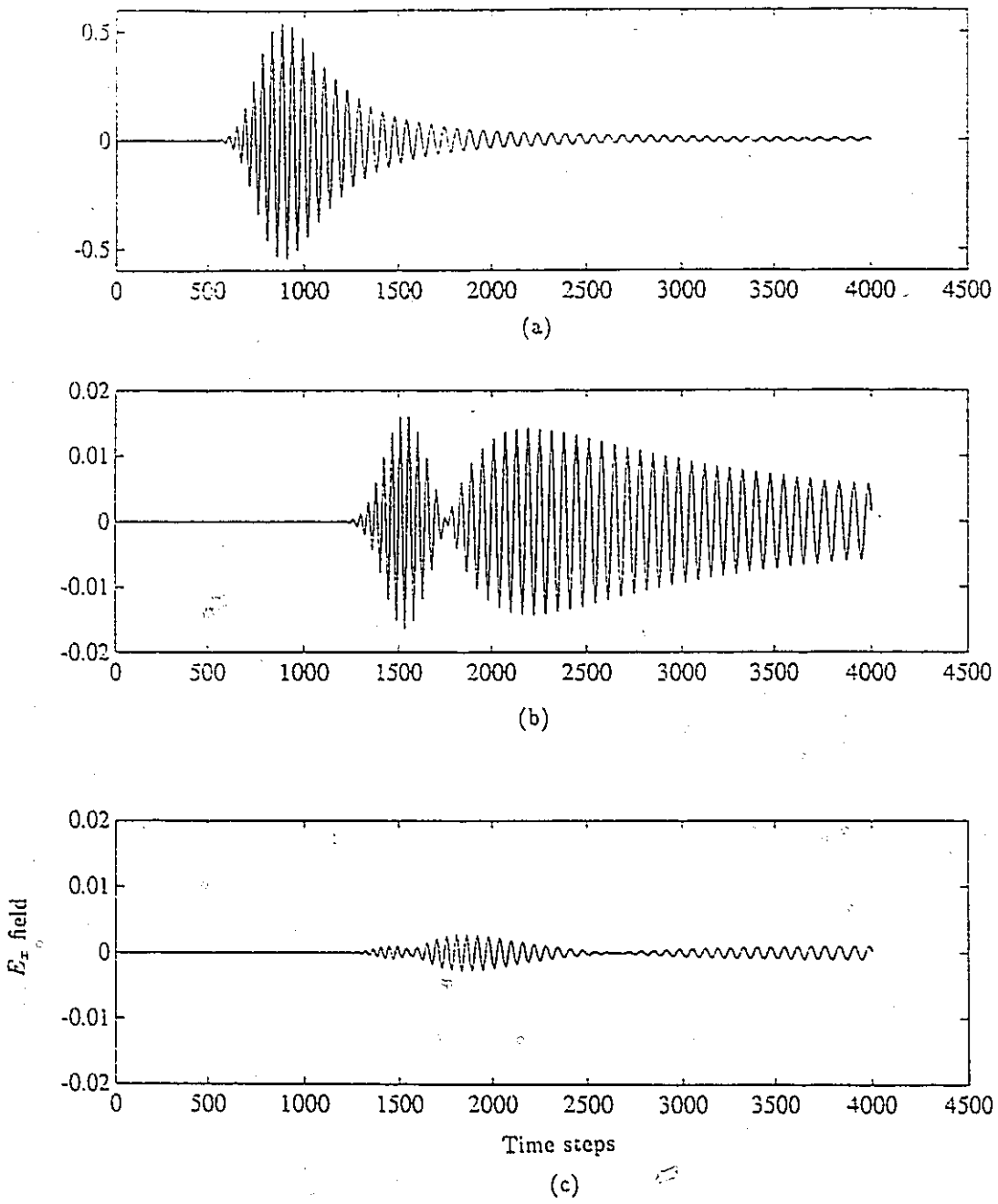

Figure 3.5: Field reflections in time domain due to DBC's and ABC. (a). Incident wave; (b). Reflected wave due to Mur's first order ABC: (c). Reflected wave due to DBC (3.18)

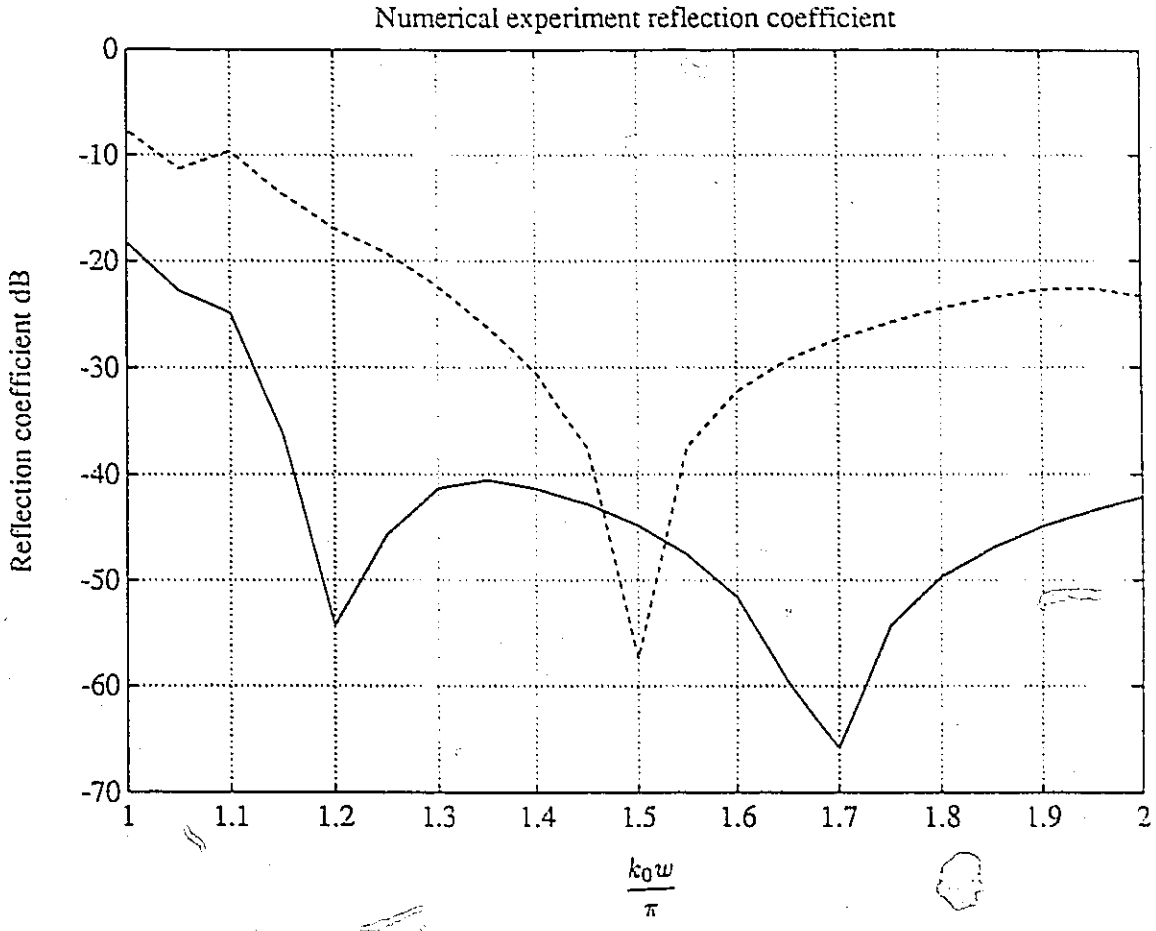

Figure 3.6: Numerical experiment reflection coefficients. Dashed line: Mur's first order ABC; Solid line: DBC (3.18)

3.3 A One-Way Dispersive Boundary Condition (DBC)

In this section, we will, using the formulated reflection coefficient for DBC in the last section, as well the approximation techniques developed in deriving an ordinary angle one-way *absorbing boundary condition* (ABC), systematically generalize and develop a one-way DBC. This one-way DBC is intended to be used for waveguide component analysis.

3.3.1 A One-way Dispersive Boundary Condition (DBC)

For a plane wave traveling to the right, the equation that must be satisfied in the frequency domain is

$$\frac{\partial \mathrm{E}(z,\omega)}{\partial z} + jk(\omega)\mathrm{E}(z,\omega) = 0 \tag{3.37}$$

where the $e^{j\omega t}$ time dependence is assumed, and $k(\omega)$ is the propagation constant. For a non-dispersive wave or TEM wave, $k(\omega) = \omega/v$, where v is the propagation velocity of the wave. Substituting this value for $k(\omega)$ into (3.37) and performing the inverse Fourier transform on the equation, we get the exact absorbing boundary condition for a non-dispersive wave or a TEM wave, which is equivalent to Mur's first order ABC. But, for a dispersive wave, since the propagation constant, $k(\omega)$, is not such a simple function of ω, the inverse Fourier transform cannot be performed to obtain an exact analytical absorbing boundary condition. Oliver and McNamara [66] suggested using the Padé series to approximate the square root in $k(\omega)$. Then, the inverse Fourier transform can be performed to obtain an approximate absorbing boundary condition for dispersive wave, i.e. to obtain a DBC. We note that this kind of approximation to the square root is very similar to the approximation to the

square root performed in deriving the one-way ordinary angle absorbing boundary condition [24, 25]. In the following, we will adapt the approximation techniques developed in deriving one-way ABCs and use the reflection coefficient formulated for DBC to further investigate and develop this class of DBCs.

Without jeopardizing the general validity of the theory in any way, a TE_{10} mode dispersion relation of waveguide filled with free space is chosen for the following discussion. The propagation constant for the TE_{10} mode is

$$\begin{aligned} k(\omega) &= \frac{\omega}{c}\left[1-\left(\frac{\omega_c}{\omega}\right)^2\right]^{1/2} \\ &= \frac{\omega}{c}\sqrt{1-s^2} \end{aligned} \tag{3.38}$$

where c is the propagation velocity of the wave in free space, ω_c is the cut off frequency of the TE_{10} mode, and $s = \omega_c/\omega$. A generalized approximation to $\sqrt{1-s^2}$ on the interval $s \subset [0,1]$ by a rational function can be written as [24, 25]

$$\sqrt{1-s^2} \approx r(s) = \frac{P_m(s)}{Q_n(s)}, \tag{3.39}$$

where P_m and Q_n are polynomials of degree m and n, respectively, and $r(s)$ is said to be of type (m,n). By specifying $r(s)$ as a general type $(2,0)$ approximant, the radical is approximated by an interpolating polynomial of the form

$$\sqrt{1-s^2} \approx p_0 + p_2 s^2. \tag{3.40}$$

By substituting (3.40) into (3.37) and multiplying the resultant equation throughout by $(j\omega)$, we have

$$j\omega\frac{\partial \mathbf{E}(t,\omega)}{\partial z} + p_0\frac{1}{c}(j\omega)^2\mathbf{E}(z,\omega) - p_2\frac{\omega_c^2}{c}\mathbf{E}(z,\omega) = 0. \tag{3.41}$$

Then, after performing the inverse Fourier transform on the above, one obtains the second-order approximate analytical DBC,

$$\frac{\partial^2 E(z,t)}{\partial z \partial t} + \frac{p_0}{c}\frac{\partial^2 E(z,t)}{\partial t^2} - p_2\frac{\omega_c^2}{c}E(z,t) = 0. \tag{3.42}$$

Similarly, by using the general type $(2,2)$ rational function,

$$\sqrt{1-s^2} \approx \frac{p_0 + p_2 s^2}{q_0 + q_2 s^2} \tag{3.43}$$

we get the third-order approximate analytical DBC,

$$-q_0 \frac{\partial^3 E(z,t)}{\partial z \partial t^2} + q_2 \omega_c^2 \frac{\partial E(z,t)}{\partial z} - \frac{p_0}{c} \frac{\partial^3 E(z,t)}{\partial t^3} + \frac{p_2 \omega_c^2}{c} \frac{\partial E(z,t)}{\partial t} = 0. \tag{3.44}$$

In deriving the one-way angle ABC [24, 25], the choice of the coefficients p_i and q_i is determined by the method of interpolation. Standard techniques such as Chebyshev, least-squares, or Padé approximation are applied with the goal of producing an approximate ABC whose performance is good over a wide range of incident wave angles. But, for DBCs, the coefficients p_i and q_i should be determined to optimize the performance of approximate DBC according to the dispersion relation for waves. Seven techniques of approximation are presented in detail in [24, 25]. These techniques are: Padé, Least-squares (or L^2 which minimizes the L^2 norm of the error of the approximation), interpolation at Chebyshev points, interpolation at Newman points, Chebyshev (or L^∞ which minimizes the L^∞ norm), Chebyshev-Padé (or C-P), and Chebyshev on a subinterval (or L_α^∞ which minimizes the L^∞ norm on the subinterval). In this thesis, we have concentrated on the study of type $(2,0)$ and $(2,2)$ approximate DBCs. The coefficients for seven families of type $(2,0)$ and $(2,2)$ DBCs are given in [26]. Next, by using the formulated DBC reflection coefficient, we examine the performance of these seven families of type $(2,0)$ and $(2,2)$ DBCs.

By substituting (3.33) into (3.42) and (3.44), reflection coefficient expressions are obtained as a function of frequency for the general second- and third-order DBCs (type (2,0) and type (2,2)). They are, respectively,

$$R_{(2,0)} = \frac{\omega k - \frac{p_0}{c}\omega^2 - p_2 \frac{\omega_c^2}{c}}{-\omega k - \frac{p_0}{c}\omega^2 - p_2 \frac{\omega_c^2}{c}} \tag{3.45}$$

and

$$R_{(2,2)} = \frac{-q_0 \omega^2 k - q_2 \omega_c^2 k + \frac{p_0}{c}\omega^3 + \frac{p_2 \omega_c^2}{c}\omega}{+q_0 \omega^2 k + q_2 \omega_c^2 k + \frac{p_0}{c}\omega^3 + \frac{p_2 \omega_c^2}{c}\omega} \tag{3.46}$$

where the propagation constant, $k(\omega)$, is determined by the TE_{10} mode dispersion relationship (3.38).

3.3.2 Conclusion

By using the reflection coefficient for DBC and by studying the relation between ABC and DBC, a one-way dispersive boundary condition has been generalized and developed systematically.

Figs. 3.7 and 3.8 show the behavior of the reflection coefficients for the two best-performing second- and third-order DBCs, respectively, where w is the width of the waveguide. The solid lines in the figures give the performance of Mur's first order ABC. From Figs. 3.7 and 3.8, it can be seen that, for a sinusoidal source excitation, the first order ABC should be used and the second order one-way DBC used in [67] is not sufficiently absorbent. Also, it can be seen that when a pulsed excitation is used, the performance of the second order one-way DBC used in [66] and the first order ABC used in [68] are lacking and at least a third-order one-way DBC should be used so as to guarantee accurate results in the dominant mode's bandwidth. Also, it can be seen that the third-order L_α^∞ DBC performs much better than the third-order Padé DBC.

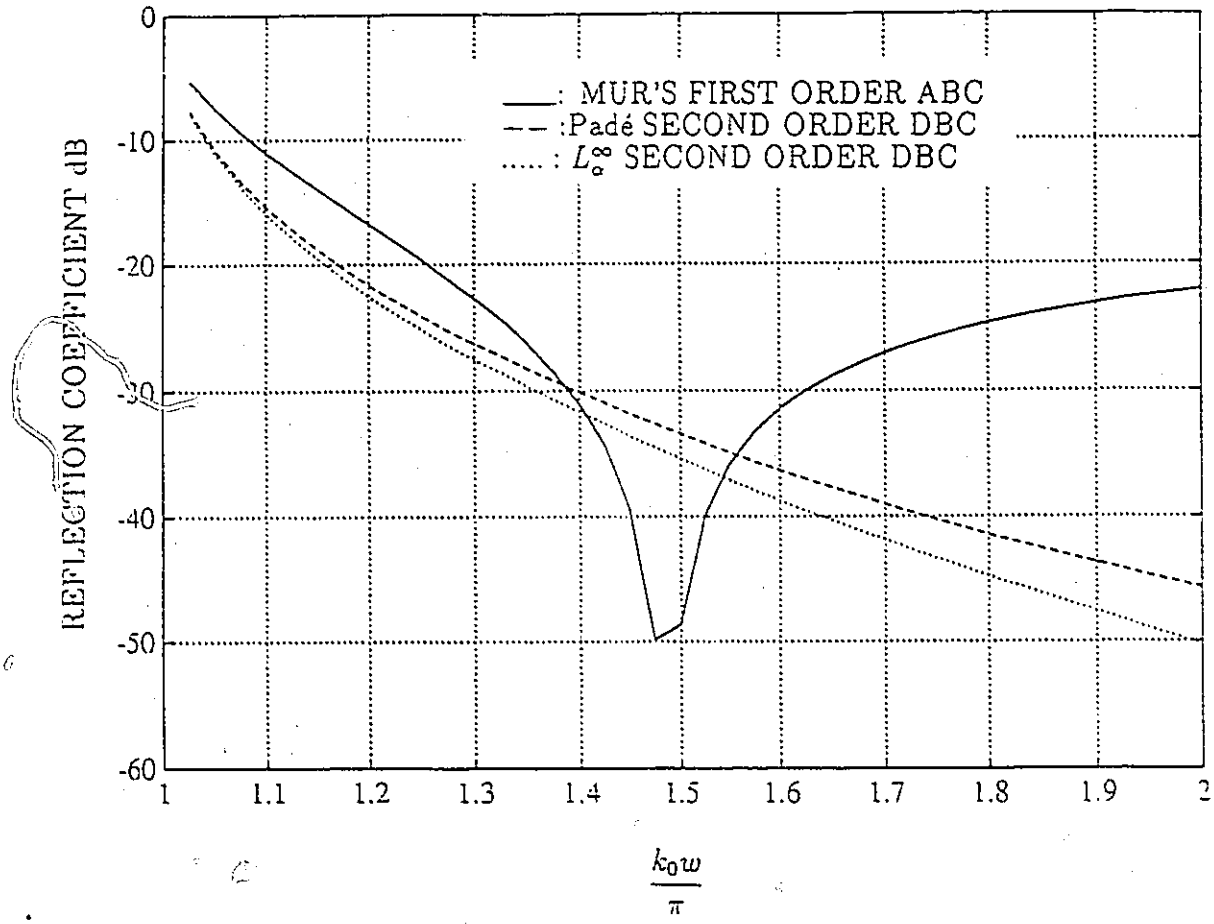

Figure 3.7: Reflection coefficients for the second order one-way DBC's

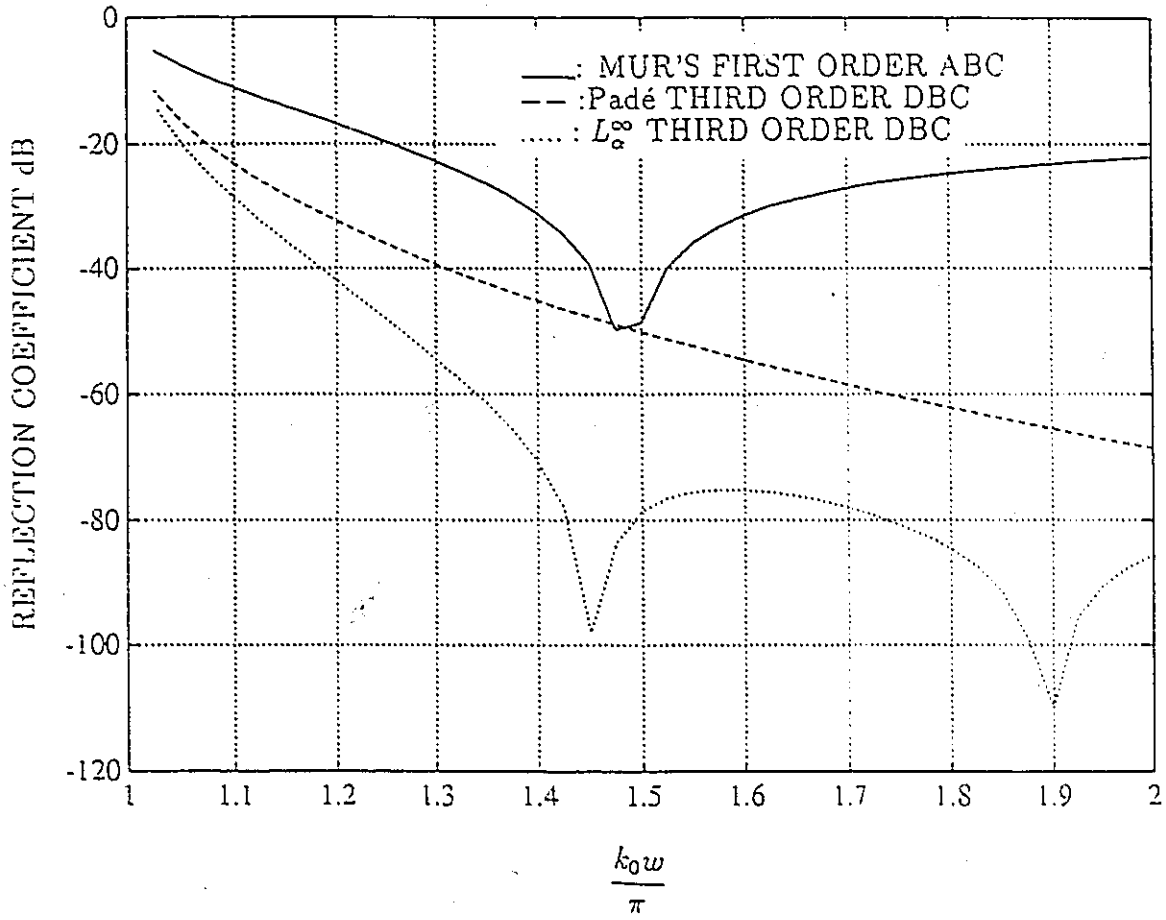

Figure 3.8: Reflection coefficients for the third order one-way DBC's

3.4 Designing DBC by Using Digital Filtering Theory

The objective of this section is to present another dispersive boundary condition (DBC), which can also absorb waves over a wide frequency band. This DBC is based on a new interpretation to the boundary condition. To start with, the relationship between the absorbing boundary condition and digital filters is discussed. Then, based on this new explanation for the DBC, we investigate the design of a DBC using digital filter theory. Finally, the relationship between our new digital filter DBC and the other DBCs is investigated in the next section.

3.4.1 The Relationship between the Boundary Condition and Digital Filter

As mentioned before, in many FD-TD analyses, the major direction of the power flow within components, such as microstrip lines, feed lines for microstrip antennas and waveguides, is in the waveguided direction due to the guiding nature of these structures. This is quite similar to the one dimensional propagation case. Based on this observation, many workers use the following one dimensional boundary condition

$$\left(\frac{\partial}{\partial z}+\frac{1}{v_i}\frac{\partial}{\partial t}\right)E=0 \tag{3.47}$$

where E represents the tangential electric field component on the boundary wall and v_i represents the velocity of propagation of the field. This equation is easily discretized using only field components on and just inside the FD-TD mesh wall, yielding the difference

equation

$$E_M^n = E_{M-1}^{n-1} + \frac{1-\rho_i}{1+\rho_i}(E_M^{n-1} - E_{M-1}^n) \tag{3.48}$$

where E_M represents the tangential electric field component on the boundary, E_{M-1} represents the tangential electric field component at the adjacent node which is inside the boundary, and $\rho_i = v_i \Delta t / \Delta z$. It will be demonstrated, using the reflection coefficient given by (3.51), that the above boundary condition can only be optimized for a wave whose frequency corresponds to the velocity, v_i, and that the magnitude of the energy reflected by the boundary can be quite large due to reflections of waves at other frequencies. The reflection coefficient R is defined as the ratio of the reflected wave field to an incident plane wave. Consider a plane wave travelling to the right. The wave has the form

$$E_{in} = e^{j(\omega n \Delta t - k i_z \Delta z)} \tag{3.49}$$

where i_z is the space position index and n is the time index. When this wave strikes an artificial boundary, it produces the total wave field

$$E_{tot} = e^{j(\omega n \Delta t - k i_z \Delta z)} + R e^{j(\omega n \Delta t + k i_z \Delta z)}, \tag{3.50}$$

where R is the reflection coefficient. Since this wave field satisfies the boundary condition, R can be determined by substituting E_{tot} into the boundary condition equation. By substituting expression (3.50) into (3.48), the reflection coefficient expression as a function of frequency is obtained for the ABC (3.48). That is

$$R_{ABC} = \frac{1 - e^{-j\omega\Delta t + jk\Delta z} - \frac{1-\rho_i}{1+\rho_i}(e^{-j\omega\Delta t} - e^{jk\Delta z})}{1 - e^{-j\omega\Delta t - jk\Delta z} - \frac{1-\rho_i}{1+\rho_i}(e^{-j\omega\Delta t} - e^{-jk\Delta z})} \tag{3.51}$$

where the propagation constant, $k = k(\omega)$, is governed by the dispersion relationship for the wave. The dispersion caused by the FD-TD algorithm is ignored because it is much smaller than the dispersion of the wave itself. For further discussion of the DBC, based on the reflection coefficient, the relationship for the dispersion of the dominant TE_{10} mode for an air-filled waveguide is used in the following analysis.

The solid lines in Fig. 3.9 show the amplitudes of reflection coefficient (3.51) for different wave velocities, where w is the width of a waveguide, which is divided into 20 space steps, and k_0 is the free space propagation constant. From this result, it can be seen that the ABC (3.48) or Mur's first order ABC has very good absorbing characteristics over only a very narrow frequency band. Our objective is to develop a dispersive boundary condition by modifying Mur's first order ABC so that it can be used to absorb waves over a wide frequency. With this in mind, let treat the ABC (3.48) as a digital system, where E_M, denoted by $y(n)$, is thought to be the output of the system, and E_{M-1} is thought to be the input of the system and is denoted by $x(n)$. Then, the ABC (3.48) can be rewritten as

$$y(n) = x(n-1) + \frac{1-\rho_i}{1+\rho_i}[y(n-1) - x(n)]. \tag{3.52}$$

Performing the z transform on (3.52), we have the following frequency domain function or frequency response of the system

$$H(\omega) = H(z)|_{z=e^{j\omega}} = \frac{e^{-j\omega} - \frac{1-\rho_i}{1+\rho_i}}{1 - \frac{1-\rho_i}{1+\rho_i}e^{-j\omega}}. \tag{3.53}$$

Analyzing the amplitude and phase responses of the above system, we can see that the absorbing boundary condition (3.48) is nothing but an allpass filter. Further, speaking from the digital filtering point of view, the function of the ABC (3.48) is to let all the frequency components pass without any magnitude weighting, but to impose different phase shifts on different frequency components as shown by the solid line in Fig. 3.10. For a dispersive boundary condition, it should also be an allpass filter, but the phase response has to be modified according to the dispersion relation for the wave. Now let us derive the optimal phase response for the dispersive boundary condition system. The boundary condition (3.48) is a non-dispersive boundary condition, which is optimized for one frequency component with phase velocity v_i. In order that waves at other frequencies are also absorbed, the velocity v_i in ABC (3.48) should be adjusted. This adjustment is equivalent to adjusting the phase shift of the system (3.53) for that frequency. So, the phase shift of the DBC system for one

given frequency can be obtained by following two procedures: (i) determine the velocity of the wave in (3.48) from the dispersion relationship of the wave at a particular frequency; (ii) use the frequency response (3.53) to calculate the phase shift that corresponds to this frequency. For the waveguide analysis, using the TE_{10} mode dispersion, the phase response of the DBC system is given in Fig. 3.10 (dotted line). At this juncture we arrive at an important conclusion, that is, the design of a dispersive boundary condition is nothing more than designing an allpass filter which has the required phase response (dotted line in Fig. 3.10).

3.4.2 Designing DBC Using Digital Filtering Techniques

An mth order allpass filter designed to approximate the desired phase response is usually in the following form

$$\begin{aligned} & y(n) + a_1 y(n-1) + a_2 y(n-2) + ... + a_m y(n-m) \\ = \; & b_0 x(n) + b_1 x(n-1) + b_2 x(n-2) + ... + b_m x(n-m). \end{aligned} \tag{3.54}$$

The corresponding dispersive boundary condition is

$$\begin{aligned} E_M^n = \; & b_0 E_{M-1}^n + b_1 E_{M-1}^{n-1} + b_2 E_{M-1}^{n-2} + ... + b_m E_{M-1}^{n-m} \\ & -(a_1 E_M^{n-1} + a_2 E_M^{n-2} + ... + a_m E_M^{n-m}). \end{aligned} \tag{3.55}$$

The reflection coefficient for the above DBC is

$$R = \frac{\sum_{p=0}^{m} a_p e^{-j\omega\Delta tp} - e^{jk\Delta z} \sum_{p=0}^{m} b_p e^{-j\omega\Delta tp}}{\sum_{p=0}^{m} a_p e^{-j\omega\Delta tp} - e^{-jk\Delta z} \sum_{p=0}^{m} b_p e^{-j\omega\Delta tp}}. \tag{3.56}$$

There are several methods that can be used to design an allpass filter whose phase response approximates the desired dotted curve in Fig. 3.10. Here, an equation error method [94, 96] is used to design the filter from the desired data. One third-order filter

which was designed using this method is given by

$$\begin{aligned} & y(n) + a_1 y(n-1) + a_2 y(n-2) + a_3 y(n-3) \\ = \; & b_0 x(n) + b_1 x(n-1) + b_2 x(n-2) + b_3 x(n-3) \end{aligned} \tag{3.57}$$

where $a_0 = 1.000$, $a_1 = -0.9675$, $a_2 = -0.1499$, $a_3 = 0.1210$, $b_0 = -0.3335$, $b_1 = 1.2101$, $b_2 = -0.5159$, $b_3 = -0.3628$. The phase response of this filter is shown in Fig. 3.10 by the dashed line. The amplitude of the reflection coefficient of the corresponding DBC is shown in Fig. 3.9 by the dashed line. From Fig. 3.9, it can be seen that ABC (3.48) can absorb waves in only a very narrow range of frequencies, whereas DBC (3.57) can absorb waves over a larger band of frequencies. The absorbing quality of the DBC can be improved by increasing the order of the DBC and by investigating other filter designing methods.

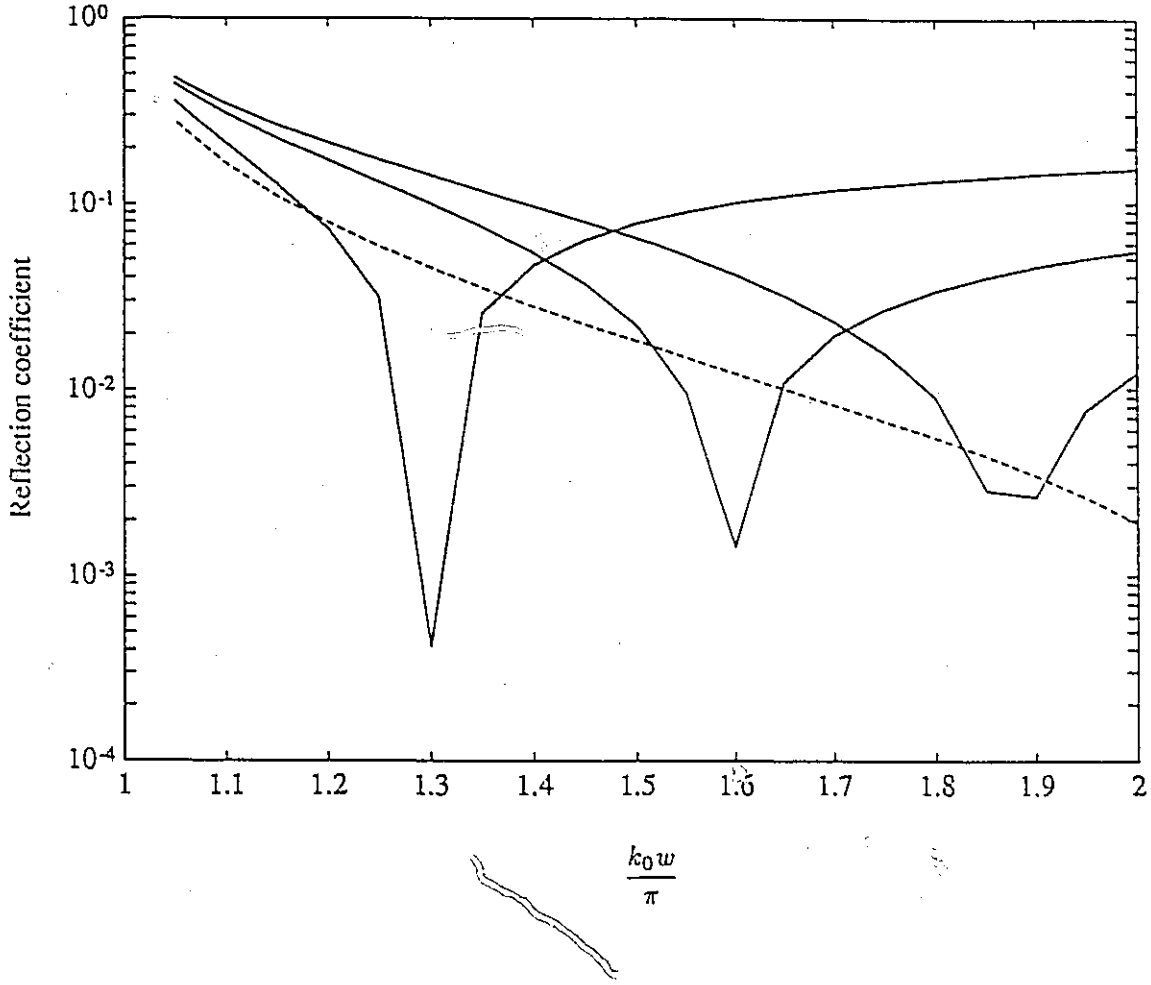

Figure 3.9: Reflection coefficients; Solid: Mur's first order ABC; Dashed: digital-filter DBC.

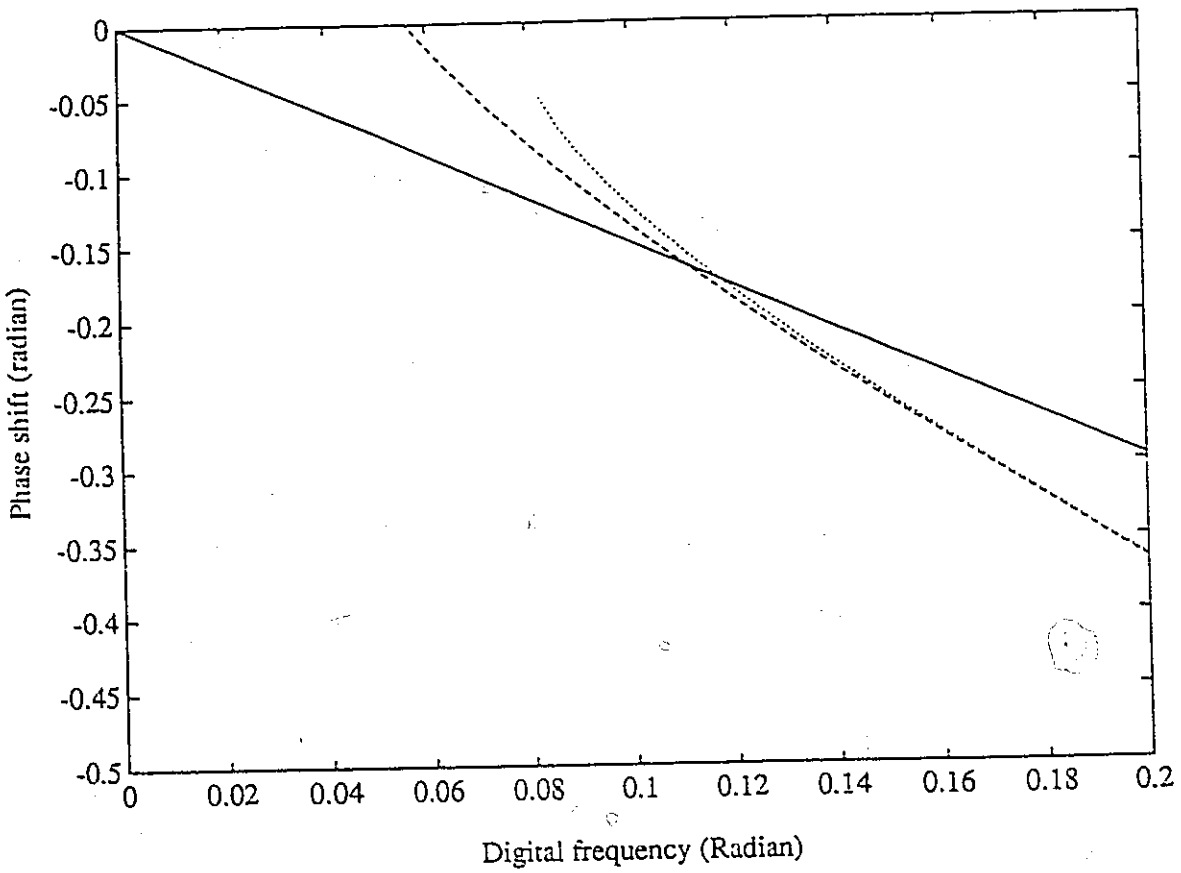

Figure 3.10: Phase response of absorbing boundary condition systems. Solid: Mur's first order ABC; Dotted: theoretical DBC; Dashed: digital-filter DBC.

3.5 The Relationship between the Digital-Filter DBC and Other DBC's

In this section, it will be demonstrated that several other dispersive boundary conditions can be interpreted and developed using the digital filter dispersive boundary condition.

It is well known that digital filters are classified into two types. One is the Finite Impulse Response (FIR) filter, the other is the Infinite Impulse Response (IIR) filter. In the above, we have used the IIR filter to design the dispersive boundary condition. The FIR filter can also be used to design the dispersive boundary condition. But, usually FIR filters have much more coefficients and delays (much higher order) than IIR filters with the same specifications (impulse frequency response). So the main reason for our choosing a recursive digital filter (IIR filter) is that IIR filters need much less computation time and memory size than FIR filters. For the FD-TD method, the saving of computation time and memory size is very important because the absorbing boundary condition is applied at every node on the boundary walls and for each time step. The number of the nodes on the boundary of the calculation domain for most practical structures is very large.

In the past few years, a dispersive boundary condition has been proposed in [39]-[41] for use with the Transmission Line Matrix (TLM) method. This boundary condition is based on a convolution of the streams of TLM impulses that are incident on the boundary with a sequence so-called numerical Green's function to obtain the time-domain reflection sequence of wide-band absorbing terminations. From the view point of the digital filter DBC, it can be seen that this numerical Green's function is nothing more than the impulse response of the dispersive boundary condition system, and that the convolution is nothing

more than the implementation of a FIR filter. So, this dispersive boundary condition can be thought of as a special case of the proposed dispersive boundary condition. In this special case, a FIR filter has been used to design the DBC. This FIR DBC is very time consuming compared with the IIR DBC because FIR DBC involves a convolution of two very long sequences.

The time domain data from the FD-TD method is an over sampled signal (Chapter 4). Further the TE_{10} mode band is very narrow and is located in the very low part of the frequency spectrum. These properties of the time domain method require that the unit impulse response of the FIR DBC system has to be very long in order to accurately describe the non-linear phase response of the allpass filter in the corresponding TE_{10} mode band. In paper [39]-[41], the length of the numerical Green's function is about 2000. Implementing convolution with such a long sequence at each time step, and at each node on the boundary wall is very time consuming so that this DBC is not efficient. However, there is one important advantage with the FIR DBC, which is that it is always stable because of the characteristics of FIR filter.

Another dispersive boundary condition is the One-Way DBC, which was originally presented in [66] and which has been systematically developed in Section 3.3. This DBC can also be interpreted using the digital filter DBC. From (3.42) and (3.44), it can be seen that the second and the third order one-way DBCs involve only first order derivatives along the z direction. So, they can be discretized using only field components which lie on the boundary and the first node inside the FD-TD mesh wall. Then they can then be written in the standard IIR DBC form (3.54). Once they are written in a standard form, their stability can be studied using the stability theory developed in the digital filter and control theory. This is one benefit we bring to the DBC by using digital filter theory. On the other hand, the benifit that we can bring to digital filter theory by studying DBCs is that digital filters might be designed using the wave equation. This point can be explained

in the following.

It should be noted that although we have designed an IIR DBC using digital filter design techniques, the performance of the DBC is not good enough, i.e. the designed phase frequency response does not approximate the required phase response accurately. But, if we design the IIR DBC using the one-way DBC technique, we can get a desired phase frequency response more accurately. This result might bring a new approach to designing digital filters. This example demonstrates the importance of studying the relationship between different fields.

The DBC discussed in Sections 3.1 and 3.2 can also be interpreted using the IIR DBC. For the second order DBC, the discretized boundary condition is (3.31). Similarly, let us take this DBC as a multichannel digital system. Here E_M is thought to be the output of the system and is denoted by $y(n)$; E_{M-1} is thought to be the first input of the system and is denoted by $x_1(n)$; finally E_{M-2} is thought to be the second input of the system and is denoted by $x_2(n)$. Then the DBC (3.31) can be written as

$$\begin{aligned} y(n) &= 2x_1(n-1) - x_2(n-2) \\ &+ (\gamma_1+\gamma_2)(y(n-1) - x_1(n) - x_1(n-2) + x_2(n-1)) \\ &- \gamma_1\gamma_2(y(n-2) - 2x_1(n-1) + x_2(n)). \end{aligned} \tag{3.58}$$

Once the DBC is written in this form, its stability can be studied using the stability theory developed in digital filter and control theory. In addition, another multichannel digital filter DBC can be designed from the above model using a technique similar to that used in the last section.

3.6 Summary and Discussions

In this chapter, a theory for dispersive boundary conditions has been systematically formulated and developed. First, based on wave decomposition and using an approach which is analogous to Bayliss and Turkel's, we derived a dispersive boundary condition. This DBC has been applied to microstrip and waveguide component analyses, and the significant improvement in performance of this DBC compared with others has been demonstrated with numerical results. Then, in order to theoretically analyze the performance of DBC, and to further develop other DBCs, we have formulated reflection coefficients for DBC. Using the formulated DBC reflection coefficient, as well as approximation techniques developed in deriving one-way Absorbing Boundary Conditions, a one-way DBC was generalized and developed. Finally, by studying the relationship between digital filter and dispersive boundary conditions, we presented a Digital Filter Dispersive Boundary Condition. It has been found that three other DBCs can be interpreted using digital filter DBC. By using digital filter and control system theories we can throw further light on the properties of these three DBCs.

The main difference between DBC and ABC is that DBC is designed to optimize the boundary condition in accordance with the dispersion characteristics of the waves, whereas ABC is designed to optimize the boundary condition based on the propagation direction of the waves. Based on concepts presented in this chapter, ABC and DBC can be developed side by side.

For example, Liao's ABC [33] was presented for absorbing wave in a wide range of angles. This ABC can be modified into a DBC in the following way. In Liao's ABC, there is a constant α, which is called as the artificial transmitting coefficient, and which is usually chosen to be 1. Suppose that we know the dispersion for the wave. Then, we can optimize α by calculating the reflection coefficient of Liao's ABC. With the optimized α, Liao's ABC

can be used as a DBC.

Another example is that given in Section (3.1), where Key and Higdon's ABC has been described in terms of dispersive boundary conditions. This description gives a one dimensional interpretation of Key and Higdon's ABC. That is, the waves from different angles are first mapped into the waves traveling along the z-axis with corresponding velocities, then the waves with different velocities in one dimension are absorbed by the dispersive boundary condition. This one dimensional explanation makes it easier for us to understand Key and Higdon's ABC. Furthermore, let us consider that Liao's and Bayliss and Turkell's ABCs have been derived based on the one dimensional wave decomposition models. Then, we can classify Key and Higdon's, Liao's, and Bayliss and Turkell's ABCs as *one-dimensional ABCs*. In this way, we can simplify the analysis of these ABCs and we can study these ABCs in one dimension rather than in two or three dimensions. Several authors have mentioned the advantage of these ABCs, which is their easy implementation even at the corners of the computation domain. This classification will tell us why, because all of them are one dimensional ABC and they have been applied to absorb the waves in multi-dimensions.

Chapter 4

USE OF DIGITAL SIGNAL PROCESSING FOR FAST FD-TD ANALYSIS OF RESONATORS

In this chapter we discuss the use of digital filtering and spectrum estimation techniques for improving the efficiency of the FD-TD algorithm in solving eigenvalue problems. The great improvement achieved in the efficiency of the method is demonstrated by means of both numerical and measurement results. In addition, several improvements to the present FD-TD method for eigenvalue analysis are presented. These include the analysis of open dielectric resonators and the extraction of the resonant frequencies from the FD-TD results. The result for the open dielectric resonator analysis is validated by using measured data.

4.1 Introduction

The optimization of the performance of resonators in microwave circuits requires accurate and efficient methods for calculating the resonant frequencies and the spatial distributions

of the fields. Various methods have been developed to study the resonant frequencies of resonant structures. Most of them, such as; the mode matching method, integral equation method, and finite element method, are carried out in the frequency domain [90].

The finite-difference time-domain (FD-TD) method has been widely used for solving electromagnetic problems. Resently, it has been used to solve eigenvalue problems associated with resonator structures [91, 92] and to calculate critical parameters for complex microstrip antennas [72, 79]. All of these results have shown the FD-TD method to be a very powerful tool for eigenvalue analysis, primarily because of two desirable attributes. First, it can be applied to problems exhibiting a complex structure which may be very difficult to solve using other analytical or numerical methods. Second, only one computation is required to get the frequency domain results over a large frequency spectrum. However, this method has one significant drawback, which is that it requires a very long computation time for extracting the resonant frequencies from the FD-TD results; for example, in the case of the problem discussed in [91], the time iteration N has to be as large as $N = 2^{16}$.

The main purpose of this chapter is to introduce the use of digital filtering and modern spectrum estimation techniques with the FD-TD method, as a means for overcoming the above limitation. By using numerical results, it will be shown that modern spectrum estimation techniques can reduce the time taken to solve a problem, such as that discussed by [91], by one order of magnitude, without any loss of accuracy in calculating the resonant frequencies. It follows from this example, that, in general, the FD-TD computational time for these types of problems can be reduced by one order of magnitude. In addition, several other improvements to the method used in [91] are presented. These include the ability to analyze open dielectric resonators, the technique for extracting the resonator frequencies, as well as the calculation of the field distribution, based on the FD-TD results.

4.2 FD-TD Method for Resonator Analysis

For ease of description, the method is described by referring to the generalized cylindrical shaped dielectric resonator (DR) in Fig. 4.1. This structure is rotationally symmetric. Since $TE_{01\delta}$ modes are the most commonly used for DR applications, only the TE_0 modes are discussed. The relevant form of Maxwell's equations is

$$\frac{\partial}{\partial t}(\epsilon E_\theta) = \frac{\partial H_r}{\partial z} - \frac{\partial H_z}{\partial r} \tag{4.1}$$

$$\frac{\partial}{\partial t}(\mu H_r) = \frac{\partial E_\theta}{\partial z} \tag{4.2}$$

$$\frac{\partial}{\partial t}(\mu H_z) = -\frac{1}{r}\frac{\partial (rE_\theta)}{\partial r} \tag{4.3}$$

Using a central difference scheme similar to that used by Yee [1], the above equations can be discretized as:

$$\begin{aligned} E_\theta^{n+\frac{1}{2}}(i,j) &= E_\theta^{n-\frac{1}{2}}(i,j) + \frac{\Delta t}{\Delta z \epsilon}[H_r^n(i,j+\frac{1}{2}) - H_r^n(i,j-\frac{1}{2})] \\ &- \frac{\Delta t}{\Delta r \epsilon}[H_z^n(i+\frac{1}{2},j) - H_z^n(i-\frac{1}{2},j)] \end{aligned} \tag{4.4}$$

$$H_r^{n+1}(i,j-\frac{1}{2}) = H_r^n(i,j-\frac{1}{2}) + \frac{\Delta t}{\mu \Delta z}[E_\theta^{n+\frac{1}{2}}(i,j) - E_\theta^{n+\frac{1}{2}}(i,j-1)] \tag{4.5}$$

$$H_z^{n+1}(i+\frac{1}{2},j) = H_z^n(i+\frac{1}{2},j) - \frac{\Delta t}{\mu \Delta r r_{i+\frac{1}{2}}}[r_{i+1}E_\theta^{n+\frac{1}{2}}(i+1,j) - r_i E_\theta^{n+\frac{1}{2}}(i,j)] \tag{4.6}$$

where i and j are space indices and n is time index.

The computation domain diagram is shown in Fig. 4.2. The tangential electric field components are located at the interfaces between different materials and on the outer boundaries of the computation domain. The fields at the interfaces between different materials can still be calculated using (4.4), if it is remembered that average of the two dielectric constants, $(\epsilon_1+\epsilon_2)/2$, has to be used in place of ϵ in the equation. Using a derivation similar to that used in [52], it can be proved that, for the fields at an interface between three media,

the effective dielectric constant becomes $(\epsilon_1 + \epsilon_2 + \epsilon_3)/3$, and for four media, it becomes $(\epsilon_1 + \epsilon_2 + \epsilon_3 + \epsilon_4)/4$.

Previous analyses, such as given in [91, 92], are limited to a consideration of a closed resonator, where the tangential electrical fields on the outer boundaries are forced to be zero. Actually, by using the well developed absorbing boundary condition (ABC) in conjunction with the FD-TD method [17], the method can be extended so that it can deal with the open structure problem. In this study, Mur's first-order boundary condition [22] is used:

$$\left(\frac{\partial}{\partial z} + \frac{1}{v_p}\frac{\partial}{\partial t}\right) E = 0 \tag{4.7}$$

where E represents the tangential electric field component relative to the boundary wall and v_p represents the phase velocity of the field. One way to impose (4.7) to second-order accuracy is to discretize (4.7) at $z = (M - \frac{1}{2})\Delta z$. At $z = (M - \frac{1}{2})\Delta z$ and $t = (n + \frac{1}{2})\Delta t$,

$$\frac{\partial}{\partial z} E(z,t)|_{z=(M-\frac{1}{2})\Delta z} \approx \frac{1}{\Delta z}(E_M^{n+\frac{1}{2}} - E_{M-1}^{n+\frac{1}{2}}), \tag{4.8}$$

$$\frac{1}{c}\frac{\partial}{\partial t} E(z,t)|_{t=(n+\frac{1}{2})\Delta t} \approx \frac{1}{c\Delta t}(E_{M-\frac{1}{2}}^{n+1} - E_{M-\frac{1}{2}}^{n}). \tag{4.9}$$

In this manner, the finite difference approximation is accurate to the second order. But since the values at the half grid points and half time steps are not available for E fields, it is expedient to approximate

$$E_m^{n+\frac{1}{2}} \approx \frac{1}{2}(E_m^{n+1} + E_m^n), \tag{4.10}$$

$$E_{m+\frac{1}{2}}^{n} \approx \frac{1}{2}(E_{m+1}^{n} + E_m^n). \tag{4.11}$$

The above approximations are also second-order accurate if $E(z,t)$ is a smooth function. Consequently, using (4.8)-(4.11) in (4.7), one obtains

$$E_M^n = E_{M-1}^{n-1} + \frac{\Delta z - v_p \Delta t}{\Delta z + v_p \Delta t}(E_M^{n-1} - E_{M-1}^n) \tag{4.12}$$

where E_M represents the tangential electric field component on the boundary and E_{M-1} represents the tangential electric field component a distance of one node inside the boundary.

The other absorbing boundary conditions [17] can be applied to improve the accuracy. But, according to our experience, the first order ABC has sufficient accuracy to deal with high dielectric constant resonators.

To start the computation, the initial electric and magnetic fields are set to zero throughout the grid, except at one selected point. Here the electric field is set to 1. This unit impulse source will excite a large number of modes. Using the above algorithm, Fig. 4.3a gives the computed electric field in the time domain at the point of observation. The resonant frequencies can be obtained by taking the Fourier transform of the computed time domain response. The field distribution for any particular frequency can be obtained by performing a Fourier transform at each point in the computation domain at that frequency. With the objective of getting more accurate estimates of the resonant frequency and field distribution than that have been obtained in the past, the following procedure is put forward.

The procedure to be followed is based on the signal analysis of the FD-TD time domain results. In this section, it is assumed that the sequence length of the FD-TD data sequence $\{x(n)\}$ is very long, where $x(n)$ is one of the field components. If one follows common practice in FD-TD analysis, the fast Fourier Transform (FFT) algorithm is used to calculate the discrete Fourier transform (DFT) of $\{x(n)\}$ to get the spectrum, $X(f)$, of $x(t)$, where $x(n) = x(t)|_{t=n\Delta t}$ and Δt is the time step used in the FD-TD algorithm. For some applications, this method is deficient, both in terms of its efficiency and its accuracy. The reason for this is that the $N/2$ values of DFT are uniformly distributed over a very large frequency bandwidth, extending from 0 to $f_s/2$ Hz, where $f_s = 1/\Delta t$ is the sampling frequency, and because the frequency resolution, which is given by

$$\Delta f = \frac{1}{N \cdot \Delta t} \quad , \tag{4.13}$$

where N is the length of the sequence $\{x(n)\}$, is too coarse to accurately determine resonant frequencies. In practice, only the lower part of the band is of interest. One method that has

been suggested here is to do the numerical integration of Fourier Transform of $x(t)$ directly in the interested frequency band

$$\begin{aligned} X(f) &= \int_0^{\infty} x(t)\exp(-j2\pi ft)\mathrm{d}t \\ &\approx \int_0^{N\Delta t} x(t)\exp(-j2\pi ft)\mathrm{d}t \\ &\approx \sum_{n=0}^{N-1} x(n)\exp(-j2\pi fn\Delta t)\Delta t. \end{aligned} \tag{4.14}$$

The advantage of this method is that it removes ambiguities sometimes encountered with the discrete Fourier Transform, due to narrowband signal components with center frequencies that lie in the gaps between the $N/2$ frequency points evaluated with the DFT. It will be shown in the following that, when FD-TD method is used for resonator analysis, the time domain results are signals which consist of many narrowband signal components. The accuracy of calculating the spectral peaks, i.e. the field distribution, is also enhanced by using (4.14).

The efficiency for evaluating (4.14) can be greatly improved by using the following method. Instead of using the original sequence $\{x(n)\}$ directly from the FD-TD analysis, a new sequence $\{x_1(n)\}$ is used in (4.14), which is obtained by decimating the $\{x(n)\}$ at a certain rate. The desampling rate is determined by the ratio of one-half the sampling frequency $f_s/2$ to the maximum frequency f_{max} of the long sequence $\{x(n)\}$. Because $\{x_1(n)\}$ is much shorter than the original sequence $\{x(n)\}$, the time required to analyze the new time domain sequence can be greatly reduced, with no reduction in the accuracy of the result. The theory which supports this treatment is Nyquist sampling theorem [93].

In order to illustrate the method clearly, let us refer to the dielectric resonator problem given in Fig. 4.1. In Fig. 4.3a is given the time domain results for the observation point shown in Fig. 4.2. This result was obtained directly from the FD-TD analysis. The DFT spectrum corresponding to this result is given in Fig. 4.3b. The parameters used in the calculation are

Dimension: $D = 6.26$ mm, $L = 4.22$ mm.

$L_1/L = 0.943$ mm, $L_2/L = 0.166$ mm

$\epsilon_{r1} = 36.2$. $\epsilon_{r2} = 9.5$

Mesh dimensions in dielectric region: $24\Delta z \times 18\Delta r$

$\Delta z = 0.17583$ mm, $\Delta r = 0.175824$ mm

$\Delta t = .65(\Delta z + \Delta r)/(2c)$, c is the speed of light in free space

According to the Nyquist theorem and from the spectrum in Fig. 4.3b, it follows that the original sequence $\{x(n)\}$ is a much over-sampled time domain signal, and that a new sequence $\{x_1(n)\}$ can be obtained by using a desampling rate of about 10. In Fig. 4.3c, the solid line gives the result obtained by applying (4.14) to the long sequence, and the dashed line gives the result obtained by applying (4.14) to the decimated sequence $\{x_1(n)\}$. The two results are exactly the same and therefore the dashed line is obscured by the solid line in Fig. 4.3c.

After getting the much shorter sequence $\{x_1(n)\}$, the numerical integration of (4.14) can also be calculated using a FFT program in the following manner. First, pad zero values to the decimated sequence $\{x_1(n)\}$, then apply FFT to the padded sequence. The number of padded zeros is determined by the required frequency resolution.

Another phenomenon that needs some explanation is why the FD-TD results, $\{x(n)\}$, which can be thought as a unit impulse response of the system under test, only contain components at the lower end of the frequency spectrum. The answer lies in the dispersion that is introduced to the results by the FD-TD algorithm itself [45]. Another simpler explanation to this phenomena is that the wavelength of the waves which can freely propagate on the FD-TD grid should be at least two grid spaces. Otherwise, the grids are too coarse to describe (support) wave movement, thereby preventing waves from propagating on the FD-TD grid. The corresponding cutoff frequency is the maximum frequency of the FD-TD

time domain result, which is equal to about $f_{max} = v/(2\Delta h)$, where v is the speed of light in the dielectric materials and Δh is the grid size (where a uniform grid is assumed). For dielectric resonator analysis, since most of the energy is centred in the material which has the largest dielectric constant, the velocity $v = c/\sqrt{\epsilon_{max}}$ should be used to determine the maximum frequency of the time domain result of FD-TD method, where c is the velocity of light in free space. Once the maximum frequency f_{max} is known, the desampling rate is easily derived.

4.3 Use of Digital Filtering and Modern Spectrum Estimation Techniques with the FD-TD Method

The objective of this section is to use digital filtering and modern spectrum estimation techniques to extract the resonant frequencies of a dielectric resonator from a short sample of FD-TD data, given by $\{x_2(n)\}$. Suppose $\{x_2(n)\}$ consists of the first two thousand data points in $\{x(n)\}$. The DFT spectrum of $\{x_2(n)\}$ is shown in Fig. 4.4a. After desampling $\{x_2(n)\}$, using a desampling rate of $(f_s/2)/f_{max}$, which is about 10, we get a sequence $\{x_3(n)\}$ whose DFT spectrum is shown in Fig. 4.4b. Because we are interested in the lower frequency band, we further process the signal $\{x_3(n)\}$ by using a decimating filter to get $\{x_4(n)\}$, whose DFT spectrum is shown in Fig. 4.4c. When applying the decimating filter [95], we first pass the data through a low-pass digital filter, then, according to the maximum frequency of the filtered output, we desample the filtered output to get the final output signal. In order to improve the accuracy of estimating the resonant frequencies of the first few modes, we further process $\{x_4(n)\}$ with a low-pass filter and get $\{y(n)\}$, whose DFT spectrum is shown in Fig. 4.4d. In all cases, ninth order Butterworth filters are used to carry out the filtering. In the filtering process, the data are filtered in both the forward and backward directions, thereby eliminating all phase distortion and minimizing

filter startup transients [96]. In the next phase of the work we carry out a search for a good high resolution spectrum estimator, with which to extract the resonant frequencies from the data set $\{y(n)\}$.

From the behavior of the spectrum of $\{x(n)\}$, based on the results given in Fig. 4.3c. it seems reasonable to assume that $\{y(n)\}$ is composed of sinusoidal components. One of the best methods for estimating the frequencies of sinusoidal components is the multiple signal classification (MUSIC) method [97]-[99]. This method belongs to the eigendecomposition-based class of super-resolution spectrum estimation methods. The term "super-resolution" refers to the fact that this class of methods have the ability to surpass the limiting behavior of classical Fourier-based methods. There are a number of reasons for our choosing the MUSIC algorithm from amongst this class of methods. These are: (i) it is easy to implement, (ii) it provides good performance, (iii) it is used as a benchmark in the field of signal processing, and (iv) it provides a good introduction to modern spectrum estimation.

The general aim of eigendecomposition-based methods is to exploit the eigenvalue decomposition of the correlation matrix of a signal consisting of p uncorrelated complex sinusoids and additive complex white noise. The signal is:

$$y(n) = \sum_{i=1}^{p} A_i \exp(j2\pi f_i n\Delta t + \theta_i) + w(n) \tag{4.15}$$

where the amplitudes $\{A_i\}$ are real-valued positive constants, the initial phases $\{\theta_i\}$ are independent random variables distributed uniformly on $[0, 2\pi]$, and the frequencies $\{f_i\}$ are distinct, Δt is the sample interval of the signal $\{y(n)\}$, and $\{w(n)\}$ is complex white noise with zero mean and variance σ^2. Although here we discuss frequency estimation for p complex sinusoids in complex white noise, the same methods generally apply to real sinusoids in real white noise if p is chosen to be twice the number of real sinusoids. The autocorrelation function of the above signal is

$$r(k) = E[y(n)y^*(n-k)]$$

$$= \sum_{i=1}^{p} A_i^2 \exp(j2\pi f_i k\Delta t) + \sigma^2\delta(k) \tag{4.16}$$

where E denotes the expectation operator and * denotes complex conjugate. The corresponding $(M+1)\times(M+1)$ ensemble-averaged autocorrelation matrix

$$\mathbf{R} = \begin{bmatrix} r(0) & r(1) & \dots & r(M) \\ r(-1) & r(0) & \dots & r(M-1) \\ . & . & \dots & . \\ . & . & \dots & . \\ . & . & \dots & . \\ r(-M) & r(-M+1) & \dots & r(0) \end{bmatrix} \tag{4.17}$$

for $M > p$ is

$$\mathbf{R} = \mathbf{S}\mathbf{D}\mathbf{S}^H + \sigma^2\mathbf{I} \tag{4.18}$$

where I is the $(M+1)\times(M+1)$ identity matrix, the rectangular matrix S is the $(M+1)\times p$ sinusoidal signal matrix defined as

$$\begin{aligned} \mathbf{S} &= [\mathbf{s}_1, \mathbf{s}_2, \dots \mathbf{s}_p] \\ &= \begin{bmatrix} 1 & 1 & \dots & 1 \\ \exp(-j2\pi f_1\Delta t) & \exp(-j2\pi f_2\Delta t) & \dots & \exp(-j2\pi f_p\Delta t) \\ \exp(-j2\pi f_1 2\Delta t) & \exp(-j2\pi f_2 2\Delta t) & \dots & \exp(-j2\pi f_p 2\Delta t) \\ . & . & \dots & . \\ . & . & \dots & . \\ . & . & \dots & . \\ \exp(-j2\pi f_1 M\Delta t) & \exp(-j2\pi f_2 M\Delta t) & \dots & \exp(-j2\pi f_p M\Delta t) \end{bmatrix}, \end{aligned} \tag{4.19}$$

D is the $p\times p$ correlation matrix of the sinusoids, and ^{H} denotes conjugate transpose. Note that the lth column of the matrix S, namely $\mathbf{s}_l$ is a signal vector of dimension $(M+1)$ carrying the frequency information of the lth complex sinusoid. Let $\lambda_1 \geq \lambda_2 \dots \geq \lambda_{M+1}$ denote the eigenvalues of the correlation matrix R, and $\nu_1 \geq \nu_2 \dots \geq \nu_{M+1}$ denote the

eigenvalues of $\mathbf{SDS}^H$, respectively. Since S is a full rank matrix and D is positive definite, it follows [100] that

$$\lambda_i = \begin{cases} \nu_i + \sigma^2, & i = 1, ..., p \\ \sigma^2, & i = p+1, ..., M+1 \end{cases} \tag{4.20}$$

Let $\mathbf{v}_1, \mathbf{v}_2, ..., \mathbf{v}_{M+1}$ denote the eigenvectors of the correlation matrix R. All the $(M+1-p)$ eigenvectors associated with the smallest eigenvlalues of R satisfy the relation

$$\mathbf{R}\mathbf{v}_i = \sigma^2 \mathbf{v}_i, \quad i = p+1, ..., M+1 \tag{4.21}$$

or, equivalently,

$$(\mathbf{R} - \sigma^2 \mathbf{I})\mathbf{v}_i = \mathbf{0}, \quad i = p+1, ..., M+1 \tag{4.22}$$

Using (4.18), the above equation can be rewritten as

$$\mathbf{SDS}^H \mathbf{v}_i = \mathbf{0}, \quad i = p+1, ..., M+1 \tag{4.23}$$

It readily follows that

$$\mathbf{S}^H \mathbf{v}_i = \mathbf{0}, \quad i = p+1, ..., M+1 \tag{4.24}$$

or more explicitly

$$\mathbf{s}_l^H \mathbf{v}_i = 0, \quad \begin{matrix} i = p+1, ..., M+1 \\ l = 1, 2, ..., p \end{matrix} \tag{4.25}$$

where the vector $\mathbf{s}_l$ constitutes the lth column of matrix S.

A fundamental property of the eigenvectors of a correlation matrix is that they are orthogonal to each other. Hence, the eigenvectors $\mathbf{v}_1, ...\mathbf{v}_p$ span a subspace that is the orthogonal complement of the space spanned by the eigenvectors $\mathbf{v}_{p+1}, ..., \mathbf{v}_{M+1}$. Accordingly, it follows from (4.25) that

$$\text{span}\{\mathbf{s}_1, ..., \mathbf{s}_p\} = \text{span}\{\mathbf{v}_1, ...\mathbf{v}_p\} \tag{4.26}$$

The $\text{span}\{\mathbf{s}_1, ..., \mathbf{s}_p\}$ refers to a subspace that is defined by the set of all linear combinations of the vectors $\mathbf{s}_1, ..., \mathbf{s}_p$. The $\text{span}\{\mathbf{v}_1, ..., \mathbf{v}_p\}$ is similarly defined.

Based on the above discussion, we can conclude the following important property of the eigenvalue decomposition of the $(M+1)\times(M+1)$ correlation matrix R of the signal defined in (4.15), which is

> The space spanned by the eigenvectors of R consists of two disjoint subspaces. One called the signal subspace, is spanned by the eigenvectors associated with the p largest eigenvalues of R. The second subspace called the noise subspace, is spanned by the eigenvectors associated with the $(M+1-p)$ smallest eigenvalues of R. These two subspace are the orthogonal complement of each other and they satisfy (4.25) and (4.26).

Various eigendecomposition-based methods exploit the above property, i.e. the existence of two subspaces, in different ways. The approach used in the MUSIC algorithm is to estimate the frequencies of the complex sinusoids by searching for those sinusoidal signal vectors $\mathbf{s}_l$ that are orthogonal to the noise subspace. This follows from (4.25).

In practice, the implementation of all of these different methods use the sample estimation of the ensemble-averaged correlation matrix R. One of the best estimations for R [98] is

$$\hat{\mathbf{R}} = \frac{1}{2(K-M)}\Phi \tag{4.27}$$

where K is the sequence length of $\{y(n)\}$ and Φ is

$$\Phi = \mathbf{A}^H\mathbf{A} \tag{4.28}$$

where $\mathbf{A}^H$ is defined as

$$\mathbf{A}^H = \begin{bmatrix} y(M) & \dots & y(K-1) & y^*(0) & \dots & y^*(K-M+1) \\ y(M-1) & \dots & y(K-2) & y^*(1) & \dots & y^*(K-M+2) \\ . & \dots & . & . & \dots & . \\ . & \dots & . & . & \dots & . \\ . & \dots & . & . & \dots & . \\ y(0) & \dots & y(K-M+1) & y^*(M) & \dots & y^*(K-1) \end{bmatrix}. \tag{4.29}$$

Let $\hat{\mathbf{v}}_1, \hat{\mathbf{v}}_2, ..., \hat{\mathbf{v}}^{M+1}$ denote the eigenvectors of the estimate $\hat{\mathbf{R}}$. Owing to the presence of uncertainties in the eigenvector estimates, $\hat{\mathbf{v}}_1, \hat{\mathbf{v}}_2, ..., \hat{\mathbf{v}}^{M+1}$, arising from the limited number of samples that are available in practice for deriving the estimate, $\hat{\mathbf{R}}$, the orthogonality relations of (4.25) no longer strictly hold. Accordingly, the MUSIC algorithm bases its estimates of the frequencies of the complex sinusoids in the data vector on locating the peaks in the expression

$$\hat{Y}_{MUSIC}(f) = \frac{1}{\sum_{i=p+1}^{M+1} |\mathbf{s}^H \hat{\mathbf{v}}_i|^2} \tag{4.30}$$

where the frequency scanning vector $\mathbf{s}(f)$ is defined by

$$\mathbf{s}(f) = [1, \exp(-j2\pi f \Delta t), ..., \exp(-j2\pi f M \Delta t)]^T \tag{4.31}$$

where ^{T} denotes transpose. It should be pointed out that MUSIC spectrum $\hat{Y}_{MUSIC}(f)$ is not a true power spectrum since it does not preserve the power of the signal nor can the autocorrelation sequence be recovered by Fourier Transforming the frequency estimator.

The MUSIC algorithm can be summarized below

1. Set up data matrix A using (4.29) and calculate the estimate $\hat{\mathbf{R}}$ of the $(M+1)\times(M+1)$ correlation matrix using (4.27). Computer the eigenvalues and eigenvectors of $\hat{\mathbf{R}}$.

2. Given that there are p complex sinusoids in the input signal, with $p \leq M$, classify the eigenvalues into two groups: One consisting of the p largest eigenvalues and the other

consisting of the $(M + 1 - p)$ smallest eigenvalues. The first group spans the sample signal subspace, the second group spans the sample noise subspace.

3. Use the eigenvectors associated with the second group to calculate the MUSIC spectrum (4.30). Determine the frequencies of the complex sinusoids by locating the spectral peaks of $\hat{Y}_{MUSIC}(f)$.

4. In place of procedure 3. the frequencies can also be determined by using root-MUSIC [100].

4.4 Numerical Results

An analysis of signal $\{y(n)\}$ was carried out using the MUSIC algorithm. It should be noted that this data sequency resulted from the filtering operation carried out in the last section. The result is shown in Fig. 4.5. The dashed line was obtained by applying a Fourier transform (4.14) to a very long FD-TD sequence, corresponding to 20000 time iterations in the FD-TD algorithm. The dotted curve gives the result from Fourier processing (4.14) of the first two thousand points in the former sequence. This shortened sequence corresponds to 2000 time iterations of the FD-TD algorithm. From this curve we see that for short data records, the resonant frequencies cannot be accurately estimated using the Fourier transform. Biases occur in the locations of the first and fourth resonant frequencies and the second and third resonant frequencies are missing altogether. The solid line gives the result of application of digital filtering and the MUSIC spectral estimation technique to the shorter data sequence. In the MUSIC algorithm, the data length of $\{y(n)\}$, K, was equal to 100; the order of the correlation matrix, $M+1$, was determined by the relation $M = 2K/3$. The accuracy of the method increases with increasing M [97]. However, $M + 1$ should not be larger than the number of data points. The choice for the order of the signal subspace, p, is based on the eigenvalue spectrum of $\hat{\mathbf{R}}$. For our example, p was equal to 21. When

p was changed from 21 to a higher value, we still got accurate frequency estimates. This suggests that the method is robust. Comparing the solid and dashed lines, it is seen that the same order of accuracy is obtained in the resonant frequency estimation by applying signal processing and spectral estimation to a short data set as that obtained by applying a Fourier transform to a much longer data set.

A semi-open dielectric resonator coupled to a microstrip substrate (Fig. 4.6) is also studied. The parameters used for this analysis are

Dimension: $D = 11.06$ mm, $L = 4.99$ mm,

$L_1' = 1.59$ mm, $L_2' = 3.18$ mm

$\epsilon_{r1} = 35.76, \quad \epsilon_{r2} = 2.2$

Dielectric region: $15\Delta z \times 18\Delta r$

$\Delta z = 0.33267$ mm, $\Delta r = 0.325294$ mm

$\Delta t = 0.65(\Delta z + \Delta r)/(2c)$, c is the speed of light in free space

The calculated and measurement results are given in Table I. In the calculation, the resonant frequencies are determined by the method presented in this chapter, where only 2000 time iterations are used in the FD-TD calculation. For the experimental results, the DR was mounted on a substrate, and the measurements were carried out with an HP8510B network analyzer.

4.5 Summary

There are three main results coming from the present study of the FD-TD method. Digital filtering and modern spectrum estimation techniques were successfully incorporated with the FD-TD method as a means of improving its efficiency for carrying out eigenvalue analysis. The efficiency and validity of the method are demonstrated using both numerical and measured results. Another relatively new spectrum estimation method, which

is called Thomson's multiple-window-method (MWM) [101], was also tested with FD-TD data. Equally good frequency estimates were obtained using MWM. The second main outcome of this research was the application of signal analyses to the time domain data obtained using the FD-TD algorithm. It has been shown that the FD-TD time domain signal for dielectric resonator analyses is much over sampled. The data that are retained for later processing can be greatly compressed, without degrading the accuracy of the analysis. This conclusion is valid when the FD-TD method is used to analyze microstrip components and antennas. In these latter cases, the maximum frequency of time domain result, f_{max}, which sets the desampling or compressing rate, is not determined by the cutoff frequency of the FD-TD algorithm itself, but rather by the maximum frequency of the excitation gaussian pulse. According to our experience, for the analysis of microstrip antennas and components [72, 79], the data from the FD-TD results can be compressed by at least one order of magnitude. So, based on this conclusion, both the memory requirements for the FD-TD time domain results and the time it takes for processing the data can be reduced by at least one order of magnitude. The third result that was demonstrated by this research is that good results can be obtained by using absorbing boundary conditions when applying the FD-TD to open dielectric resonators. The validity of the analysis was demonstrated by a comparison of measurements and calculated results. All of the above conclusions are applicable to other time domain methods, such as the Transmission Line Matrix method.

In conclusion, it should be mentioned that signal processing and spectrum estimation techniques can greatly improve both the capability and the efficiency of time domain methods. This point has been reinforced in this thesis and by several papers [70, 75, 83, 86, 102, 103], where the authors have to greater or lesser degree drawn on signal processing techniques to improve the performance of their numerical algorithms. More discussions on this point will be carried out in concluding Chapter.

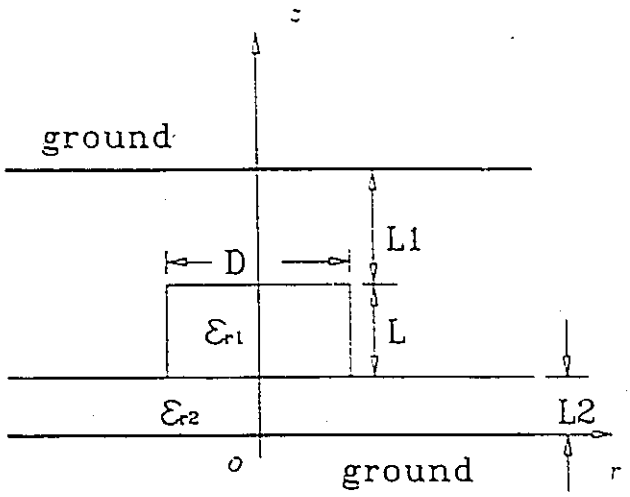

Figure 4.1: A generalized cylindrical shaped dielectric resonator

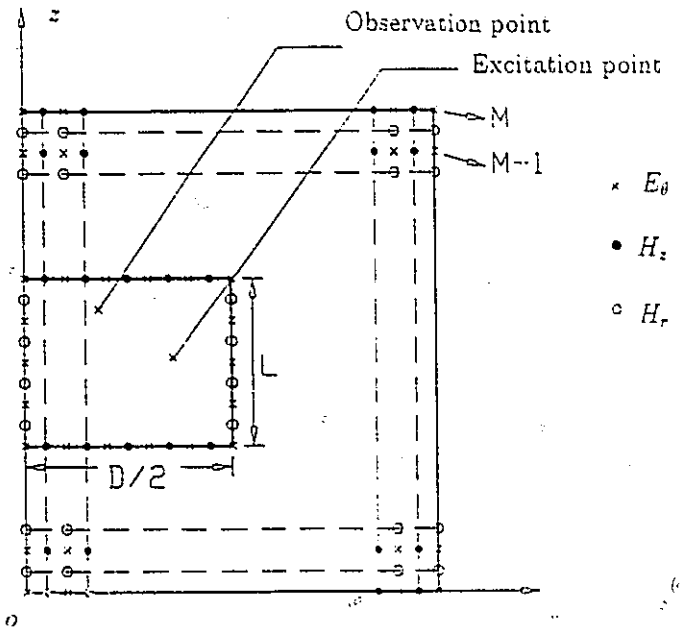

Figure 4.2: FD-TD grids, the tangential electric field components are arranged on the interface of different materials and on the outer boundaries of the computation domain.

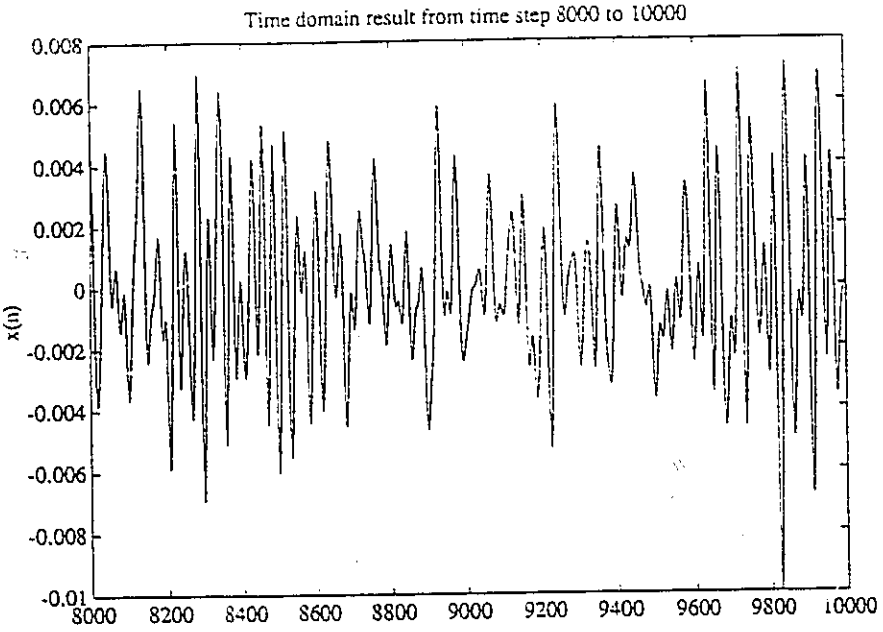
Time domain result from time step 8000 to 10000
x(n)
0.008
0.006
0.004
0.002
0
-0.002
-0.004
-0.006
-0.008
-0.01
8000
8200
8400
8600
8800
9000
9200
9400
9600
9800
10000
Time steps

(a)

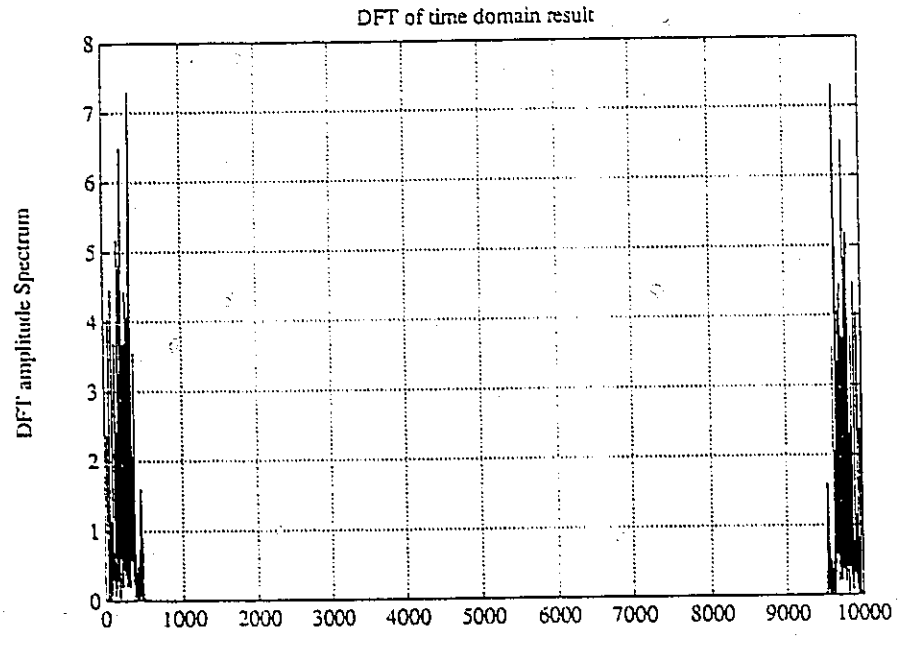
DFT of time domain result
DFT amplitude Spectrum
8
7
6
5
4
3
2
1
0
0
1000
2000
3000
4000
5000
6000
7000
8000
9000
10000
Index of DFT

(b)

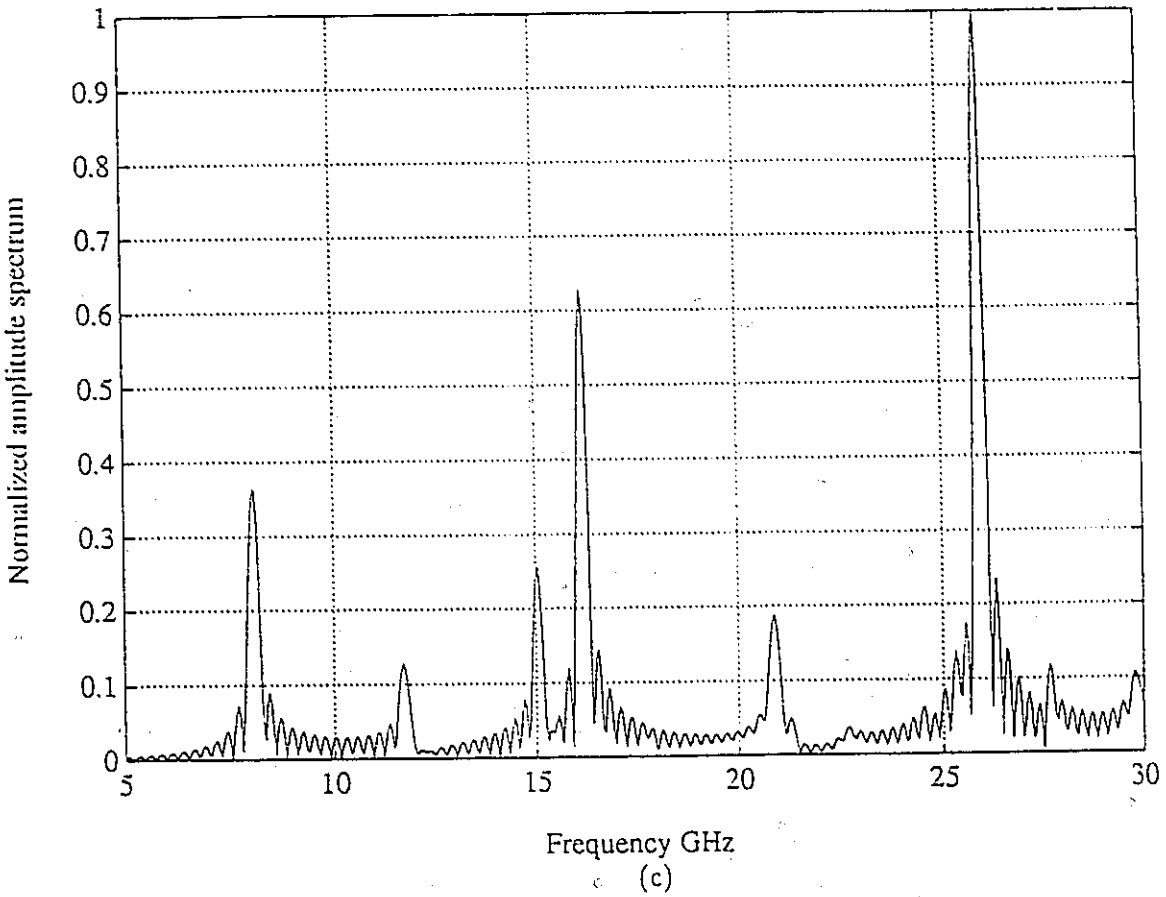

Figure 4.3: (a) Time domain result directly obtained from the FD-TD algorithm and (b) its corresponding DFT spectrum, (c) Normalized amplitude spectrum of Fourier transform of long sequence and desampled shorter sequence.

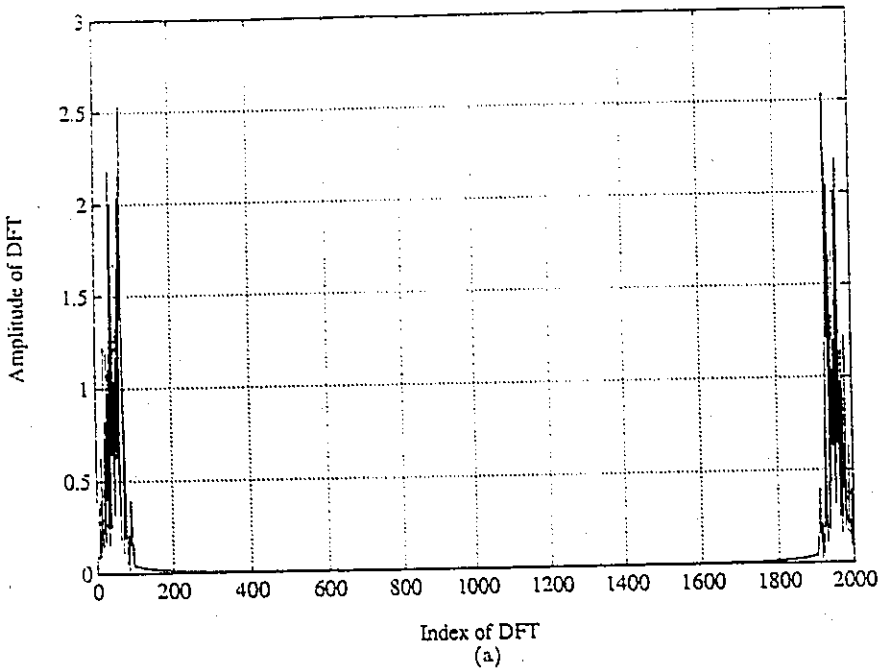
Amplitude of DFT
Index of DFT
0
0.5
1
1.5
2
2.5
3
0
200
400
600
800
1000
1200
1400
1600
1800
2000

(a)

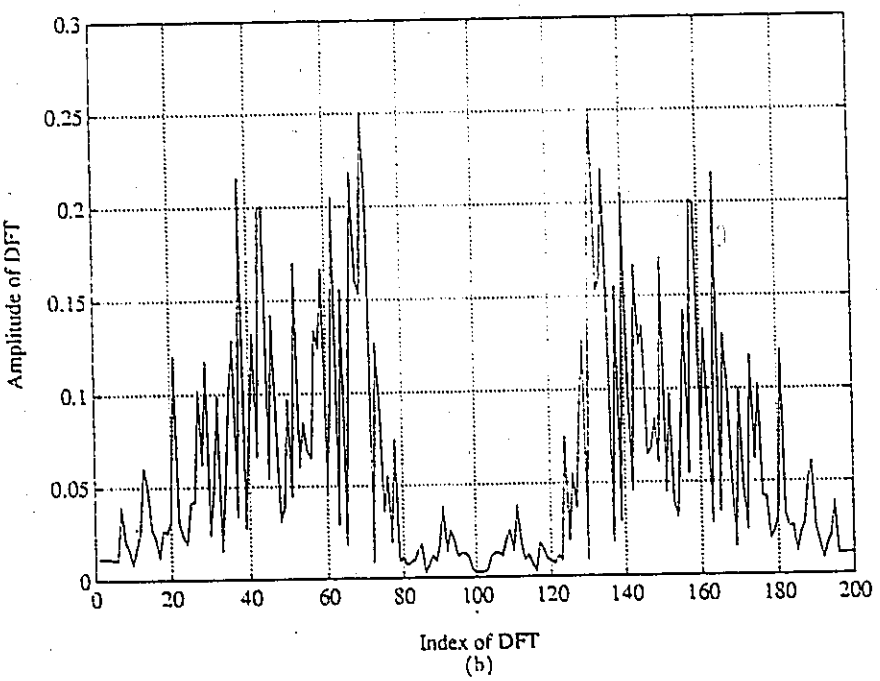
Amplitude of DFT
Index of DFT
0
0.05
0.1
0.15
0.2
0.25
0.3
0
20
40
60
80
100
120
140
160
180
200

(b)

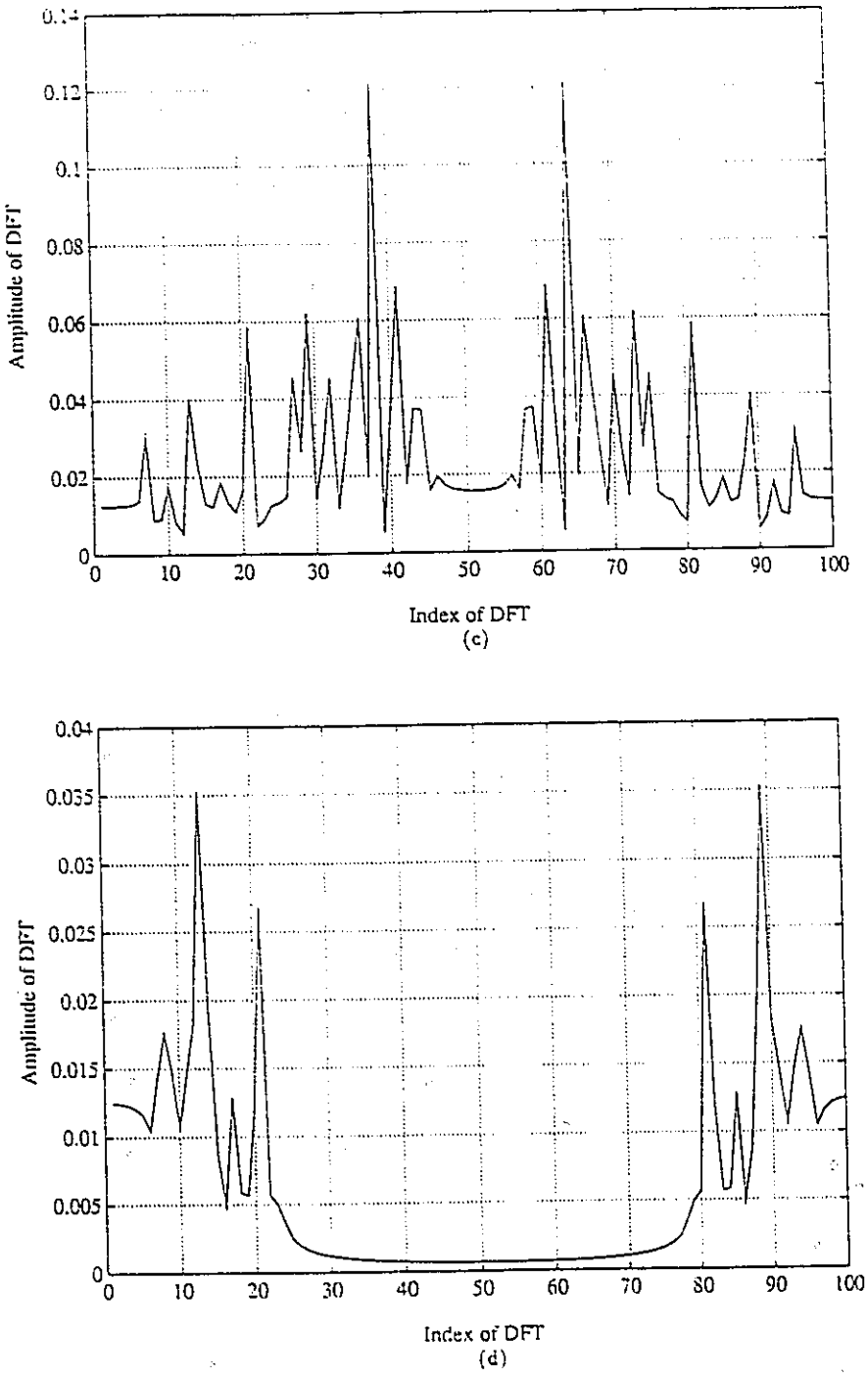

Figure 4.4: Digital filtering processing of the FD-TD time domain result. (a-d) DFT amplitude spectrum

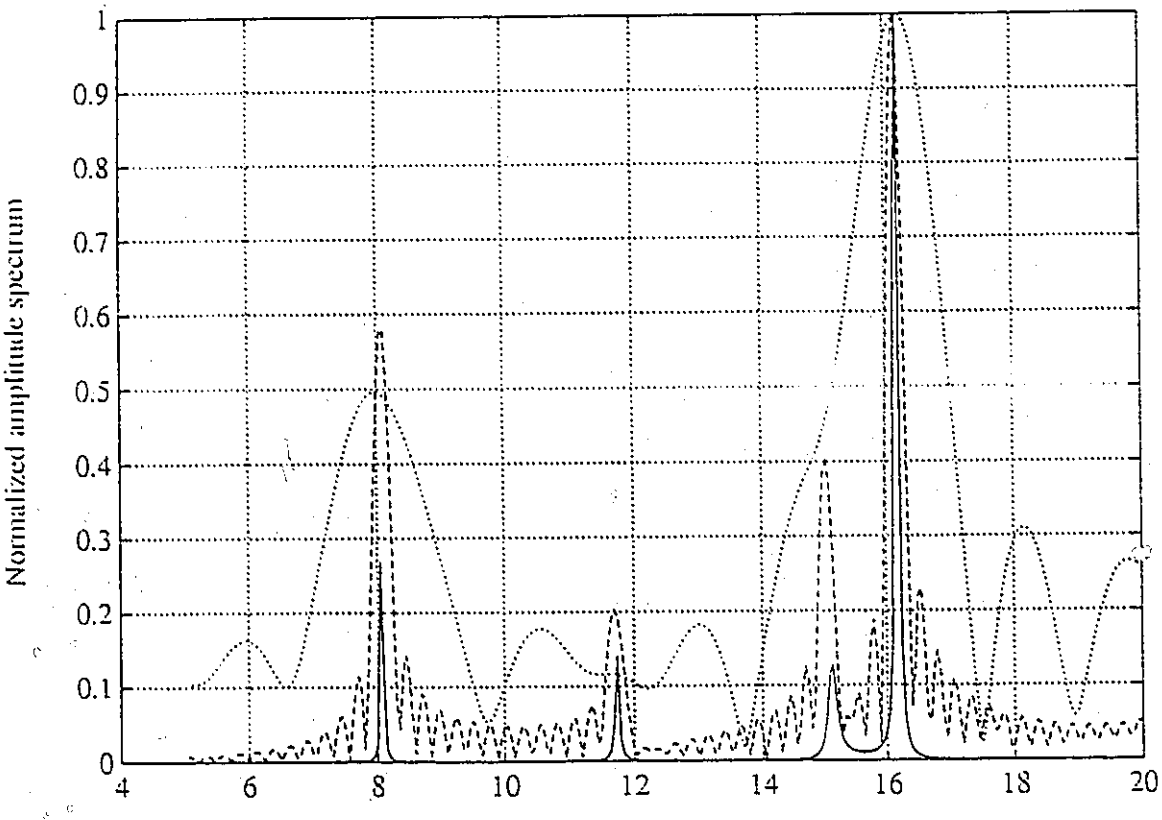
Normalized amplitude spectrum
Frequency GHz
0
0.1
0.2
0.3
0.4
0.5
0.6
0.7
0.8
0.9
1
4
6
8
10
12
14
16
18
20

(a)

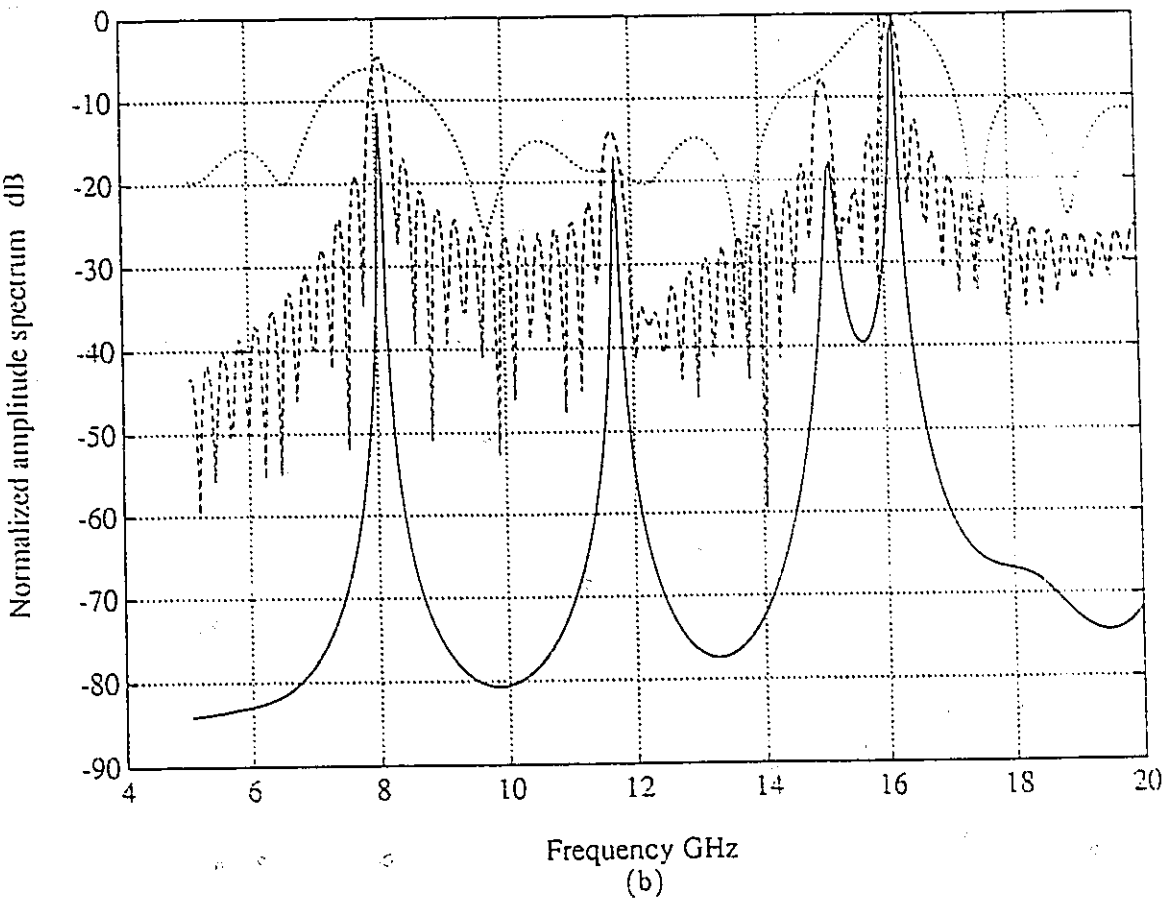

Figure 4.5: Resonant frequency estimation using different methods. Dashed line: 20000 iterations and using Fourier integration Eq. (10). Dotted line: 2000 time iterations and using Fourier integration Eq.(10). Solid line: Using 2000 time iterations in FD-TD algorithm and using digital filter processing and MUSIC method.

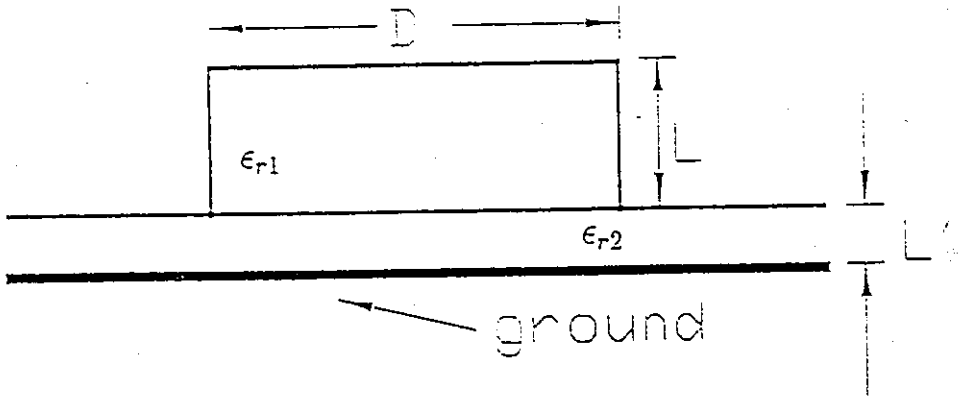

Figure 4.6: Semi-open dielectric resonator on a microstrip substrate.

Table 4.1: Resonant frequencies for the $TE_{01\delta}$ mode of a semi-open DR.

L' (mm)	FD-TD results (GHz)	measured results (GHz)
1.59	4.9680	4.9832
3.18	4.7770	4.7918

Chapter 5

MICROSTRIP ANTENNA ANALYSIS USING THE FD-TD TECHNIQUE

5.1 Background

The popularity of planar printed antennas has steadily increased over the past decade, or so, due to a number of advantages: such as, low cost, low weight, low profile, conformability with existing structures, and ease of fabrication and integration with active devices. During this period of time they have become an important area of study within the antenna community and have led to a major innovation in antenna theory. Usually printed antennas are fabricated on a substrate, or on a number substrates backed by a metallic sheet (the ground plane). The radiating elements, consisting of thin metallic patches or slots in metallic sheet, are located at an interface, commonly consisting of a dielectric and air. Multilayered or stacked structures are often used to increase antenna bandwidth. This can be achieved, for example, by simply introducing an air-gap between the dielectric layers. Usually the bandwidth can be increased to more than 10 percent. Practically, there are three common

structures that are used to feed planar printed antennas. These are coaxial probe feeds, microstrip line feeds, and aperture coupled feeds. The coaxial-fed structure is often used in a single element or a small array because of the ease of matching its characteristic impedance to that of the antenna; and, as well, the parasitic radiation from the feed network tends to be insignificant. Furthermore, it can also be used as the transition from a printed circuit located on one side of a substrate to the printed antenna on the other side. Compared to probe feeds, microstrip line-fed structures are more suitable for large arrays due to the ease of fabrication and lower-costs, but the serious drawback of this feed structure is the strong parasitic radiation [58]. The aperture-coupled structure has all of the advantages of the former two structures, and isolates radiation from the feed network, thereby leaving the main antenna radiation uncontaminated. All three of these practical feed structures will be discussed in this chapter.

To date, many numerical techniques [58]-[63] have been developed to analyze planar printed antennas in the spectral domain. For coaxial-fed patch antennas, the earliest model to be adopted for full-wave analysis is the delta current source model [59]. The model is based on the use of sinusoidal expansion modes and the assumption that the current on the probe is constant. The assumption restricts the model to the point where reasonable results can only be obtained near the resonant frequency of the patch antenna. Another popular model is based on sophisticated attachment models [60], in which the excitation current is spread over a charge cell. This model was developed to be compatible with roof-top basis functions. Unfortunately, the resulting matrix needs to be carefully treated because it is severely ill conditioned in the vicinity of the resonant frequency. Recently, a more accurate spectral domain model was developed [61], in which the fringing field is replaced by a frill of magnetic current. However, the discontinuity between the coaxial line and the patch substrate, as well as the higher order modes near the connector region, cannot be easily accounted for, even though a primary TEM mode excitation concept is incorporated in the

model. It is found that, spectral domain methods can provide a more accurate model for microstrip line-fed antennas than for coaxial-fed antennas, even though some non-practical assumptions must be imposed in the line-fed model. A number of assumptions, such as the transverse directed currents [62] not being taken into account and little consideration being given to contributions from higher order modes propagating down the feed line, will cause the numerical results to diverge as the frequency increases. Furthermore, when an antenna consists of a multilayered structure, the spectral domain methods become more difficult to use because of the complexity of the Sommerfeld-type integral treatment.

The Finite-Difference Time-Domain method has been widely used to solve electromagnetic problems since 1966. Since Maxwell's equations are discretized directly, using central difference, in both space and time, the FD-TD method is more flexible for modeling complex structures. In the last few years, a number of investigators have used the FD-TD method to analyze microstrip problems [49]-[54], but in the case of the coaxial-line feed problem, the analysis is based on assumptions that deviate from practice. For example, the discontinuity between the coaxial line and patch region is replaced by an equivalent lump resistance, and as well, the characteristic impedance of the coaxial line is not included in the model [54]. Obviously, it is very difficult to obtain an accurate equivalent resistance to incorporate all of the effects of the discontinuity near the connector, especially if the modeling is being carried out over a wide frequency range. On the other hand, although a number of researchers have given attention to modeling line-fed printed antennas using the FD-TD method, as of yet, none has addressed the problem of strong dispersion when the dielectric constant is high. This situation will be addressed in this chapter using the dispersive boundary condition presented in Chapter 3.

In this chapter it will be shown that the FD-TD method provides a technique for accurate modeling of planar printed antennas. There are three features of this full-wave analysis technique that will be highlighted. First, rather than being limited to treatment

of simple printed antenna structures, this study focuses on complex printed antennas, such as microstrip line-fed aperture coupled stacked microstrip antennas and coaxial-fed stacked microstrip antennas. Second, a coaxial feed model is presented, which provides a robust description of probe feeds, as well as allowing for modelling of complex printed antennas. The model takes into account contributions from the higher order modes at the junction between the probe and the antenna. The validity of the model is demonstrated by a comparison of simulated and experimental results. The example, which will be discussed in detail, is the coaxial-fed stacked microstrip antenna. The third feature of this paper is the novel use of a dispersive boundary condition. Its implementation will be shown to be quite straightforward. This boundary condition is useful in analyzing printed antenna structures which contain microstrip lines, where the dielectric constant of the line is high.

The antenna structures that are analyzed in this chapter can be considered to be representative of printed antenna structures. As well, the results of the sophisticated numerical treatment will be shown to be in excellent agreement with the experimental results over a very wide frequency range. The experimental results that are used to validate the numerical modelling were obtained using an HP8510B network analyzer. Details with regards to calibration and measurement error will be provided in the following sections.

5.2 Discretization of Maxwell's Equations

The generalized microstrip antenna under analysis is shown in Fig. 5.1, where the patch, feed line, and the ground plane are made of a perfect conductor ($\sigma = \infty$) and the substrate has a relative dielectric constant of ϵ_r. The structure is assumed to be in an open environment, that is, above the dielectric and the metal strip surface, free space is assumed to extend to infinity; in the horizontal direction, apart from the discontinuity region, the substrate-ground structure also extends uniformly into infinity.

The Maxwell equations governing the solution of this problem are

$$\frac{\partial \vec{E}}{\partial t} = \frac{1}{\epsilon_i} \bigtriangledown \times \vec{H} \tag{5.1}$$

$$\frac{\partial \vec{H}}{\partial t} = -\frac{1}{\mu_o} \bigtriangledown \times \vec{E} \tag{5.2}$$

where i=1,2 represents the substrate and the free-space region, respectively. At the interface of the two regions, the field continuity conditions are enforced.

For the uniqueness of the solutions to these Maxwell equations, the following conditions must be satisfied: (i) The initial condition for the fields must be specified on the whole domain of interest; that is, $\vec{E}(\vec{r}, t = 0)$ and $\vec{H}(\vec{r}, t = 0)$ must be given everywhere inside the computation domain; (ii) The tangential components of $\vec{E}$ and $\vec{H}$ on the boundary of the domain of interest must be given for all $t > 0$. For the boundary at infinity, Sommerfeld's radiation condition must be satisfied, that is, the wave at infinity must be of an outgoing type.

In a rectangular coordinate system (x,y,z), Maxwell's curl equations may be written in component form as,

$$\frac{\partial H_x}{\partial t} = \frac{1}{\mu}(\frac{\partial E_y}{\partial z} - \frac{\partial E_z}{\partial y}) \tag{5.3}$$

$$\frac{\partial H_y}{\partial t} = \frac{1}{\mu}(\frac{\partial E_z}{\partial x} - \frac{\partial E_x}{\partial z}) \tag{5.4}$$

$$\frac{\partial H_z}{\partial t} = \frac{1}{\mu}(\frac{\partial E_x}{\partial y} - \frac{\partial E_y}{\partial z}) \tag{5.5}$$

$$\frac{\partial E_x}{\partial t} = \frac{1}{\epsilon}(\frac{\partial H_z}{\partial y} - \frac{\partial H_y}{\partial z}) \tag{5.6}$$

$$\frac{\partial E_y}{\partial t} = \frac{1}{\epsilon}(\frac{\partial H_x}{\partial z} - \frac{\partial H_z}{\partial x}) \tag{5.7}$$

$$\frac{\partial E_z}{\partial t} = \frac{1}{\epsilon}(\frac{\partial H_y}{\partial x} - \frac{\partial H_x}{\partial y}). \tag{5.8}$$

The system of the above six coupled partial differential equations of (5.3)-(5.8) forms the basis of the FD-TD algorithm for electromagnetic wave interactions with general three-dimensional objects.

In order to find an approximate solution to this set of equations, the problem is discretized over a finite three dimensional computational domain. Discrete approximations to these continuous partial differential equations are obtained by using the centered difference approximation to the first-order partial differentials in both the time and space domains.

$$\frac{\partial f}{\partial x} = \frac{f(x+\Delta x/2,t) - f(x-\Delta x/2,t)}{\Delta x} + O(\Delta x^2) \tag{5.9}$$

$$\frac{\partial f}{\partial t} = \frac{f(x,t+\Delta t/2) - f(x,t-\Delta t/2)}{\Delta t} + O(\Delta t^2). \tag{5.10}$$

To achieve the accuracy of (5.9), and to realize all of the required space derivatives of the system of (5.3)-(5.8), Yee [1] positioned the components of $\vec{E}$ and $\vec{H}$ about a unit cell of the lattice as shown in Fig. 5.2. To achieve the accuracy of (5.10), he evaluated $\vec{E}$ and $\vec{H}$ at alternate half time steps. To be more specific, if the components of $\vec{E}$ is at time $n\Delta t$, the components of $\vec{H}$ are calculated at $(n+1/2)\Delta t$. For this reason, this algorithm is also called the leapfrog method. The explicit finite difference approximations to (5.3)-(5.8) are

$$\begin{aligned} H_x^{n+\frac{1}{2}}(i,j,k) &= H_x^{n-\frac{1}{2}}(i,j,k) - \frac{\Delta t}{\mu} \\ &\cdot \left[\frac{E_z^n(i,j,k) - E_z^n(i,j-1,k)}{\Delta y} \right. \\ &\left. - \frac{E_y^n(i,j,k) - E_y^n(i,j,k-1)}{\Delta z} \right] \end{aligned} \tag{5.11}$$

$$\begin{aligned} H_y^{n+\frac{1}{2}}(i,j,k) &= H_y^{n-\frac{1}{2}}(i,j,k) - \frac{\Delta t}{\mu} \\ &\cdot \left[\frac{E_x^n(i,j,k) - E_x^n(i,j,k-1)}{\Delta z} \right. \\ &\left. - \frac{E_z^n(i,j,k) - E_z^n(i-1,j,k)}{\Delta x} \right] \end{aligned} \tag{5.12}$$

$$\begin{aligned} H_z^{n+\frac{1}{2}}(i,j,k) &= H_z^{n-\frac{1}{2}}(i,j,k) - \frac{\Delta t}{\mu} \\ &\cdot \left[\frac{E_y^n(i,j,k) - E_y^n(i-1,j,k)}{\Delta x} \right. \\ &\left. - \frac{E_x^n(i,j,k) - E_x^n(i,j-1,k)}{\Delta y} \right] \end{aligned} \tag{5.13}$$

$$E_x^{n+1}(i,j,k) = E_x^n(i,j,k) + \frac{\Delta t}{\epsilon} \cdot \left[\frac{H_z^{n+\frac{1}{2}}(i,j+1,k) - H_z^{n+\frac{1}{2}}(i,j,k)}{\Delta y} - \frac{H_y^{n+\frac{1}{2}}(i,j,k+1) - H_y^{n+\frac{1}{2}}(i,j,k)}{\Delta z} \right] \tag{5.14}$$

$$E_y^{n+1}(i,j,k) = E_y^n(i,j,k) + \frac{\Delta t}{\epsilon} \cdot \left[\frac{H_x^{n+\frac{1}{2}}(i,j,k+1) - H_x^{n+\frac{1}{2}}(i,j,k)}{\Delta z} - \frac{H_x^{n+\frac{1}{2}}(i+1,j,k) - H_x^{n+\frac{1}{2}}(i,j,k)}{\Delta x} \right] \tag{5.15}$$

$$E_z^{n+1}(i,j,k) = E_z^n(i,j,k) + \frac{\Delta t}{\epsilon} \cdot \left[\frac{H_y^{n+\frac{1}{2}}(i+1,j,k) - H_y^{n+\frac{1}{2}}(i,j,k)}{\Delta x} - \frac{H_x^{n+\frac{1}{2}}(i,j+1,k) - H_x^{n+\frac{1}{2}}(i,j,k)}{\Delta y} \right] \tag{5.16}$$

The entire computational domain is formed by stacking the basic rectangular cells into a rectangular volume shown in Fig. 5.1. With the system of finite-difference equations represented by (5.11)-(5.16) the new value of a field vector component at any lattice point depends only on its previous value and on the four surrounding previous values of the components of the other field vector. Therefore, at any given time step, the computation of a field vector can proceed either one point at a time; or, if p parallel processors are employed concurrently, p points at a time.

The above FD-TD scheme is specially suitable for microstrip component analysis due to the following advantages. First, there is no need for special treatment at the edge of a microstrip antenna or transmission line if the tangential $\vec{E}$ and vertical $\vec{H}$ components are located on the metal strip and only the parallel components of the electric field are located

on the edge of the strip. Second, because the discretization steps used in the analysis of microstrip components are very small, the numerical dispersion of the above scheme is negligible compared to the physical dispersion of the microstrip structure. Finally, the central difference nature of the leapfrog method makes it a relatively accurate method (second-order accuracy in both time and space), and makes it a very direct method from a mathematical point of view compared to the other time domain methods.

For finite difference scheme (5.11)-(5.16), a stability condition must be found which guarantees that the numerical error generated in one step of the calculation does not accumulate and grow, and which guarantees that the approximate solution derived using the numerical scheme converges to the theoretical one. The stability condition of Yee's algorithm is [46]

$$v_{max} \cdot \Delta t \leq \frac{1}{\sqrt{\frac{1}{\Delta x^2} + \frac{1}{\Delta y^2} + \frac{1}{\Delta z^2}}}. \tag{5.17}$$

For the special case of $\Delta x = \Delta y = \Delta z = \Delta h$, (5.17) becomes

$$v_{max} \cdot \Delta t \leq \frac{1}{\sqrt{3}} \cdot \Delta h \tag{5.18}$$

where v_{max} is the maximum electromagnetic wave phase velocity within the media being modeled. Usually the space steps in the FD-TD technique are determined in such a way that the fine parts of the structure can be modeled accurately. Then, the time step is limited by the above stability condition.

The finite difference form (5.11)-(5.16) of Maxwell's equations is derived in the uniform region of the medium and therefore cannot be applied directly to the nodal points located on the dielectric-air interface, on conductors, or on the boundary planes of the finite difference mesh. All these points require special treatment.

The field components which lie on the dielectric-air interface are the tangential components of $\vec{E}(E_y$ and $E_z)$ and the vertical component of $\vec{H}(H_x)$. In calculating H_x,

the difference equation similar to (5.11) can still be used because the value of μ does not change across the boundary, and because the E_y and E_z components used to calculate H_y are the tangential components with respect to the interface and are thus continuous across the boundary. To calculate E_y and E_z, however, finite difference formulation other than (5.15) and (5.16) must be derived from the field continuity conditions across the boundary [52]. The derived result is that E_y can be obtained by the discretization form of

$$\frac{\epsilon_1 + \epsilon_2}{2} \cdot \frac{\partial E_y}{\partial t} = \frac{\partial H_y}{\partial z} - \frac{\Delta H_z}{\Delta x} \tag{5.19}$$

and E_z can be obtained through

$$\frac{\epsilon_1 + \epsilon_2}{2} \cdot \frac{\partial E_z}{\partial t} = \frac{\Delta H_y}{\Delta x} - \frac{\partial H_x}{\partial y}. \tag{5.20}$$

In other words, the average value of ϵ is used in (5.15) and (5.16) for the calculation of the interface E_y and E_z nodes.

The microstrip and the ground planes are assumed to be perfectly conducting and have zero thickness and are treated by setting the tangential electric fields, E_y and E_z, and normal magnetic fields, H_x, to zero. In Yee's FD-TD scheme, the boundary condition imposed on the normal magnetic field is automatically satisfied by the finite difference calculations if the tangential electric fields have been specified.

The computation domain can be reduced by one-half if one applies a magnetic wall boundary condition at the center of the structure if the analyzed structures are symmetric. In some analyses, we apply a direct magnetic wall boundary condition, that is, the tangential magnetic components and the normal electric components are forced to be zero on this wall, instead anti-symmetrical tangential magnetic field condition and symmetrical tangential electrical field condition are applied. In this way, the geometry of the analyzed antennas can be more accurately aligned.

Since the computation domain cannot include the whole space, the finite difference

mesh must be truncated to accommodate the finite size of computer memories. The truncation planes are the side, top, and end surfaces (Fig. 5.1). The numerical algorithm on the truncation planes must simulate the propagation of the outgoing waves; this is known as the artificial *absorbing boundary condition* (ABC). In order to achieve an accurate result, a good ABC has to be used. In the next section, we will discuss the used absorbing boundary conditions in details.

5.3 Absorbing Boundary Conditions

The primary property of the boundary condition is that the boundary is transparent to the wave propagating out with respect to the computational domain. There are several ways to simulate this property. Perhaps the simplest and most obvious means of eliminating reflections at the mesh walls is to pad the computational domain with lossy regions which absorb the incident waves [54]. But, it has been demonstrated that the layer should be relatively thick in order to absorb the outgoing waves without generating significant reflections. The second way to obtain this property is to impose an artificial boundary condition. The most common methods used to derive absorbing boundary conditions are based on asymptotic expansion of the one-way wave equation. Many researchers have developed theories to derive these approximate boundary conditions [19]-[27]. Here, a derivation of the one-way absorbing boundary condition based on the work of Mur [22] is presented in order to understand ABC, and to further study the relationship between the ABC and DBC.

Without loss of generality, a wave inside the computational domain is assumed to be travelling in the $+z$ direction incident on the mesh boundary at $z = M\Delta z$. A continuous space is first assumed and the boundary conditions required to prevent reflections at the $z = M\Delta z$ boundary are derived. The medium is assumed to be lossless and uniform, without free currents or charge density. Any single component of the electric or magnetic

field, represented by ϕ, satisfies the scalar wave equation in cartesian coordinates,

$$\left(\frac{\partial^2}{\partial x^2}+\frac{\partial^2}{\partial y^2}+\frac{\partial^2}{\partial z^2}-\frac{1}{c^2}\frac{\partial^2}{\partial t^2}\right)\phi=0. \tag{5.21}$$

A plane wave travelling in the computational domain in the z direction can be expressed as,

$$\phi = e^{j(\omega t-k_x x-k_y y-k_z z)} \tag{5.22}$$

For perfect absorption the wave must satisfy the one-way or first order wave equation,

$$\left(\frac{\partial}{\partial z}+\frac{1}{v_z}\frac{\partial}{\partial t}\right)\phi=0 \tag{5.23}$$

or

$$\left(\frac{\partial}{\partial z}+\frac{k_z}{\omega}\frac{\partial}{\partial t}\right)\phi=0 \tag{5.24}$$

where $k^2=k_x^2+k_y^2+k_z^2$ and therefore $k_z=(k^2-k_x^2-k_y^2)^{\frac{1}{2}}$. Substituting for k_z,

$$\left(\frac{\partial}{\partial z}+\frac{1}{c}\sqrt{1-\frac{k_x^2}{k^2}-\frac{k_y^2}{k^2}}\frac{\partial}{\partial t}\right)\phi=0 \tag{5.25}$$

where $k=\omega/c$. The first approximation to this equation is to assume approximately normal incidence, or $k_x\approx 0$ and $k_y\approx 0$. In this case the boundary condition simplifies to

$$\left(\frac{\partial}{\partial z}+\frac{1}{c}\frac{\partial}{\partial t}\right)\phi=0. \tag{5.26}$$

This equation is readily discretized by using centered differences at $z=(M-1/2)\Delta z$ and at $t=n+1/2$ in the following manner,

$$\frac{1}{2}\left(\frac{\phi_M^{n+1}-\phi_{M-1}^{n+1}}{\Delta z}+\frac{\phi_M^{n}-\phi_{M-1}^{n}}{\Delta z}\right)+\frac{1}{2c}\left(\frac{\phi_M^{n+1}-\phi_M^{n}}{\Delta t}+\frac{\phi_{M-1}^{n+1}-\phi_{M-1}^{n}}{\Delta t}\right)=0 \tag{5.27}$$

which reduces to,

$$\phi_M^n=\phi_{M-1}^{n-1}+\frac{1-\rho}{1+\rho}(\phi_M^{n-1}-\phi_{M-1}^{n}), \tag{5.28}$$

where ϕ_M represents the field components on the boundary, ϕ_{M-1} represents field component a distance of one node inside the boundary, and $\rho=c\Delta t/\Delta z$. This is the so-called first order ABC which was presented by Mur [22] for application to the FD-TD method.

For the microstrip antenna analysis, on the feed lines the waves are normally incident to the mesh walls. It should be noted that the normal incidence assumption is not valid for the fringing fields which are propagating tangential to the side walls, therefore the side walls should be far enough away that the fringing fields are negligible at the walls. Additionally, radiation is not generally normal to the mesh walls. Therefore a higher order absorbing boundary condition is necessary to handle problems in which radiation is a significant factor.

The one-way wave equation (5.25) is again considered, and it is observed that if the directions of propagation, i.e. k_x and k_y, were known, then this expression could be used to develop an exact absorbing boundary condition for the specified direction of propagation. Using this idea the more general case where the direction of propagation is near normal with $k_x \ll 0$ and $k_y \ll 0$ is considered. In this case the square root in (5.25) may be approximated to yield,

$$\left[\frac{\partial}{\partial z} + \frac{1}{c}\left(1 - \frac{1}{2k^2}(k_x^2 + k_y^2)\right)\frac{\partial}{\partial t}\right]\phi = 0. \tag{5.29}$$

If this expression is differentiated with respect to time,

$$\left[\frac{\partial^2}{\partial z \partial t} + \frac{1}{c}\left(\frac{\partial^2}{\partial t^2} - \frac{c^2}{2}(k_x^2 + k_y^2)\frac{1}{\omega^2}\frac{\partial^2}{\partial t^2}\right)\right]\phi = 0. \tag{5.30}$$

For plane wave solution the following relations hold

$$\frac{\partial^2}{\partial t^2} \leftrightarrow -\omega^2, \quad \frac{\partial^2}{\partial x^2} \leftrightarrow -k_x^2, \quad \frac{\partial^2}{\partial y^2} \leftrightarrow -k_y^2 \tag{5.31}$$

Using these relations to go back to a differential equation,

$$\left[\frac{1}{c}\frac{\partial^2}{\partial z \partial t} + \frac{1}{c^2}\frac{\partial^2}{\partial t^2} - \frac{1}{2}\left(\frac{\partial^2}{\partial x^2} + \frac{\partial^2}{\partial y^2}\right)\right]\phi = 0, \tag{5.32}$$

which is the continuous second order absorbing boundary condition. The finite difference approximations for this equation make use of time and space averaging to achieve centered differences in space and time in a manner similar to the first order absorbing boundary condition [49]. The above equation is much more absorbent than the strictly normal incidence

boundary condition (5.26) although it still assumes that the angle of incidence is close to being normal. However, for microstrip component analysis, this second boundary condition has a number of disadvantages when compared with the first order boundary condition. these are (i) the implementation of the boundary condition is much more complicated than the first order boundary condition since the discretized second order boundary condition needs the values on nine neighboring nodes while first order ABC needs the value only on one neighbor node; (ii) because the metallic or dielectric boundaries intersect the outer boundaries, this makes it very difficult to apply the second order boundary condition; (iii) the corner treatment of the computational domain with (5.32) is not as easy as with the normal incident boundary condition (5.26). Overall, the normal incidence boundary condition is much easier to apply for these situations as it has no derivatives tangential to the walls.

Considering the above factors, Mur's first order absorbing boundary condition (5.28) is used to evaluate the tangential field components on almost all the mesh walls. The most important factor to be considered when applying the boundary conditions is the proper selection of the phase velocity. For aperture-coupled stacked antennas and for the side and the end walls, we choose local phase velocities, that is, inside the dielectric the velocity is determined by the local ϵ_r and below and above the dielectric the velocity is determined by $\epsilon_r = 1.0$. On the front feed line wall, a new boundary condition, the *dispersive boundary condition* (DBC), is applied to absorb the dispersive wave on the microstrip line.

In the FD-TD simulation of microstrip circuits and antennas. it was observed that most of the energy propagating towards the radiating element comes out or is reflected back onto the feed stripline. So the accuracy of the frequency domain results is greatly dependent on the absorbing boundary condition applied on this wall. Usually, nearly applying the Mur's first order ABC will leave a visible amount of reflection. This is mainly due to the velocity of the wave on the stripline not being a constant but rather being a function of

frequency [52, 49]. In order to absorb this dispersive wave, Zhang and Mei [52] have used the super boundary condition treatment proposed by Fang [17, 18]. This treatment consists of four steps:

1. Apply Mur's first order ABC (5.28) to the tangential electrical fields on the boundary walls;

2. Use the electrical field values calculated in procedure 1 and use the finite-difference equations to calculate the tangential $\vec{H}$ next to the boundary;

3. Apply the same kind of boundary condition on the tangential $\vec{H}$ next to the boundary;

4. Compare the values obtained in procedures 2 and 3. These two $\vec{H}$ fields will always have the property that the errors contained in them due to imperfect treatment of the boundary condition will have opposite signs and the magnitudes of these errors will maintain a known ratio. By using a weighted average of these two $\vec{H}$ we get an error cancellation effect and obtain the final $\vec{H}$.

The fortuitous cancellation of errors that occurred above can actually result in an improved performance for the boundary condition. However, it is felt that the derivation of boundary condition needs both simplification and a strong theoretical foundation. Therefore, a new boundary condition should be presented which takes into account the dispersive characteristics of the microstrip line. This boundary condition is called as *dispersive boundary condition* (DBC), which has been discussed systematically in Chapter 3. For high dielectric constant microstrip component analysis, the DBC (3.37) presented in Chapter 3 is used.

5.4 Designing the Excitation

The FD-TD technique used for microstrip component analysis consists of three key components: i.e. the finite-difference scheme, the boundary condition used to truncate the computational domain, and the source of excitation that is used to get the whole process going. This section will discuss the types of sources that are used to provide excitation for FD-TD analysis.

In the case of planar printed antenna problems, microstrip lines and coaxial probes are the basic structures which are used as feeds. When $t = 0$, all the fields in the computational domain are set to zeros. Then, a Gaussian pulse is used as the source of excitation in the time domain because its smooth Gaussian shaped spectrum can provide information from DC to the desired frequency simply by adjusting the width of the pulse. In the spatial domain, the fields on the excitation plane are specified with a desired mode distribution.

5.4.1 Source Treatment for Line-Fed Microstrip Antennas

In the case of microstrip line or microstrip line-fed problems, in order to simulate a voltage source excitation it is necessary to impose the vertical electric field, E_x, in a rectangular region underneath the stripline. The remaining electric field components on the source plane might be specified in different ways. In [52], an electric wall source is used; i.e. the remaining electric field components on the source wall of the mesh are set to zero. An unwanted side effect of this type of excitation is that a sharp magnetic field is induced tangential to the source wall and that the pulse is reduced in magnitude. This will cause trouble in the absorbing boundary condition treatment [52]. Another excitation scheme is to simulate a magnetic wall at the source plane [50]. The source plane consists only of E_x and E_y components, with the tangential magnetic field components offset by $\pm\Delta z/2$. If the magnetic wall is implemented by setting the tangential magnetic field components to

zero just behind the source plane, then significant distortion on the pulse still occurs. If the magnetic wall is enforced directly on the source plane by using image theory; i.e. H_{tan} outside the magnetic wall is equal to -H_{tan} inside the magnetic wall, then the remaining electric field components on the source plane may be readily calculated using the finite-difference equations. Using this excitation, the induced tangential magnetic field can be greatly reduced. Fig. 5.3 shows results for testing different sources. The dashed lines are obtained using an electric wall source, which show E_x fields just underneath the microstrip line at different locations. The solid lines are obtained using a magnetic wall source. In our analysis, we use the magnetical wall source. Although in the above a fictitious source is used, the boundary conditions will force the field to take on the realistic distributions after the wave propagates a distance of a few lattices. Once the Gausssian pulse is well clear of the front plane, the front plane is shifted forwards about ten lattices and is transformed into an absorbing boundary condition. Because the dominant mode for the microstrip line is the *quasi*-TEM mode, which is known to be dispersive, the dispersive characteristics of the waves propagating on the line must be taken into account by using a dispersive absorbing condition. This becomes more important when the dielectric constant of the substrate is very high, for example $\epsilon_r = 10.2$

5.4.2 Source Treatment for Coaxial-Fed Patch Antennas

The coaxial line-fed connection is a critical part of coaxial-fed patch antennas and needs a special treatment. The curved boundary of the inner and outer conductors of a coaxial line is approximated by staircasing, and the tangential components of the electrical field are forced to zero at the conductor surface.

As shown in Fig. 5.4, the inner conductor of the coaxial line is attached to the patch antenna going through the dielectric substrate and outer conductor is connected

to the ground plane. In the coaxial-fed model. the antenna is divided into two regions for the purpose of easy computation. One is the coaxial line region and the other is the patch antenna region. These two regions are carefully merged near the ground interface. Although, the boundary of the coaxial line is approximated by using staircasing, the extent to which waves are scattered into the coaxial line is largely determined by the characteristic impedance of the coaxial line, i.e. its electric characteristics, but seldom upon the specific shape, i.e. its physical characteristics [78]. It is interesting to observe that a very good numerical result can be obtained provided that the numerical characteristic impedance of the coaxial line is almost the same as that of the coaxial line used in the measurement. The importance of the model is that the computational effort needed for the coaxial line region is less than 2% of that for the patch antenna region.

From a knowledge of the modes that exist on a coaxial line, a simple field distribution can be specified at the excitation plane in such a way that the field components in the rectangular coordinate system take on the projected values of the analytically radial field distribution. The non-TEM modes which are excited by the non-physical excitation will decay after propagating at most a few lattices. The only mode which is able to propagate down the coaxial line is the TEM mode. Since the TEM mode is a non-dispersive wave, the first order absorbing boundary condition will absorb almost all of the wave that is reflected by the antenna and which travels backwards towards the excitation plane of the coaxial line.

5.5 Variable Mesh and Multigrid Methods

In microstrip circuits or antennas, the thickness of the substrate is very small compared with the dimensions of the other parts of the structure, and all the discontinuities are located on the surface of the substrate. These properities restrict that a few grids must be

placed under the substrate in order to model the discontinuities accurately. If a uniform grid is used in the vertical direction, two obvious problems arise. The first is that if using the same grid size we are going to have too many grids in the vertical direction. The second problem relates to complications that arise when implementing absorbing boundary conditions. The latter usually requires a reasonable separation between the boundary and the source. Typically, it should be 0.25 to 0.5 wavelength. With a fine mesh size, these separations require the displacement of a large number of lattice points, both in the vertical and horizontal directions.

There are two methods which can be used to solve these problems. They are multigrid [13, 12] and variable mesh methods. In the first method, a locally fine uniform grid is embedded into the coarse grid. Inside each grid part, the ratio of Δt to Δh is kept the same so that in all subareas of the mesh exactly the same FD-TD algorithm can be employed. The coarse and the fine grid regions are solved simultaneously, and the boundary conditions between two regions are enforced to ensure a smooth transition.

The variable mesh method uses a mesh whose size changes gradually with distance. Only one time step is used throughout the mesh in this method, which is determined by the finest grid, while in the multigrid method each subgrid domain uses its corresponding time step. In both of these two methods, the Yee's FD-TD scheme should be used in the subdomain in order to obtain the second order accuracy relative to the local grids. The key issue that must be addressed when implementing these methods is how to deal with the transition between the coarse and fine grids. Considering that the transition with the variable mesh method is much more simplier than that of the multigrid method, the variable mesh method should be used for microstrip compoment analysis. By using this method, the node number in the computational domain can be reduced by about one-half, thereby the computational time can be reduced by about half.

Consider an interface between two latices, each with its own latice spacing, as shown in Fig. 5.5. It is observed that centered differences are maintained for all field values except E_i. At this point, a higher order finite difference scheme can be derived by fitting a second degree polynomial to the magnetic fields at three points. Here, we adopt an alternative scheme used by Sheen [49]. In this scheme, one lets $\Delta_2 = \Delta_1/3$, then centered differences are maintained by differencing H_{i+1} and H_{i-1},

$$\left(\frac{\partial H}{\partial x}\right)_{at\ E_i\ point} = \frac{H_{i+1}^{n+\frac{1}{2}} - H_{i-1}^{n+\frac{1}{2}}}{\Delta_1}. \tag{5.33}$$

The above discretization is of second order accuracy relative to the coarse grid, Δ_1.

5.6 Numerical and Experimental Results

Numerical results have been computed for four microstrip antennas, a line-fed rectangular patch antenna, a proximity coupled triangular patch antenna, an aperture-coupled stacked rectangular patch antenna, and a coaxial probe-fed stacked rectangular patch antenna. These antennas have dimensions on the order of 3 cm, and the operating frequency ranges are all less than 10 GHz. These antenna structures are chosen to be representative of printed antenna structures. As well, in each instance, we try to introduce new techniques for improving the performance of the FD-TD method when applied to analysis of the microstrip. For example, the conforming method will be tested with the proximity coupled triangular patch antenna; the dispersive boundary condition will be employed in the aperture-coupled stacked microstrip rectangular patch antenna analysis; and coaxial-fed microstrip antenna model will be demonstrated and validated by analyzing a coaxial-fed patch antenna.

All the numerical results obtained by the FD-TD method are compared with experimental results. These measurements of the input characteristics of the planar printed antennas under discussion are carried out on an HP8510B network analyzer. To set the

reference plane at a specific location, two kinds of calibration techniques are used; one is the standard coaxial line calibration and the other is the TRL calibration. The former can only be used to set the reference plane at the interface between the coaxial-cable and SMA connector. The latter can be used to set the reference plane at any place on a line, so that the effect of the coax-to-microstrip transition can be eliminated from the measured results. In the TRL calibration, three calibration kits were required; a Thru line of length l_{thru}, an open-circuit Reflect line of length $l_{open} = l_{thru}/2$, and a delay Line of length $l_{open} = l_{thru} + \Delta l$. The resulting reference planes are defined at a distance $l_{thru}/2$ from the connector to the patch antenna. The characteristic impedance and propagation constant of the three lines must be known at the center of the frequency band being tested and must be the same as those for the line, on which the reference plane is located. Usually $\Delta l = \lambda_g/4$, where λ_g is the waveguide wavelength corresponding to the center frequency in the frequency range of interest. A limitation of the TRL calibration is the fact that the only values of impedance and propagation constant for the line that are used in the calibration are those at center of the frequency band. As is well known, the characteristic impedance and effective dielectric constant for a line vary with frequency. The effects of dispersion on the microstrip line cannot be taken into account by means of experimental techniques. The limitation brought about by dispersion restricts the bandwidth of the measurements, as well as causing measurement errors, especially when the dispersion is serious.

5.6.1 Line-Fed Rectangular Microstrip Antenna

The dimensions of the microstrip antenna to be analyzed are given in Fig. 5.6. To model the antenna accurately along the x-direction, Δx is chosen such that the distance between four nodes exactly equals to the thickness. In order to correctly model the dimension of the antenna, Δy and Δz have been chosen so that an integral number of nodes will fit the rectangular patch accurately. The computational parameters used in the FD-TD analysis

are

$\Delta h = 1.59/4$ mm

$\Delta x = \Delta h,\ \ \Delta y = 1.9132\Delta h,\ \ \Delta z = 1.8416\Delta h$

$\Delta t = 0.515\Delta h/c$

Computation domain: $30\Delta x \times 55\Delta y \times 160\Delta z$

Microstrip line width: $6\Delta y$

Use of symmetry: magnetic wall divides antenna into two equal parts.

The spatial distribution of $E_x(y, z, t)$ just beneath the microstrip at 450, 600, 800, 2000, and 6000 time steps is shown in Fig. 5.7. The plots in this figure show, respectively, the Gaussian pulse traveling down the microstrip line ($t = 450\Delta t$), the moment when the pulse enters the patch ($t = 600\Delta t$ and $t = 800\Delta t$), the picture at the state of resonance ($t = 2000\Delta t$), and the residual wave after some time ($t = 6000\Delta t$). Notice that most of the energy propagating toward the radiating element is reflected back from the feed stripline. So a good absorbing boundary condition should be used at the front wall. For this example, the first order ABC is used on the front wall since the dispersion of the feed line is not serious due to its low dielectric constant.

There are many techniques that can be used for deriving the antenna's radiation pattern. For example, one can take direct advantage of the FD-TD method, because the field at any time step in the computational domain is known during the simulation process. Using an equivalence principle and assuming that the substrate is infinitely large, the air-dielectric interface can be replaced by a conductor sheet on which is superposed a magnetic current. By applying image theory, the surface magnetic current J_m can be written as

$$\mathrm{J}_m(f) = 2\mathrm{E}(f) \times \mathrm{n} \tag{5.34}$$

where $\mathrm{E}(f)$ is the electric field on the air-dielectric interface at a particular frequency and n is the outward unit vector perpendicular to the interface. After obtaining J_m and using the

free space Green's function for magnetic current, the radiation pattern is easily obtained. Fig. 5.8 shows the amplitude distribution of the equivalent magnetic current at the first resonant frequency. Clearly seen in the figure is that the field has little variation along the width of the antenna. The variation along the length of the antenna is sinusoidal like. This implies that the cavity and transmission line models are reasonable. It also should be noticed that the FD-TD method has taken into account the effect of the microstrip line feed.

The scattering coefficient for the antenna is given in Fig. 5.9. This result shows good agreement with the measured data. There is close agreement between simulated and measured values of the antenna's resonant frequencies. The scattering parameter $S_{11}(\omega)$ has been obtained by simple Fourier transform of the transient waveforms as

$$S_{11}(\omega) = \frac{\mathcal{F}\{V_r(t)\}}{\mathcal{F}\{V_i(t)\}} \tag{5.35}$$

where $V_i(t)$ and $V_r(t)$ are the incident and reflected voltages, respectively, which are obtained by numerical integration of the vertical electric field underneath the center of the microstrip line. The input impedance for the antenna may be calculated from the $S_{11}(\omega)$ by transforming the reference plane to the edge of the microstrip antenna,

$$Z_{in}(\omega) = Z_o(\omega)\frac{1 + S_{11}(\omega)e^{j2\gamma(\omega)L}}{1 - S_{11}(\omega)e^{j2\gamma(\omega)L}} \tag{5.36}$$

where $\gamma(\omega)$ is the wavenumber on the microstrip and is calculated by

$$e^{-\gamma(\omega)(z_j - z_i)} = \frac{\mathcal{F}\{V(z_j, t)\}}{\mathcal{F}\{V(z_i, t)\}}, \tag{5.37}$$

L is the distance from the edge of the antenna to the reference plane, and $Z_0(\omega)$ is the characteristic impedance of the microstrip line.

In the above analysis, the use of a uniform grid in the vertical direction resulted in a large memory requirement, thereby long computational time. In order to save the memory,

the variable mesh method discussed in the last section can be used without degrading the analysis accuracy [49].

5.6.2 Proximity Coupled Triangular Patch Antenna

In this subsection, we discuss the analysis of a triangular microstrip antenna, which is proximity coupled to a microstrip feed line. The reason that we choose the triangular shape is that we want to test the application of conforming models to microstrip component analysis.

Proximity coupling is of interest because it allows for ease of fabrication, as well as flexibility in the design of microstrip antennas. The input impedance of the antenna may be matched by varying the length of the coupling region. Additionally, the substrate is often thicker which causes the bandwidth to be larger. The actual antenna under consideration is shown in Fig. 5.10. The computational parameters used in the FD-TD analysis are

$\Delta h = 1.59/4$ mm

$\Delta x = \Delta h, \quad \Delta y = 1.4305\Delta h, \quad \Delta z = 2.4780\Delta h$

$\Delta t = 0.515\Delta h/c$

Computation domain: $50\Delta x \times 55\Delta y \times 140\Delta z$

Microstrip line width: $8\Delta y$

Use of symmetry: magnetic wall along the centre plane.

In the calculation, a conformal method has been employed to treat the triangular edges of the antenna. As discussed in Introduction, several conformable surface models for scattering problems have been developed to overcome the shortcoming of the staircasing approximation used with Yee's scheme. The *contour finite-difference time-domain method* (CFDTD) [3, 45] has been chosen in our analysis for its straightforward physical interpretation and the ease

with which it can be implemented. In *computational fluid dynamics* (CPD), this method is called *finite volume method* (FV) [9, 13]. It is derived by integrating the basic equations to be solved over a grid element (a finite volume) and then discrete approximations are applied to the resulting integral quantities on a grid element. In *computational electromagnetics*, the basic equations are the Maxwell's differential equations. Integrating these equations yields the Ampere's and Faraday's integral equations. The integral equations can be discretized on non-rectangular lattice, which is the general CFDTD method. The CFDTD method can be interpreted as the generalization of the Yee's method because the discrete approximations to the integral equations over surfaces of Yee's unit lattice produces the exact Yee's scheme.

Fig. 5.11 shows the characteristic impedance of the microstrip feed line. Fig. 5.12 shows the amplitude distribution of the equivalent magnetic current at the first resonant frequency. The scattering coefficient results, shown in Fig. 5.13, show fair agreement with the measured data. There is close agreement between the resonant frequencies derived from the simulated and measured results. The dotted line is obtained by applying a CFDTD scheme to the edges. This is similar to the one used in [3]. This result demonstrates that the improvement brought about by using the the CFDTD is very small. This is because of the very small grid size. In microstrip antenna analysis, the patchs are typically discretized using 20 to 40 grid spacings. Thus, the space steps are on the order of $\lambda/60$ to $\lambda/100$ in size.

5.6.3 Aperture-Coupled Stacked Microstrip Rectangular Patch Antenna

The topology of the aperture-coupled patch antenna [64] is similar to that for a traditional microstrip antenna, except for the fact that the microstrip patch antenna is located on one substrate, with a relative dielectric constant ϵ_{pr}, and the feed network is located on another substrate, with relative dielectric constant ϵ_{fr}. Usually, ϵ_{fr} is higher than ϵ_{pr} in

order to reduce the dimensions of the feed network. These two substrates are separated by a common ground plane. In order to couple electromagnetic power from the feed network to the patch antenna, an electrically small opening or aperture is made in the ground plane, as shown in Fig. 5.17. Since the radiator and the feeder are separated by the common ground plane, the radiation from the feed network can be eliminated from the field pattern. As well, the feed network will be decoupled from the antenna. Because ϵ_{fr} usually has a large value, the microstrip line will be strongly dispersive, thereby degrading the performance of the first order absorbing boundary condition. Fig. 5.14 shows the numerical experiments in the time domain, where the curves show the reflected waves of a Gaussian pulse from different absorbing boundary conditions. It is observed that the reflected wave for a first order boundary is about ten times greater than that from the dispersive boundary condition (3.73), and that the reflection from super boundary condition treatment is also greater than that from dispersive boundary condition. Therefore, the dispersive boundary condition is used in the analysis to be carried out. In this example, the distance between the open end of microstrip line and the center of the aperture is 3.8 mm. The two velocities that are selected for designing the absorbing boundary condition are $v_1 = c/\sqrt{7.12}$ and $v_2 = c/\sqrt{8.5}$. These correspond to frequencies 1 GHz and 8 GHz, respectively, where c is the speed of light in free space.

Fig. 5.15 and Fig. 5.16 show the amplitudes of magnetic currents on the upper patch and lower patch, respectively. Fig. 5.17 shows a Smith Chart for the input impedance of the aperture coupled stacked patch antenna. The coupling aperture length is chosen to be equal to 30 grid spaces and its width to two grid spaces. Fairly good agreement is observed between calculated and measured results over the frequency band from 3 to 5.6 GHz. This is the band in which the antenna operates most efficiently. Because of the serious dispersion in the microstrip line (Fig. 5.18 shows the characteristic impedance of the microstrip line which has been calculated using the FD-TD method), it is difficult to

develop a TRL calibration which is accurate over a wide frequency band. The measurement repeatability of the return loss is about ± 0.05 dB, and phase is about $\pm 3^0$. The observed experimental error is primarily due to the uncertainties inherent in the calibration kits that were used for the TRL calibration.

5.6.4 Coaxial Probe-Fed Stacked Rectangular Patch Antenna

The FD-TD coaxial-fed microstrip antenna model has been demonstrated and validated in [78] using both measured and numerical results. To show the applicability of the coaxial probe-fed model to more complicated printed antenna structures, the coaxial probe-fed stacked patch antenna is investigated. As shown in Fig. 5.19 the antenna consists of two patches. The coaxial probe is connected to the lower patch. An air gap is introduced between the two patches in order to increase the bandwidth of the antenna. In this example, the feed probe is located at a point which (12.5, 4) mm from the low left corner of the lower patch.

Fig. 5.19 gives the measured and calculated results for the reflection coefficient of the stacked patch antenna. It is obvious that the comparison between theory and measurement is excellent both in magnitude and phase within a wide frequency range. From the reflection coefficient we discover that the antenna has a bandwidth that exceeds 16 percent at the first resonate frequency. The return loss for this band of frequency is less than -10 dB.

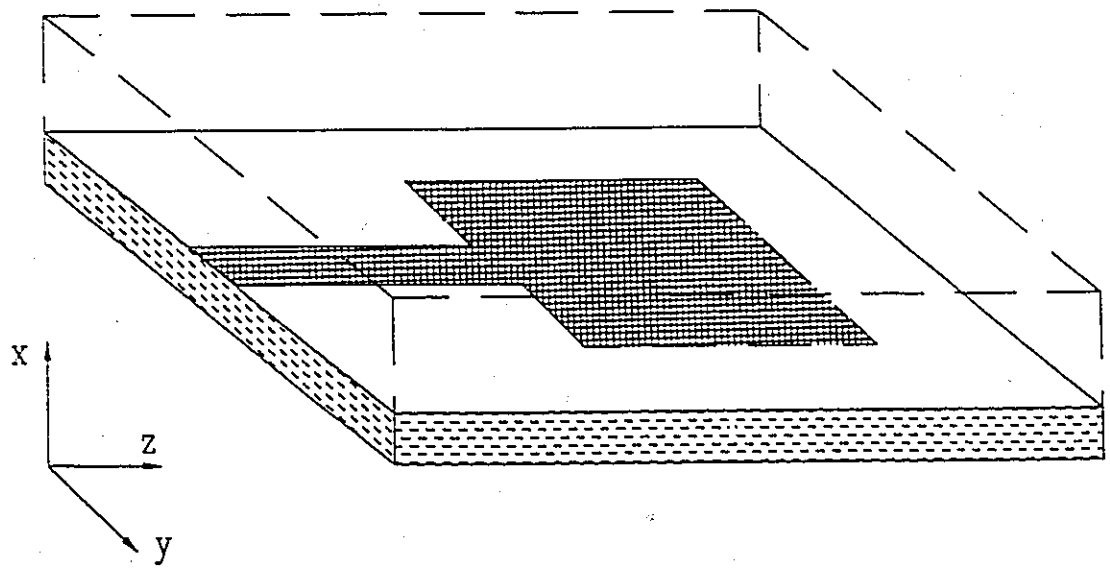

Figure 5.1: A generalized microstrip antenna enclosed in the computation domain

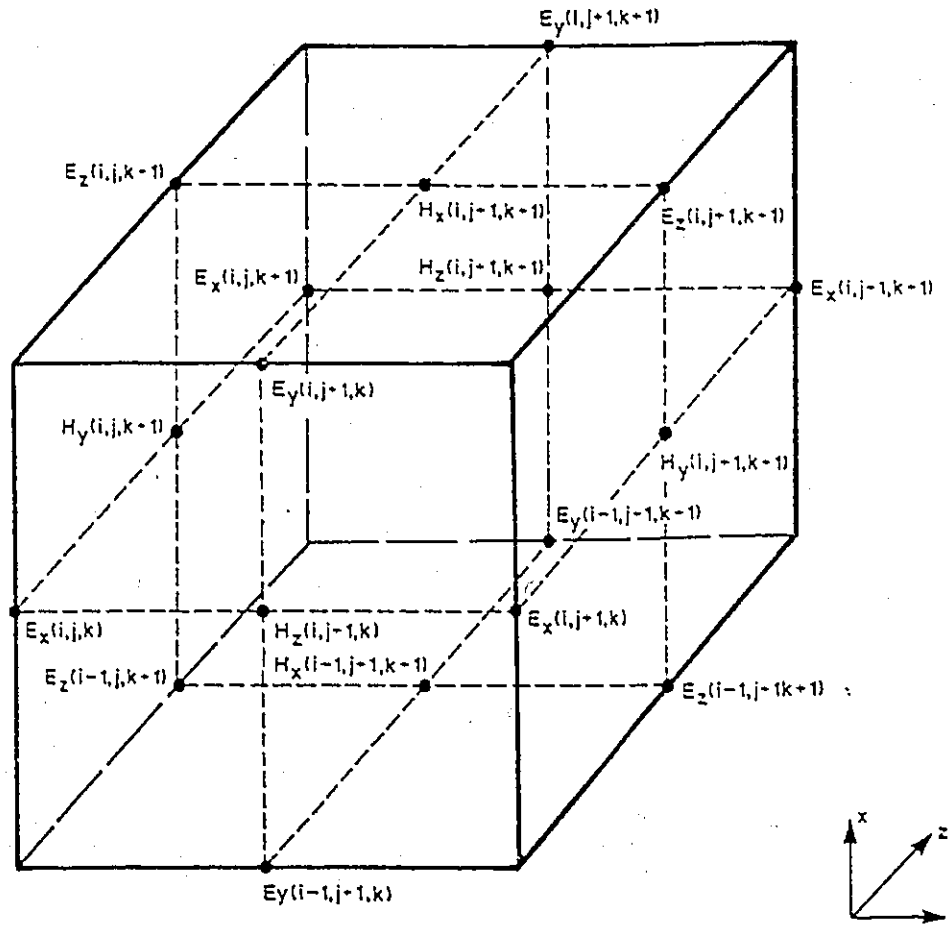

Figure 5.2: Yee's lattice

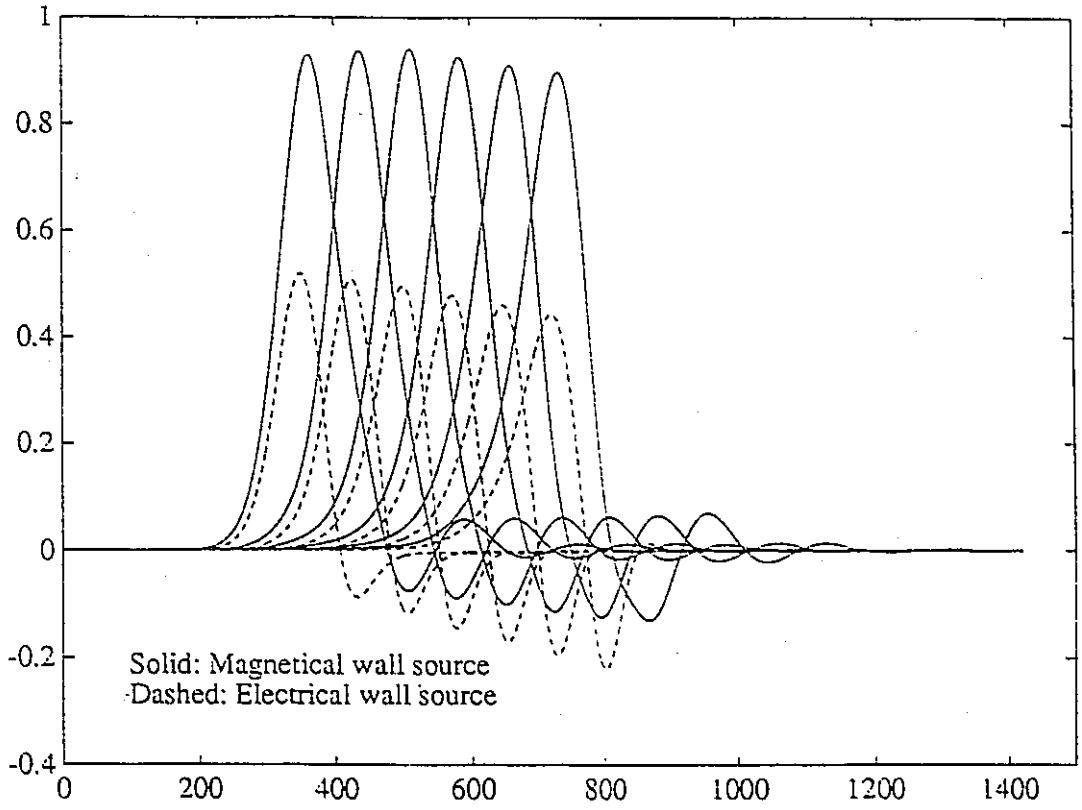

Figure 5.3: Source testing for microstrip line, Dashed line: electrical wall source; Solid line: magnetical wall source.

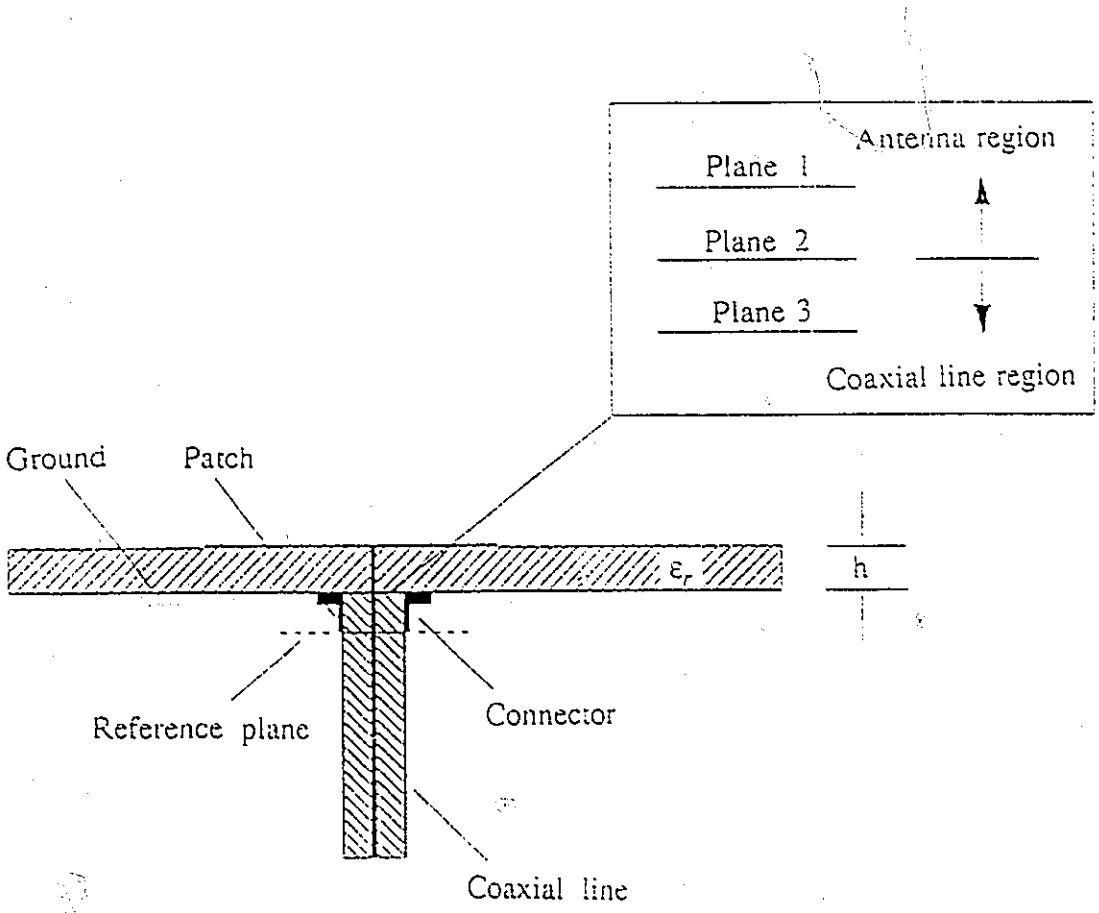

Figure 5.4: Side view of a coaxial probe-fed printed antenna

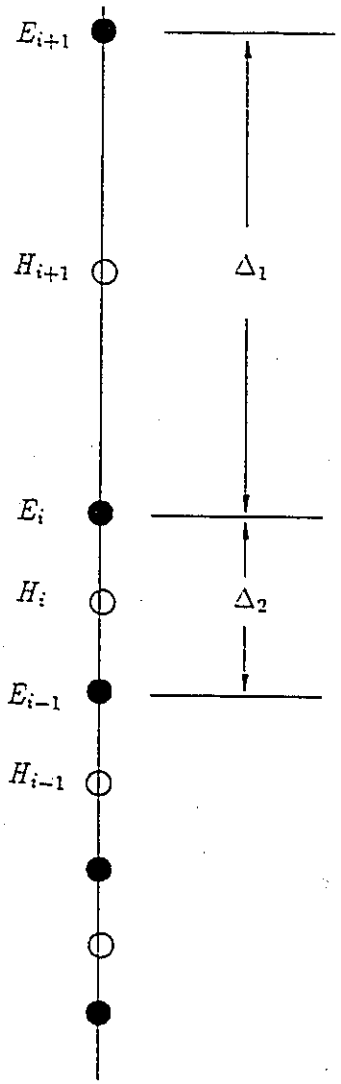

Figure 5.5: Field locations near the fine and coarse grid.

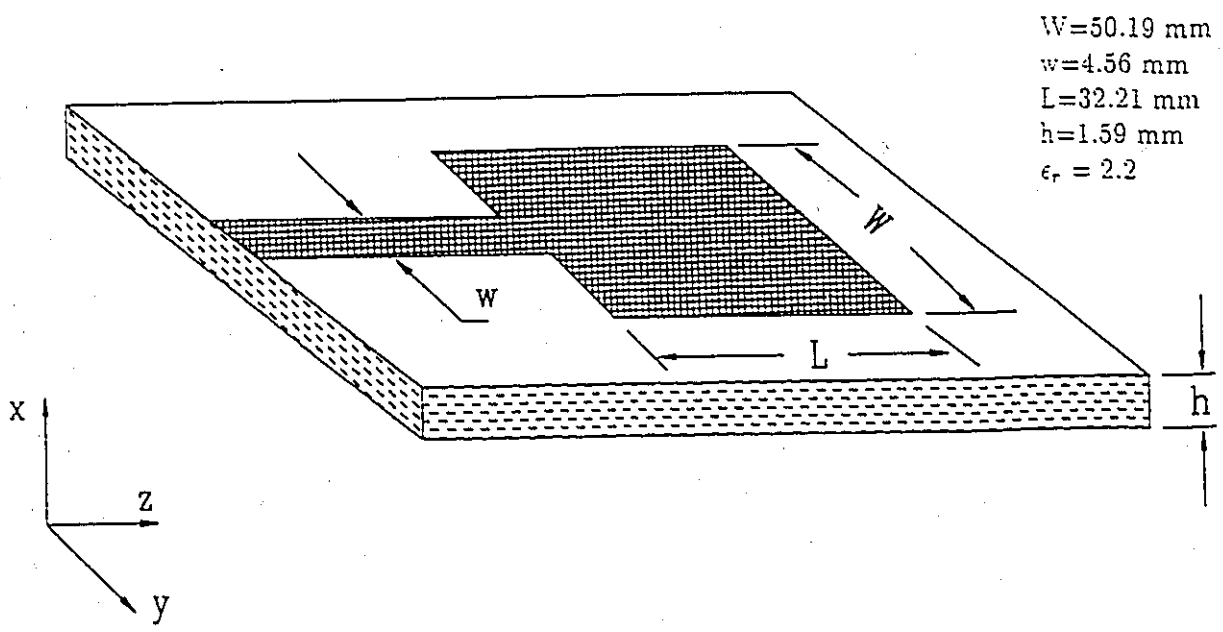

Figure 5.6: Line-fed rectangular microstrip antenna.

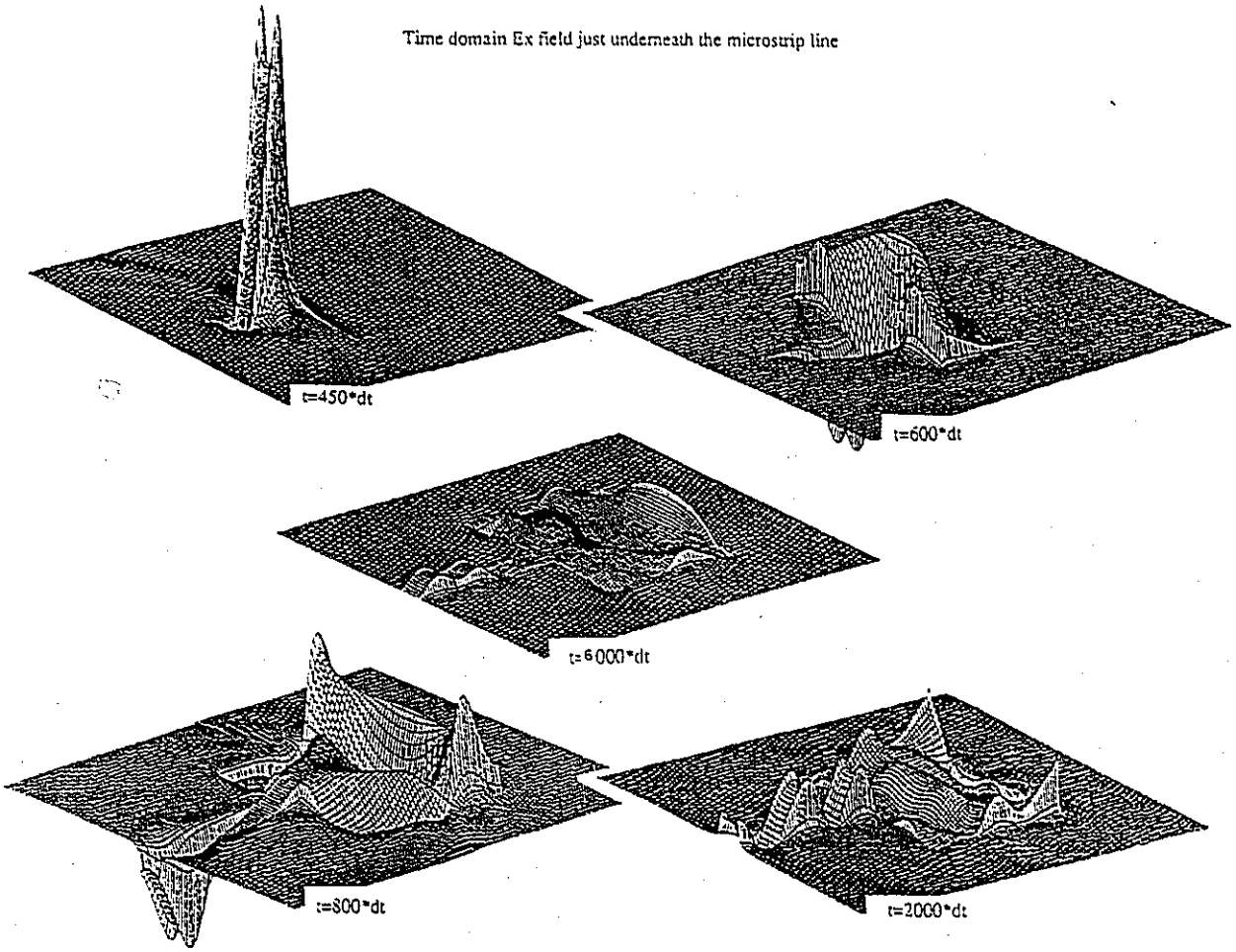

Figure 5.7: Time domain E_x-field just underneath the microstrip line.

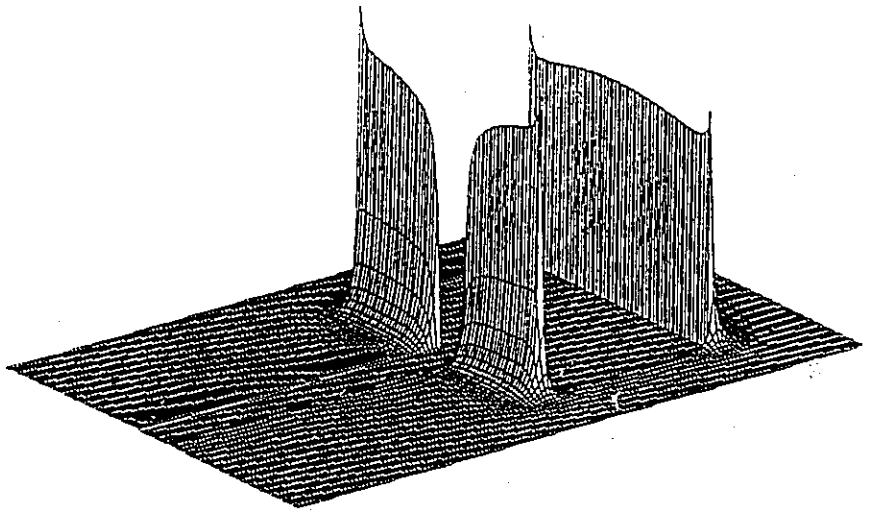

(a)

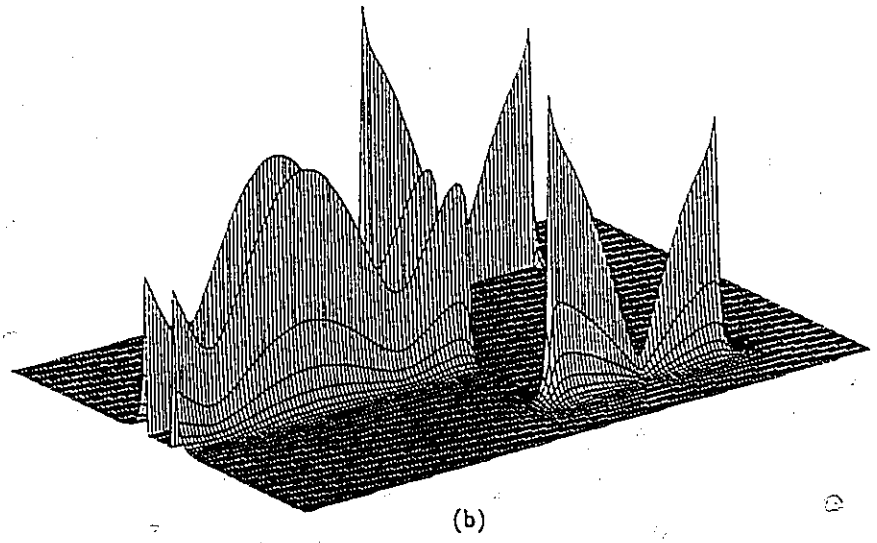

(b)

Figure 5.8: Equivalent magnetic current density distribution at f=3.0 GHz. (a) J_{mz}; (b) J_{my}.

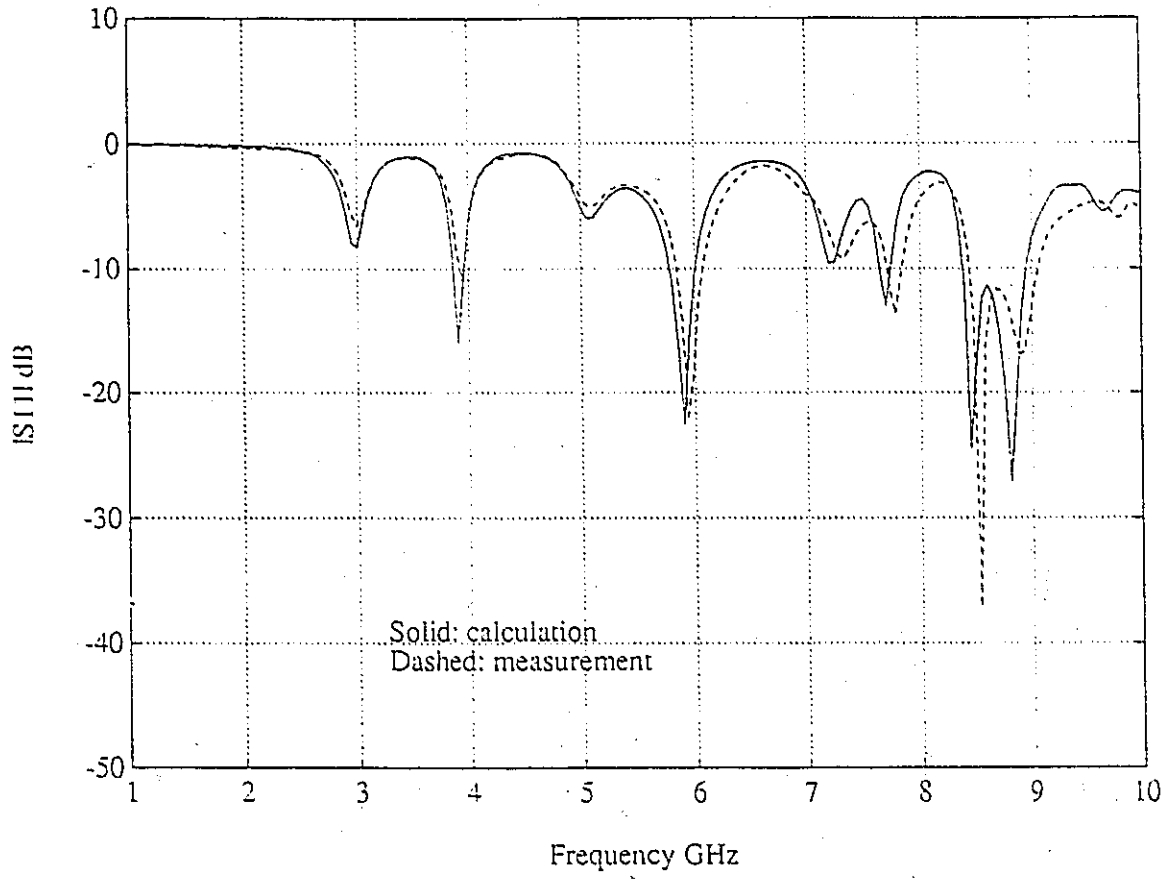

Figure 5.9: Reflection coefficient of line-fed patch antenna.

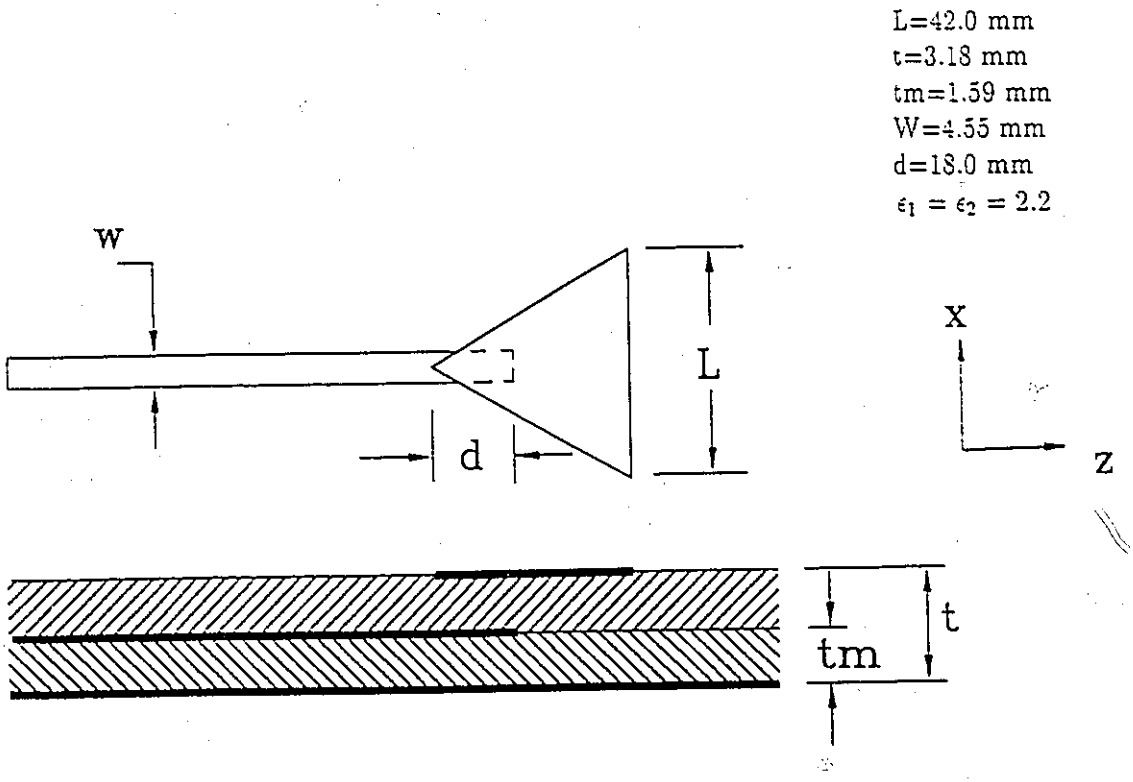

Figure 5.10: Proximity coupled microstrip antenna.

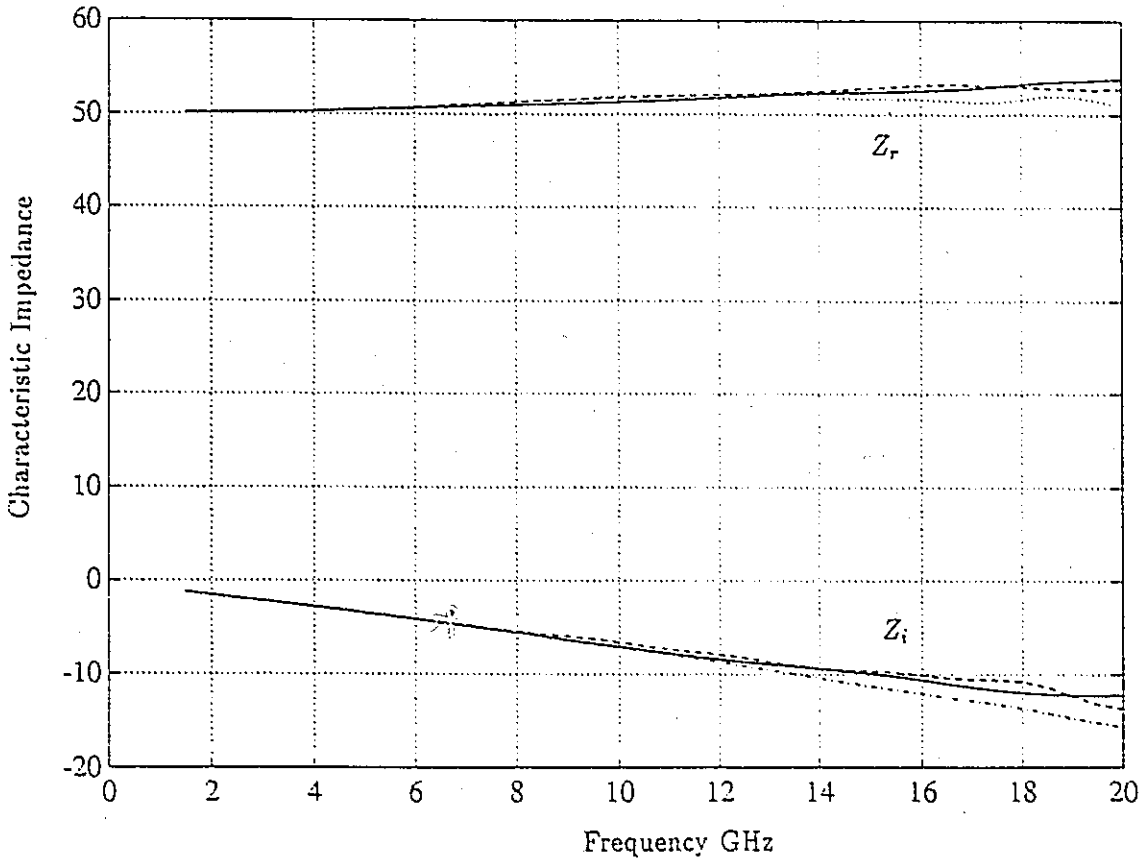

Figure 5.11: Characteristic impedance of the feed line for the proximity coupled microstrip antenna.

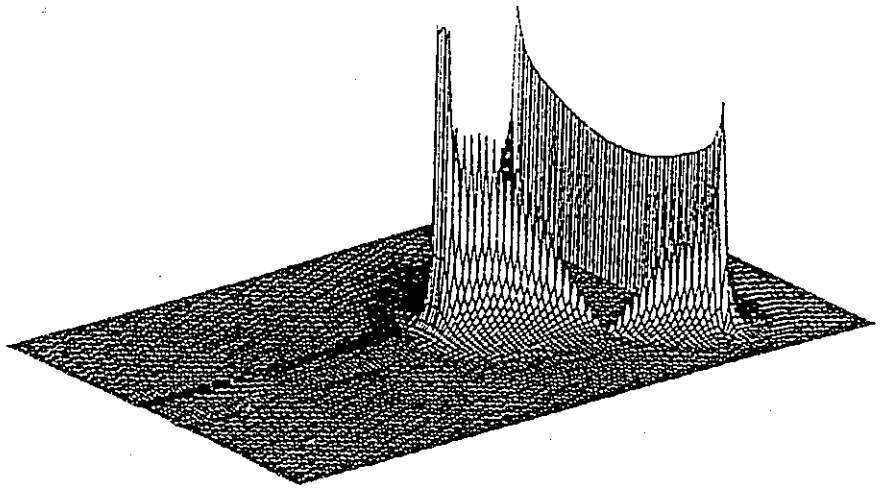

(a)

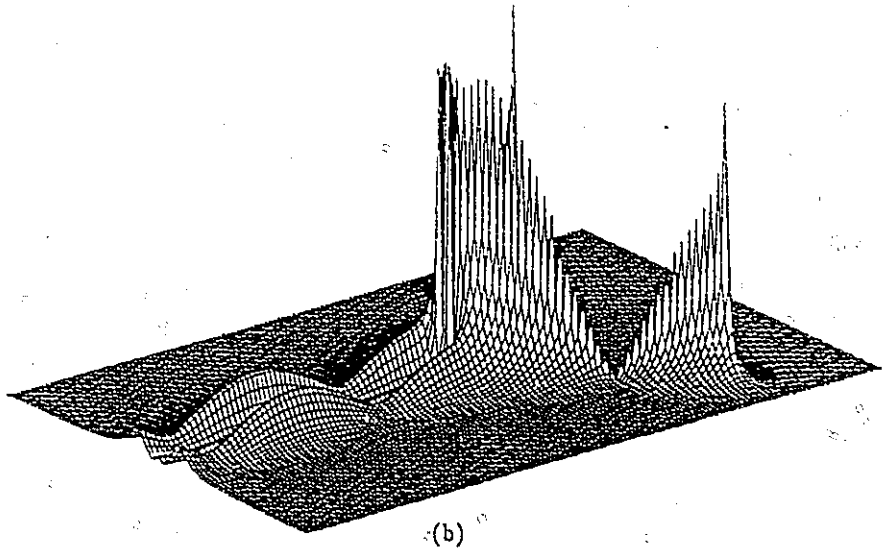

(b)

Figure 5.12: Equivalent magnetic current at f=3 GHz, (a) J_{mz}; (b) J_{my}.

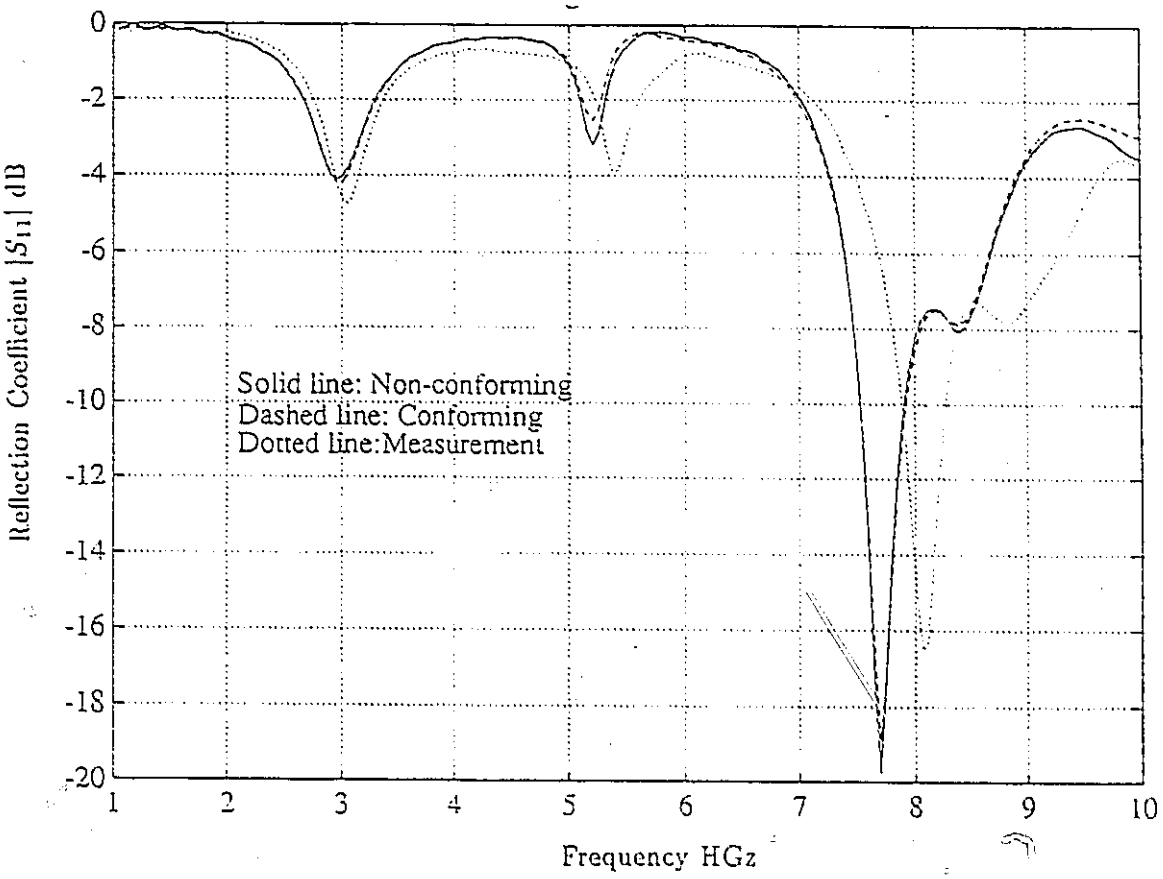

Figure 5.13: Reflection coefficient of proximity coupled microstrip antenna.

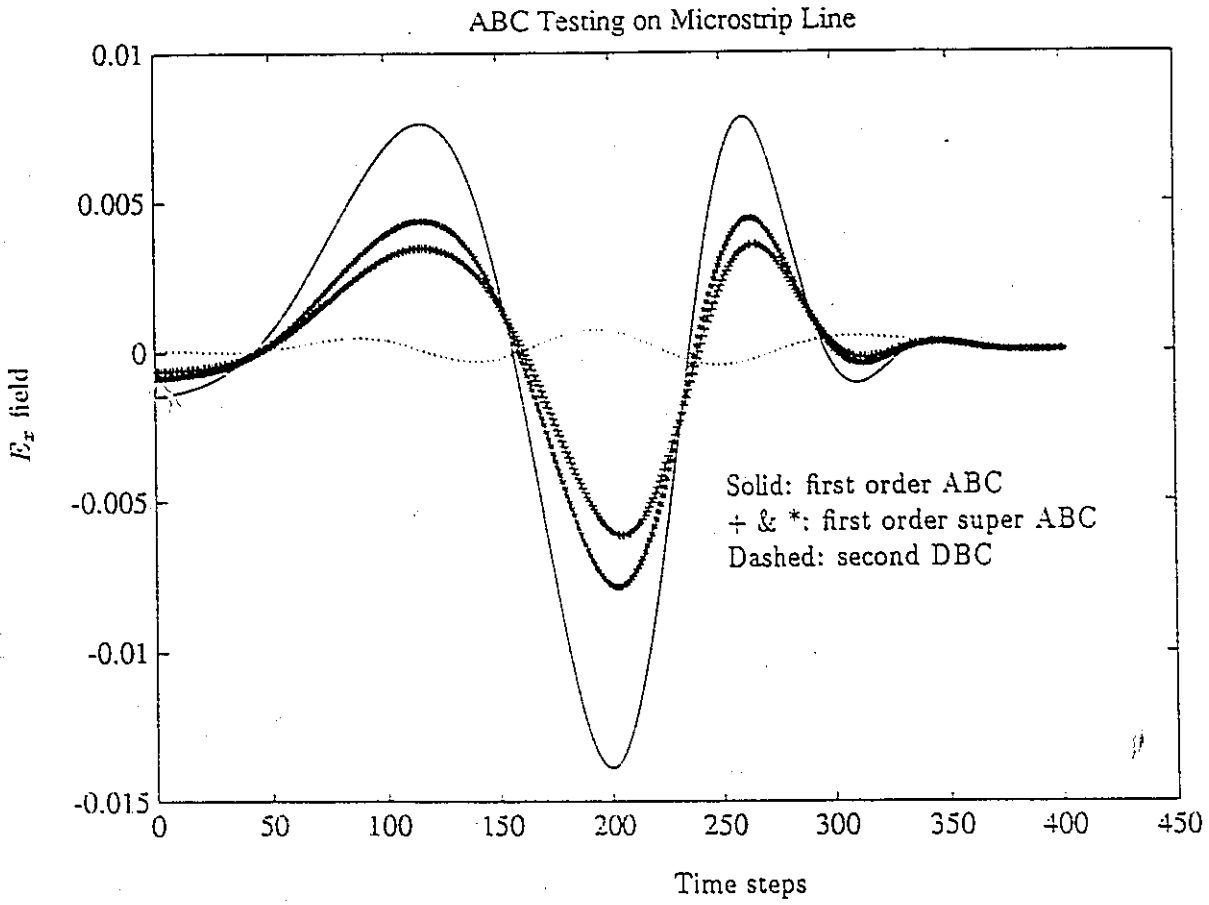

Figure 5.14: Reflected waves from different absorbing boundary conditions.

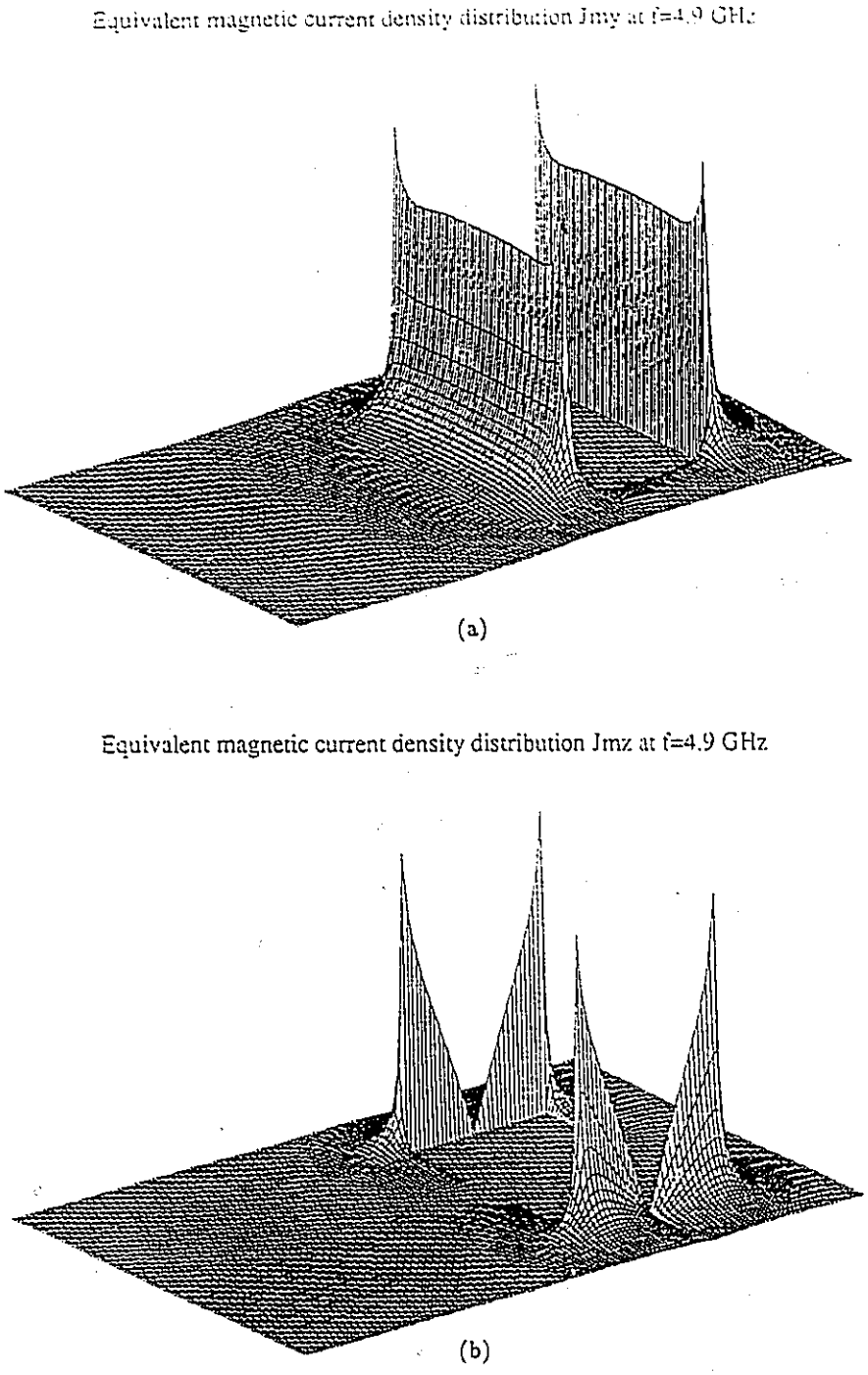

Figure 5.15: Equivalent magnetic current density distribution at f=4.9 GHz, on the upper patch plane, (a) J_{mz}; (b) J_{my}.

Jmy at f=4.9 GHz, on the lower patch plane

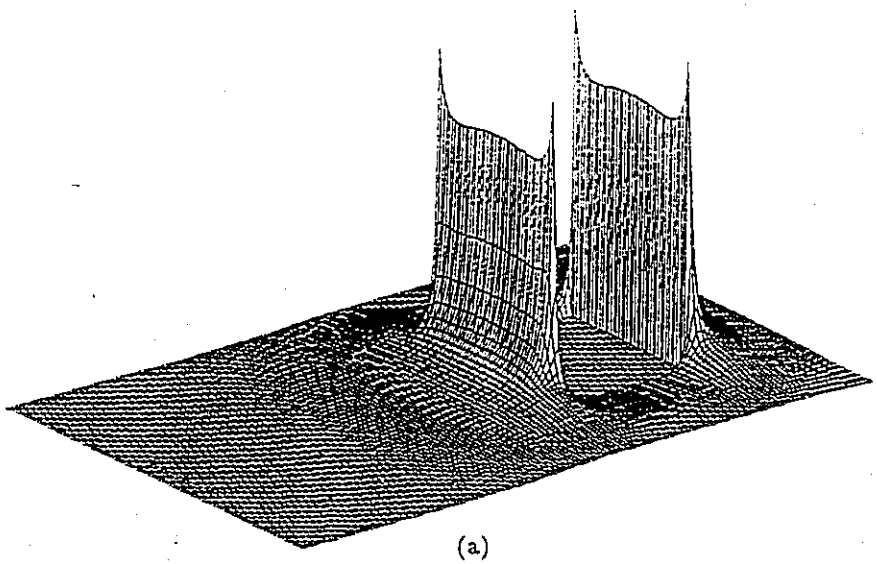

(a)

Jmz at f=4.9 GHz, on the lower patch plane

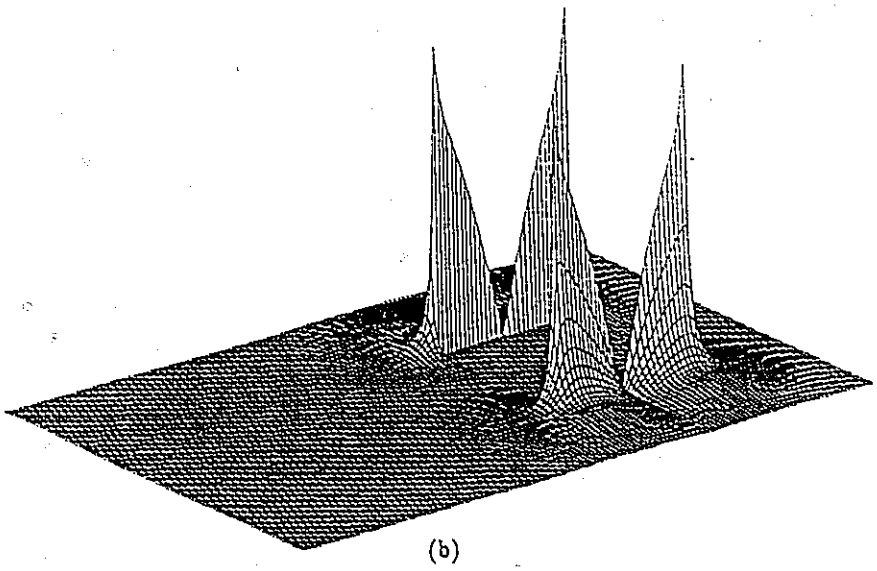

(b)

Figure 5.16: Equivalent magnetic current density distribution at f=4.9 GHz, on the lower patch plane, (a) J_{mz}; (b) J_{my}.

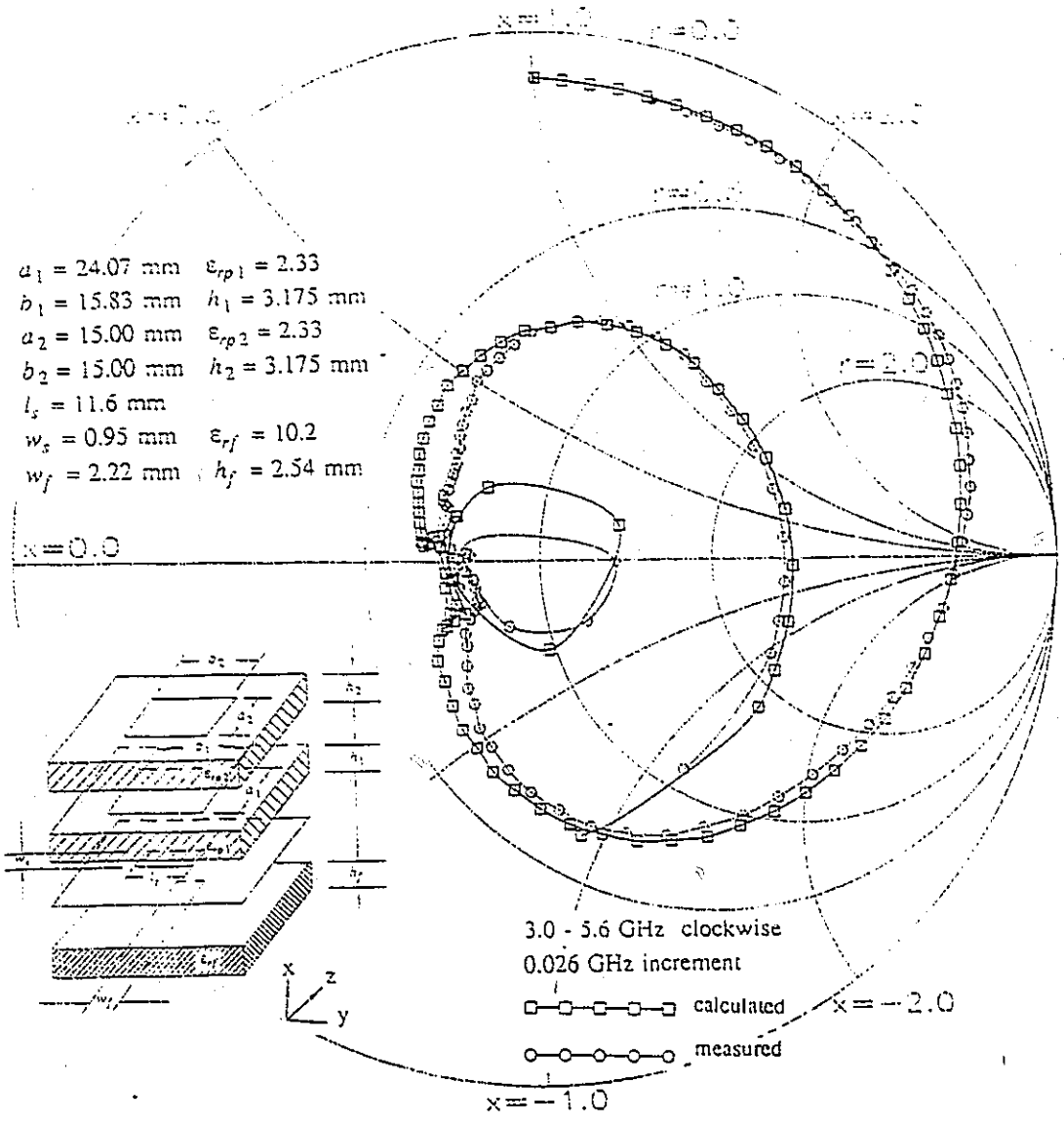

Figure 5.17: Input impedance of an aperture-coupled stacked microstrip antenna.

5.7 Summary

By carrying out a numerical analysis of a number of complex printed antennas, it has been shown that the finite-difference time-domain (FD-TD) method is a very powerful tool for analyzing planar printed antennas. The method can be used to accurately predict all of the antenna parameters of interest over a wide frequency range, based on one simulation in the time domain. It can provide not only input information for the antennas, but also very detailed field distributions, including the near and far fields. The three-dimensional FD-TD coaxial feed model provides a means to address more complicated, but practical printed antenna problems. The validity of the model is demonstrated by comparing the numerical and experimental results. The dispersive boundary condition was successfully used for analyzing components of printed antennas with large dielectric constant substrates. It has been demonstrated that the implementation of the DBC is much simpler than that for the super boundary condition, and that DBC's performance is better than both that of the first order ABC and super boundary condition.

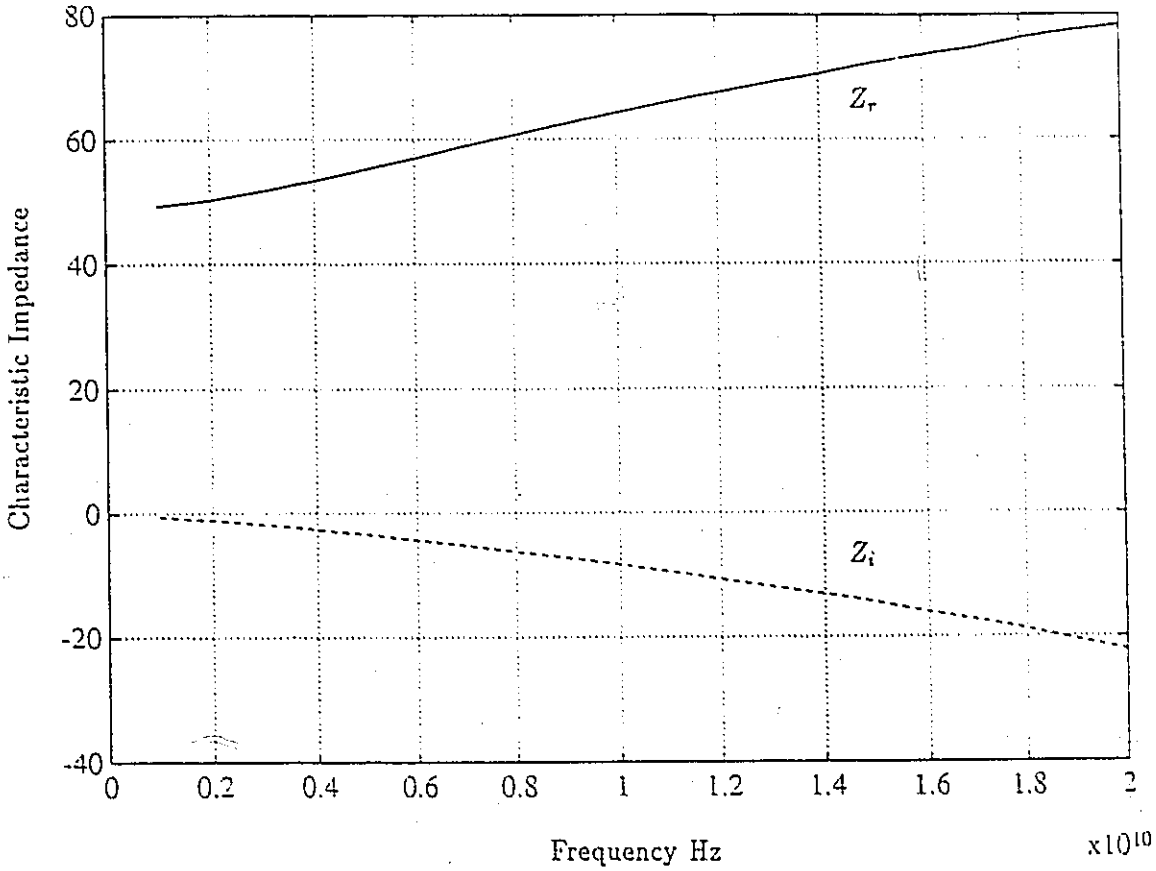

Figure 5.18: Characteristic impedance of the feed line for the aperture-coupled stacked antenna.

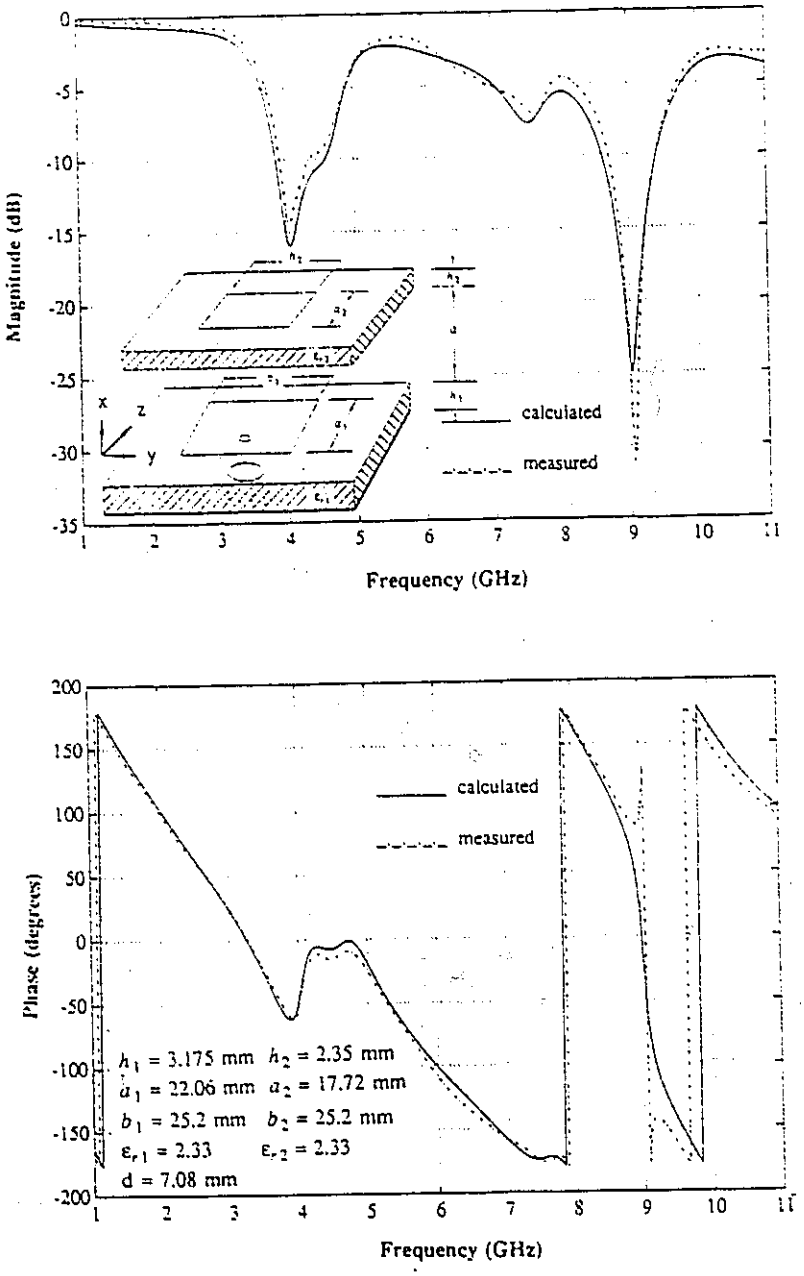

Figure 5.19: Reflection coefficient of a coaxial probe-fed stacked patch antenna.

Chapter 6

CONCLUSIONS

The main contribution of this dissertation is summarized below. In Chapter 2, a new scheme is presented for deriving finite-difference time-domain solutions of Maxwell's equations. In Chapter 3, a new theory of dispersive boundary condition (DBC) is systematically formulated and developed. By using these dispersive boundary conditions, one can analyze many dispersive structures with a much higher accuracy and a much smaller memory. In Chapter 4, modern spectrum estimation and digital filtering techniques are used with the FD-TD method to improve its efficiency for solving eigenvalue problems. The major improvements that can now be achieved in the efficiency of the FD-TD method are demonstrated by means of numerical and measurement results. In Chapter 5, the finite-difference time-domain technique is used to analyze complex planar printed antennas with various feed structures. In addition, the publications [71]-[89] are representative of the contributions this thesis has made to the FD-TD method and its applications.

We have adopted many concepts from digital filter and control theories and incorporated them into the FD-TD algorithm in Chapter 3. Actually, these concepts can be employed to help develop the FD-TD technique in at least other two aspects. One is dispersive material analysis by using the FD-TD. The other one is finite-difference time-domain

implementation of surface impedance boundary conditions [34, 35].

Only recently, the FD-TD method has been generalized to treat frequency dispersive materials. For general frequency dispersive materials, two approaches have been developed. In the first approach, convolution integrals are employed [36, 37]. Since these convolutions are applied to every discretization point, as well as for every time step, this approach is time consuming and requires a large memory. The second approach [2, 38] does not require time domain convolution. The time domain models of the dispersive materials are written in the form of ordinary time differential equations. The second algorithm is much more efficient than the first in terms of computational overhead and memory requirements. These two models can be unified by using a system concept.

The main issue that must be dealt with in order to generalize the FD-TD technique for analyzing dispersive materials is the development of an efficient time domain model. This model should describe the relationship between D and E or B and H in time domain, where D and E are the electric flux density and electric field intensity, respectively, and B and H are the magnetic flux density and magnetic intensity, respectively. In the case of electrical dispersion, let us consider the dispersive material as a linear system, or have E as the input of the system, and D as the output of the system. Then, the relation between D and E can be described by an ordinary time differential equation, by a time convolution integral, or by a frequency domain system function. The first two models are in the time domain and the third one is in the frequency domain. These three models can be derived from one another, i.e, they are just three different ways of describing the system. The use of the differential equation model produces the most efficient FD-TD algorithm for analyzing dispersive structures. In most practical problems, the dispersive characteristics of a material are described by a collection of discrete data points contained within some frequency band. Using these data as the frequency response of a system, the differential equation model of the dispersive structure can be obtained by designing an appropriate filter or system.

The above can also be applied to develop finite-difference time-domain implementation of surface impedance boundary conditions [34, 35].

In Chapter 3, it has been shown that several absorbing boundary conditions can be written into digital systems. It is expected that digital filter theory or system control theory, which are well developed, will be employed to develop a comprehensive absorbing boundary condition theory. Neural network theory might also be employed to further develop the theory developed in this chapter.

By carrying out analysis for a number of complex printed antennas in Chapter 5 and [79], it has been shown that the FD-TD method is a very powerful tool for analyzing planar printed antennas. However, it should be noted that there are two main drawbacks with regards to the use of the FD-TD method for microstrip component analysis. They are: the requirement for a large computer memory, as well as long computation run-times. The first problem is mainly due to the grid having to be very small in order to model the discontinuities on the substrate surface accurately. This can be overcome to some degree by using a variable mesh along the thickness direction of the substrate. The second problem can be overcome by using digital signal processing techniques. Several methods have been tried for reduing the computational time. They are the Prony [103], Modern Spectrum Estimation (MUSIC)[76], Multiple-Window-Method (MWM) [76], and System Identification [104] methods. From a spectrum estimation point of view, all these methods are to estimate the spectrum of FD-TD time domain data in a very short period of time, and all of them are spectrum estimation methods. It should be emphasized that for different structures, the signal models of the time domain data should be analyzed first, then according to the signal models, different methods are chosen. Otherwise the quality of results derived from the data will be less than optimal. For example, in the case of dielectric resonator analysis, the time domain sequence consists of very narrow band signals, which resemble sinusoidal signals. These kinds of signals can be analyzed best by using methods like MUSIC. They could not

be analyzed well by using System Identification method used in [104], which actually is the so-called ARMA spectrum estimation method in the signal processing techniques.

Bibliography

[1] K. S. Yee, "Numerical solution of initial boundary value problems involving Maxwell's equation in isotropic media," *IEEE Trans. Antenna Propagat.*, vol. AP-14, pp.302-307, May 1966.

[2] C. F. Lee, "Finite difference method for electromagnetic scattering problems," Ph.D. Dissertation, MIT, 1990.

[3] T. G. Jurgens, "Contour finite difference time domain modeling of electromagnetic wave scattering and interaction," Ph.D. Dissertation, Northwestern University, 1990.

[4] R. Holland, "Finite-Difference solution of Maxwell's equations in generalized nonorthogonal coordinates," *IEEE Trans. Nucl. Sci.*, vol. NS-30, No.6, pp.4589-4591, Dec. 1983.

[5] M. Fusco, "FDTD algorithm in curvilinear coordinates," *IEEE Trans. Antenna Propaga.*, vol. AP-38, pp.76-89, Jan. 1990.

[6] J. F. Lee, R. Palandech, and F. Mittra, "Modeling three-dimensional waveguide discontinuities using FDTD algorithm in curvilinear coordinate system," accepted for publication in *IEEE Trans. Antenna Propaga.*,.

[7] V. Shankar, W. F. Hall, and A. H. Mohammadian, "A time-domain differential solver for electromagnetic scattering problems," *Proceeding of the IEEE*, vol. 77, No.5, pp.709-721, May 1989.

[8] M. A. Morgan, *Finite Element and Finite Difference Methods in Electromagnetic Scattering*, edited, Elsevier, 1990.

[9] N. K. Madsen, and R. W. Ziolkowski, "Numerical solution of Maxwell's equations in the time domain using irregular nonorthogonal grids," *Wave Motion*, vol. 10, pp.583-596, 1988.

[10] A. C. Cangellaris, C. C. Lin, and K. K. Mei, "Point-matched time domain finite element methods for electromagnetic radiation and scattering," *IEEE Trans. Antenna Propaga.*, vol. AP-35, No.10, pp.1160-1173, Oct. 1987.

[11] A. C. Cangellaris, "Time-domain computation of electromagnetic wave scattering by the method of conforming boundary elements," Ph.D Dissertation, University of California, Berkeley, 1985.

[12] S. S. Zivanovic, K. S. Yee, and K. K. Mei, "A subgridding method for the time-domain finite-difference method to solve Maxwell's equation," *IEEE Trans. Microwave Theory Tech.* vol. MTT-39, No. 3, pp.471-479, March 1991.

[13] S. F. McCormick , *Multigrid Methods*, John Hopkins University Press, 1989.

[14] J. C. Wilson, "Stability of Richtmyer type difference schemes in any finite number of space variables and their comparison with multistep strang schemes," *J. Inst. Maths Applics.*, 10, pp.238-257, 1972.

[15] S. Abarbanel and D. Gottlieb, "A note on the leap-frog scheme in two and three dimensions," *Journal of Computational Physics*, 21, pp.351-355, 1976.

[16] L. Lapidus and G. F. Pinder, *Numerical solution of partial differential equations in science and engineering*, John Wiler & Sons. Inc., 1982.

[17] J. Fang, "Time domain finite difference computation for Maxwell's equations," Ph.D. Dissertation, University of California at Berkeley, 1989.

[18] J. Fang and K. K. Mei, "Super boundary condition treatment with the FD-TD method." *1988 IEEE AP-S Int. Symp. Dig.*, pp. 472-475, June 1989.

[19] R. Clayton and B. Engquist, "Absorbing boundary conditions for acoustic and elastic wave equations," *Bull. Seis. Soc. Am.*, vol. 67, pp. 1529-1540, 1977.

[20] B. Engquist and A. Majda, "Absorbing boundary conditions for numerical simulation of waves," *Math. Comp.*, vol. 31, pp.629-651, 1977.

[21] B. Engquist and A. Majda, "Radiation boundary conditions for acoustic and elastic wave calculations," *Comm. Pure Appl. Math.*, vol. 32, pp.314-357, 1979.

[22] G. Mur, "Absorbing boundary conditions for the finite difference approximatin of the time domain electromagnetic field equations," *IEEE Trans. Elec. Comp.*, vol. EMC-32, No. 4, pp.1073-1077, Oct. 1981.

[23] E. L. Lindman, "Free space boundary conditions for the time dependent wave equation," *J. Comp. Phys.*, vol. 18, pp.66-78, 1975.

[24] L. Halpern and L. N. Trefethen, "Wide-angle one-way wave equations," *J. Acoust. Soc. Am.*, vol.84, pp. 1397-1404, Oct. 1988.

[25] L. N. Trefethen and L. Halpern, "Well-posedness of one-way wave equations and absorbing boundary condition," *Math. Comput.*, vol. 47, pp. 421-435, Oct. 1986.

[26] J. G. Blaschak and G. A. Kriegsmann, "A Comparative Study of Absorbing Boundary Conditions," *Journal Of Computational Physics*, vol. 77, pp. 109-139, July 1988.

[27] T. G. Moore, J. G. Blaschak, A. Taflove and G. A. Kriegsmann, "Theory and application of radiation boundary operators," *IEEE Trans. Antenna Propagat.*, vol. 36, No. 12, pp. 1797-1812, Dec. 1988.

[28] A. Bayliss and E. Turkel, "Radiation boundary conditions for wave-like equations," *Commu. Pure Appl. Math.*, vol. 33, pp. 707-725, 1980.

[29] A. Bayliss, Goldstein, and E. Turkel, "On accuracy conditions for the numerical computation of waves," *J. Comp. Phys.*, vol. 59, pp. 396-404, 1985.

[30] R. G. Keys, "Absorbing boundary conditions for acoustic media," *Geogpysics*, vol. 50, No. 6, pp. 892-902, July 1985.

[31] R. L. Higdon, "Numerical absorbing boundary conditions for the wave equation," *Math. Comput.*, vol. 49, No. 179, pp. 65-91, July 1987.

[32] R. L. Higdon, "Absorbing boundary conditions for difference approximations to the multi-dimensional wave equation," *Math. Comput.*, vol. 47, No. 176, pp. 437-459, Oct. 1986.

[33] Z. Liao, H. L. Wong, B. Yang, and Y. Yuan, "A transmitting boundary for transient wave analyses," *Scientia Sinica, Series A*, vol. XXVII, No. 10, pp.1062-1076, Oct. 1984.

[34] J. G. Maloney and G. S. Smith, "The use of surface impedance concepts in the finite-difference time-domain method," *IEEE Trans. Antenna Propaga.*, vol. AP-40, pp. 38-48, Jan. 1992.

[35] , J. H. Beggs, R. J. Luebbers, K. S. Yee, and K. S. Kunz, "Finite-difference time-domain implementation of surface impedance boundary conditions," *IEEE Trans. Antenna Propaga.*, vol. AP-40, pp. 49-56, Jan. 1992.

[36] R. Luebbers, F. Hunsberger, K. Kunz, R. Standler, and M. Schneiderr, "A frequency-dependent finite difference time domain formulation for dispersive materials," *IEEE Trans. Electromagn. Compat.*, vol. EMC-32, pp. 222-227, Aug. 1990.

[37] R. J. Luebbers, F. Hunsberger, K. Kunz. "A frequency-dependent finite difference time domain formulation for transient propagation in plasma," *IEEE Trans. Antenna Propaga.*, vol. AP-39, pp. 29-34, Jan. 1991.

[38] T. Kashiwa and I. Fukai, "A treatment by the FD-TD method of the dispersive characteristics associated with electronic polarization," *Microwave Optical Technol. Lett.*, vol. 3, pp. 203-205, 1990.

[39] W. J. R. Hoefer, "Huygens and the computer–a powerful alliance in numerical electromagnetics," *Proceedings of The IEEE*, vol. 79, no. 11, pp. 1459-1471, Oct. 1989.

[40] Eswarappa, G. I. Costache and W. J. R. Hoefer, "TLM modelling of dispersive wideband absorbing boundaries with time domain diakoptics for S-parameters extraction," *IEEE Trans. Microwave Theory Tech.*, vol. 38, Apr. 1990.

[41] Z. Chen, W. J. R. Hoefer and M. M. Ney, "A new procedure for interfacing the transmission line matrix (TLM) method with frequency-domain solutions," *IEEE Trans. Microwave Theory Tech.*, vol. 39, no. 10, pp. 1788-1792, Dec. 1989.

[42] N. R. S. Simons, "Application of the transmission-line matrix method to open region field problems," Master Degree Thesis, Elec. Eng. Dept., University of Manitoba, Jan. 1990.

[43] C. Wilcox, "An expansion theorem for electromagnetic fields," *Comm. on Pure and Applied Math.*, vol. 9, pp. 115-134, 1956.

[44] D. S. Kâtz, A. Taflove, J. P. Brooks, and E. Harrigan, "Large-scale methods in computational electromagnetics," *Cray Channels.*, Spring 1991, pp. 16-19.

[45] A. Taflove, "The FD-TD method for numerical modeling of EM wave interactions with arbitrary structures," in *Electromagnetics Research, part 2: Progress in Electromagnetics Research*, J. A. Kong ED., Elsevier, New York, 1990, ch. 8.

[46] A. Taflove and M. Brodwin, "Numerical solution of steady-state electromagnetic scattering problems using the time dependent Maxwell's equations," *IEEE Trans. Microwave Theory Tech.*, vol. MTT-23, No. 8, pp. 623-630, Aug. 1975.

[47] R. Holland and L. Simpson, "Implementation and optimization of the thin structure formalism in THREDE," *IEEE Trans. Nuclear Sci.*, vol. NS-6, pp. 1625-1630, 1980.

[48] R. Holland, L. Simpson, and K. Kunz, "Finite difference analysis of EMP coupling ot lossy dielectric structures," *IEEE Trans. Electromagn. Compat.*, vol. EMC-22 pp. 203-209, 1980.

[49] D. M. Sheen, "Numerical modeling of microstrip circuits and antennas," Ph.D. Dissertation, MIT, 1991.

[50] D. M. Sheen, S. M. Ali, M. D. Abouzahra and J. A. Kong," Application of the three-dimensional finite-difference time-domain method to the analysis of planar microstrip circuits," *IEEE Trans. Microwave Theory Tech*,. vol. MTT-38, pp. 849-857, July 1990.

[51] X. Zhang, J. Fang, K. K. Mei and Y. Liu, "Calculations of the dispersive characteristics of microstrips by the time-domain finite- difference method," *IEEE Trans. Microwave Theory Tech.*, vol. MTT-36, pp. 263-267, Feb. 1988.

[52] X. Zhang and K. K. Mei, "Time domain finite difference approach to the calculation of the frequency dependent characteristics of microstrip discontinuities," *IEEE Trans. Microwave Theory Tech.*, vol. MTT-36, pp. 1775-1787, Dec. 1988.

[53] G. Liang, Y. Liu and K. K. Mei, "Full-wave analysis of coplanar waveguide and slotline using the time-domain finite-difference method," *IEEE Trans. Microwave Theory Tech.*, vol. MTT-37, pp. 1949-1957, Dec. 1989.

[54] A. Reineix and Bo. Jecko. "Analysis of microstrip patch antennas using finite difference time domain method," *IEEE Trans. Antenna Propaga.*, vol. AP-37, No.10, pp.1361-1368. 1989.

[55] E. Sano and T. Shibata, "Fullwave analysis of picosecond photoconductive swetches," *IEEE Journal of Quantum Electronics*, vol. 26, pp. 372-377, Feb. 1990.

[56] R. H. Voelker and R. J. Lomax, "A finite-difference transmission line matrix method incorporating a nonline device model," *IEEE Trans. Microwave Theory Tech.*, vol. MTT-38, pp. 302-312, March 1990.

[57] W. Sui, D. A. Christensen, and C. H. Durney, "Extending the two- dimensional FDTD method to hybrid electromagnetic systems with active and passive lumped elements," *IEEE Trans. Microwave Theory Tech.*, vol. MTT-40, pp. 724-730, April 1992.

[58] K. L. Wu, M. Spenuk, J. Litva and D. G. Fang, "Theoretical and experimental study of feed network effects on the radiation pattern of series-fed microstrip antenna arrays," *IEE Proceedings Pt. H*, vol. 138, pp. 238-242, 1991.

[59] D. Pozar, "Input impedance and mutual coupling of rectangular microstrip antennas," *IEEE Trans. Antenna and Propagation*, vol. AP-30, pp. 1191-1196, 1982.

[60] J. R. Mosig and F. E. Gardiol, "General integral equation formulation for microstrip antennas," *IEE Proceedings Pt. H*, vol. 132, pp. 424-432, 1985.

[61] W. C. Chew, Z. Nie, H. Liu and Y. T. Lo, "Analysis of a probe-fed microstrip disk antenna," *IEE Proceedings Pt. H*, vol. 138, pp. 185-191, 1991.

[62] D. Pozar and S. M. Voda, "A rigorous analysis of a microstrip line fed patch antenna," *IEEE Trans. Antenna and Propagation*, vol. AP-35, pp. 1343-1349, 1987.

[63] K. L. Wu, J. Litva, R. Fralich and C. Wu, "Full wave analysis of arbitrarily-shaped line-fed microstrip antennas using triangular finite element method." *IEE Proceedings Pt. H*, in press.

[64] C. Wu, J. Wang, R. Fralich and J. Litva, "A rigorous analysis of an aperture-coupled stacked microstrip antenna," *Microwave and Optical Technology Letters*, vol. 3, pp. 400-404, 1990.

[65] M. D. Pourcq, "Field and power-density calculations in closed microwave systems by three-dimensional finite differences," *IEE Proceedings*, vol. 132, Pt. H, no. 6, pp.360-368, Oct. 1985.

[66] J. C. Oliver and D. A. McNamara, "Finite-Difference Time-Domain (FD-TD) analysis of discontinuities in homogeneous, dispersive waveguides," *Electron. Lett.*, vol. 25, no. 15, pp. 1006-1007, 1989.

[67] J. C. Oliver and D. A. McNamara, "Analyzing edge slots in rectangular waveguides using finite-difference time-domain method," *Electron. Lett.*, vol. 26, no. 15, pp. 1135-1136, 1990.

[68] P. Alinikula and K. S. Kunz, "Analysis of waveguide aperture coupling using the finite-difference time-domain method," *IEEE Microwave and Guided Wave Letters*, vol. 1, no. 8, pp.189-191, August 1991.

[69] S. T. Chu, "Modeling of guided-wave optical structures by the finite-difference time-domain method," Ph.D. Dissertation, the University of Waterloo, 1990.

[70] S. T. Chu and S. K. Chaudhuri, "Combining modal analysis and the FD-TD method in the study of dielectric waveguide problems," *IEEE Trans. Microwave Theory Tech.*, vol. MTT-38, pp. 1755-1760, Nov. 1990.

[71] Z. Bi, K. Wu and J. Litva, "Application of the FD-TD method to the analysis of H-plane waveguide discontinuities," *Electron. Lett.*, vol. 26, no. 22, pp. 1897-1898, 1990.

[72] J. Litva, Z. Bi, K. Wu, R. Fralich and C. Wu, "Full-wave analysis of an assortment of printed antenna structures using the FD-TD method," *1991 IEEE AP-S Int. Symp. Dig.*, pp. 410-413, June 1991.

[73] J. Litva, K. Wu and Z. Bi, "Application of the FDTD technique to the analysis of printed antenna structures," presented at *Process in Electromagnetics Research Symposium*, Cambridge, Massachusetts, USA, July 1991.

[74] Z. Bi, K. Wu, C. Wu and J. Litva, "A new finite-difference time-domain algorithm for solving Maxwell's equations," *IEEE Microwave and Guided Wave Letters*, vol. 1, pp. 382-384, December 1991.

[75] Z. Bi, K. Wu, C. Wu and J. Litva, "A dispersive absorbing boundary condition for microstrip component analysis using the FD-TD method," *IEEE Trans. Microwave Theory Tech.*, vol. MTT-40, pp. 774-777, April 1992.

[76] Z. Bi, Y. Shen, K. Wu, and J. Litva, "Fast finite-difference time-domain analysis of dielectric resonators using digital filtering and spectrum estimation techniques," *IEEE Trans. Microwave Theory Tech.*, vol. MTT-40, August 1992.

[77] Y. Shen, Z. Bi, K. Wu, and J. Litva, "FD-TD analysis of open cylindrical dielectric resonators," *Microwave and Optical Technology Letter*, vol. 5, pp. 261-265, June 1992.

[78] C. Wu, K. Wu, Z. Bi and J. Litva, "Modelling of coaxial-fed microstrip patch antenna by finite difference time domain method," *Electron. Lett.*, vol. 27, no. 19, pp. 1691-1692, September 1991.

[79] C. Wu, K. Wu, Z. Bi and J. Litva, "Accurate characterization of planar printed antennas using finite difference time domain method," *IEEE Trans. Antenna Propaga.*, vol. 40, no. 5, pp. 526-534, May 1992.

[80] Z. Bi, J. Litva, K. Wu and C. Wu, "Dispersive absorbing boundary Conditions (DBC) for waveguide component analysis using the FD-TD method," submitted to *IEEE Trans. Microwave Theory Tech.*.

[81] Z. Bi, Y. Shen, K. Wu and J. Litva, "Enhancing finite-difference time-domain analysis of resonators using digital filtering and spectrum estimation techniques," *1992 IEEE MTT-S Int. Symp. Dig.*, pp. 869-872, June 1992.

[82] Y. Shen, Z. Bi, K. Wu and J. Litva, "Efficient FD-TD analysis of dielectric resonators with tuning screw and multilayer structures," *1992 IEEE MTT-S Int. Symp. Dig.*, pp. 967-970, June 1992.

[83] Z. Bi, K. Wu, and J. Litva, "Designing dispersive boundary condition (DBC) for the FD-TD method using digital filtering theory," *1992 IEEE AP-S Int. Symp. Dig.*, July 1992.

[84] Z. Bi and J. Litva, "Consideration of a one-way dispersive boundary condition (DBC) for the FD-TD method," *1992 IEEE AP-S Int. Symp. Dig.*, July 1992.

[85] J. Litva, K. Wu, Z. Bi and C. Wu, "Some considerations for microstrip coplanar-waveguide antennas," *1992 IEEE AP-S Int. Symp. Dig.*, July 1992.

[86] Z. Bi, J. Litva, K. Wu and C. Wu, "Using digital signal processing techniques with the FD-TD method," presented at *1992 IEEE-APS/URSI/NEM Joint Symposia*, Chicago, USA, July 1992.

[97] P. Stoica and T. Söderström. " Statistical analysis of MUSIC and subspace rotation estimates of sinusoidal frequencies," *IEEE Trans. Acoust., Speech, Signal Processing*, vol. ASSP-39, pp.1836-1847, August 1991.

[98] S. Haykin, *Adaptive filter theory*, 2nd ed., Prentice-Hall, Inc., 1991.

[99] S. L. Marple Jr., *Digital spectrum analysis with applications*, Prentice-Hall, Inc., 1987.

[100] P. Stoica and T. Söderström, "On spectral and root forms of sinusoidal frequency estimators," *Proc. IEEE Int. Conf. Acoust., Speech, Signal Processing, ICASSP'91*, Toronto, Canada, pp. 3257-3260.

[101] A. Drosopoulos and S. Haykin, "Adaptive radar parameter estimation with Thomson's Multiple-Window method," chapter 7, In S. Haykin and A. Steinhardt eds., Adaptive Radar Detection and Estimation, Wiley, 1991.

[102] J. G. Blaschak and T. G. Moore, "Adaptive absorbing boundary condition," presented at *Process in Electromagnetics Research Symposium*, Cambridge, Massachusetts, USA, July 1991.

[103] W. L. Ko and R. Mittra, "A combination of FD-TD and prony's method for analyzing microwave integrated circuits," *1991 IEEE AP-S Int. Symp. Dig.*, pp. 1742-1745, June 1991.

[104] W. Kuempel and I. Wolff, "Digital signal processing of time domain field simulation result using the system identification method," *1992 IEEE MTT-S Int. Symp. Dig.*, June 1992.

[87] K. Wu, C. Wu, Z. Bi and J. Litva,"Modelling of electromagnetic packaging and coax-to-microstrip transition effects by FD-TD method," presented at *1992 IEEE-APS/URSI/NEM Joint Symposia*, Chicago, USA, July 1992.

[88] C. Wu, K. Wu, Z. Bi and J. Litva,"Coaxial-fed model for microstrip patch antenna using the finite-difference time-domain method," presented at *1992 IEEE-APS/URSI/NEM Joint Symposia*, Chicago, USA, July 1992.

[89] Z. Bi, J. Litva, K. Wu and C. Wu,"FD-TD analysis of waveguide component using dispersive boundary condition (DBC)," *Symposium on Antenna Technology and Applied Electromagnetics*, Canada, August 1992.

[90] D. Kajfez and P. Guillon, "Dielectric Resonators", Artech House, 1986.

[91] A. Navarro, M. J. Nuñez and E. Martin, "Study of TE_0 and TM_0 modes in dielectric resonators by a finite difference time-domain method coupled with the Discrete Fourier transform," *IEEE Trans. Microwave Theory Tech.*, vol. MTT-39, pp. 14-17, Jan. 1991.

[92] D. H. Choi and W. J. R. Hoefer, "The finite difference-time domain method and its application to eigenvalue problems," *IEEE Trans. Microwave Theory Tech.*, vol. MTT-34, pp. 1464-1470, Dec. 1986.

[93] S. Haykin, *Communication systems*, 2nd ed., John Wiley & Sons Inc., 1983.

[94] J. O. Smith, "Techniques for digital filter design and system identification with application to the violin," Ph.D. Dissertation, Elec. Eng. Dept., Stanford University.

[95] D. F. Elliott, *Handbook of digital signal processing, engineering applications*, Ed., Academic Press, Inc., 1987.

[96] J. N. Little, *Signal processing toolbox for use with Matlab*, The Math Works, Inc., 1988.